Non-equilibrium dynamics of chiral liquid crystal

Abstract

In this dissertation, we experimentally studied non-equilibrium dynamics of cholesteric liquid crystal (CLC), which is a chiral phase of liquid crystal (LC) exhibiting helical director field. In spite of increasing understanding on the structure and equilibrium properties of CLC owing to development of microscopy and numerical calculations, the non-equilibrium behaviors have been far from understood due to the complex coupling between the chiral structure and dynamics.

First, we investigated the rotational motion of CLC droplets under a temperature gradient, which is called the Lehmann effect, a long-standing unsolved problem in CLC physics. We controlled the angle between the helical axis of CLC droplets and the direction of the temperature gradient by changing anchoring conditions of LC cells. As a result, we observed that the three types of CLC droplets, one of which we observed for the first time, rotate under a temperature gradient. We found that the rotational velocity of these droplets depends differently on their size. By determining the 3D structures of the droplets using the fluorescence confocal polarizing microscopy (FCPM), we constructed a phenomenological model to describe these rotational behaviors following the basic ideas in a hydrodynamic theory of LC (the Ericksen-Leslie theory). Our phenomenological model showed that a surface torque induced by a temperature gradient is required to explain the rotational velocity of the three types of CLC droplets.

Secondly, we studied the Marangoni-effect-driven spontaneous swimming motion of CLC droplets dispersed in surfactant solutions. We discovered that a CLC droplet with a helical director field swims in a helical path driven by the Marangoni flow. We also found that the handedness of the helical path is reversed when that of the droplet is reversed by replacing the chiral dopant with the enantiomer. In contrast, we observed that nematic liquid crystal droplets swim in straight paths. Consequently, we concluded that the helical motion of the CLC droplets is induced by chirality of CLC.

Finally, we proposed a phenomenological model of the self-propelled helical motion of the CLC droplets. Our model was constructed by symmetry argument in chiral systems, and it describes the dynamics of CLC droplets with a coupled time-evolution equations in terms of a velocity, an angular velocity and a tensor variable representing the symmetry of the helical director field of the droplet. We found that helical motions appear in our model in addition to other chiral motions. By investigating bifurcation behaviors between each chiral motion, we found that the chiral coupling terms between the velocity and the angular velocity, and the nonlinearity of model equations play a crucial role in the emergence of the helical motion of the CLC droplet.

Acknowledgement

I would like to show my greatest appreciation to Prof. Masaki Sano, who has been my supervisor for 5 years in graduate school. I have been always stimulated by his great insights and constructive criticisms on my works. Without his guidance and persistent helps, this dissertation would not have been possible. The time I has been working with him will be my valued treasure.

I would like to offer my special thanks to Prof. Takao Ohta, who helped me constructing our theoretical model of spontaneous helical motion. He always encouraged and guided me by raising crucial questions I have to solve. I also appreciate Dr. Tetsuya Hiraiwa discussing patiently with me on the theoretical model. Especially, he taught me how to think logically and raise appropriate questions. Also, my skills on theoretical analysis are enhanced by his advice and suggestions. I would also thank Dr. Mitsusuke Tarama for giving me essential theoretical advice.

Furthermore, I appreciate Dr. Masafumi Kuroda, who taught me fundamental physics and experimental techniques on liquid crystals from the beginning of my graduate school. I could not have even started my works on the Lehmann effect without his kind helps.

I am deeply grateful to Dr. Ken H. Nagai, who gave us essential comments on our works and provided me opportunities to discuss with many researchers. I am strongly affected by his research attitude and insight into physics.

I would like to express my gratitude to Prof. Helmut R. Brand, who has been encouraging me to work on non-equilibrium dynamics in chiral systems.

I thank all the present and former lab members for their advices and helps on our works. I have enjoyed life in laboratory thanks to their friendliness and generosity. I was strikingly stimulated by their attitude on their research. In special, I would appreciate Prof. Kazumasa A. Takeuchi, Dr. Kyogo Kawaguchi, Dr. Yohei Nakayama and Dr. Sosuke Ito, who show me how interesting non-equilibrium physics is. The time I had spent with them in the same lab has great influence on my research. Also, I would like to offer my special thanks to Mr. Daiki Nishiguchi for his inspiring me by his broad knowledge on physics and insights into experimental data.

I would like to thank Prof. Masahiro Takinoue and Dr. Masamune Morita for their kind supports on microfluidic experiments. Also, I would appreciate Prof. Mitsuhiro Shibayama and Mr. Kazu Hirosawa for their kind helps on the density measurement, which was essential in our experiments on the helical motion of CLC droplets.

Finally, I am sincerely appreciate my family and all they have done for me.

List of publication

1. T. Yamamoto, M. Kuroda and M. Sano.
   "Three-dimensional analysis of thermo-mechanically rotating cholesteric liquid crystal droplets under a temperature gradient"
   EPL (Europhysics Letters), **109**, 46001 (2015).

2. T. Yamamoto and M. Sano.
   "Chirality-induced helical self-propulsion of cholesteric liquid crystal droplets"
   arXiv: 1604.00298 (2016).

3. T. Yamamoto and M. Sano.
   "Chirality-induced helical self-propulsion of cholesteric liquid crystal droplets"
   Manuscript in preparation (2017).

4. T. Yamamoto and M. Sano.
   "Theoretical model of chirality-induced helical self-propulsion of cholesteric liquid crystal droplets"
   Manuscript in preparation (2017).

This dissertation includes the main results in these papers.

- Chapter 3 includes the main results in paper 1.

- Chapter 4 includes the main results in paper 2 and 3.

- Chapter 5 includes the main results in paper 2 and 4.

Contents

Chapter 1

Introduction

"Chirality" is a term describing the reflection symmetry breaking. In other words, an object is "chiral", if it is not identical with the mirror-image (Fig. 1.1). We are surrounded by various chiral-shaped objects and have been also more or less attracted aesthetically by their sophisticated shapes such as a helix. In addition to many artificial chiral objects such as spiral staircases, nails and propellers, chiral shapes are often seen in living things, such as snails, vines and flagella because biomolecules such as amino acids, proteins and DNA have chirality. Chiral structures are ubiquitous in our world.

From the scientific point of view, it is quite natural to study the non-equilibrium dynamics of these chiral objects as well as the sophisticated static structures. Actually, the dynamics of chiral objects and systems have been rigorously investigated in a wide range of scientific fields: for instance, reaction dynamics of asymmetric reactions in chemistry [1, 2, 3], thermally-driven rotation of skyrmion phase (chiral spin phase) in physics [4, 5], unidirectional rotation of molecular motors in biology [6], etc. Among these intensive studies on non-equilibrium dynamics in chiral systems, "hydrodynamics in chiral systems" is a fascinating topic in fundamental physics [7, 8, 9]. Since fluids composed of chiral molecules are ubiquitous, especially in biological cells and tissues filled with water and chiral molecules, it is essential to elucidate the role of chirality in hydrodynamics not only from the view point of fundamental physics but also interdisciplinary science.

Cholesteric liquid crystals (CLC), which is a chiral phase of liquid crystal, have been studied as a model system of chiral fluids [10, 11]. However, the higher nonlinearity of the system compared to the Newtonian fluid has been an obstacle for analytical and also numerical approach from the view point of theoretical physics. Also, since the CLC exhibits three dimensional (3D) chiral structure, that is 3D helical director field, 3D observation of the structure has challenged the experimentalists. We know even hydrodynamics in the simplest achiral system, that is the Newtonian fluid whose dynamics is described by the Navier-Stokes equation, exhibits complicated phenomena, a representative of which is turbulence. However, we have been amazingly elucidating beautiful laws, such as Kolmogorov's 5/3 law [12], even from turbulence in the Newtonian fluid.

1

Here, *the aim of the dissertation is to experimentally extract simple laws governing the dynamics of the CLC, which is apparently too complicated, and gain a further understanding of roles of chirality in hydrodynamics.*

In this chapter, we overview the background and motivations of the topics we study in the dissertation.   We would like to start from introducing "non-equilibrium thermodynamics [11]", an established theoretical framework describing hydrodynamics. Since "non-equilibrium thermodynamics" is constructed by considering how spatial symmetries of systems play roles in hydrodynamics, we consider that it is a good start point to study the hydrodynamics in chiral systems.

Mirror

COOH   COOH

H_3C C ''''H   H''' C CH_3

NH$_2$ H_2N
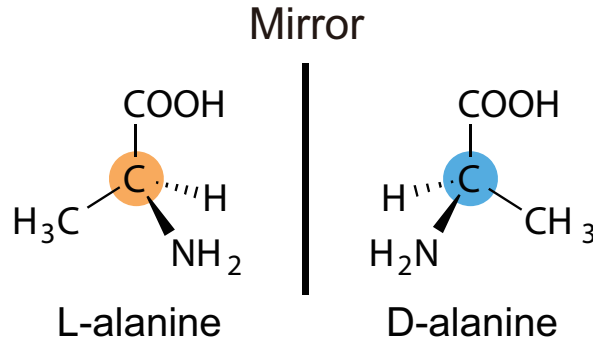
L-alanine   D-alanine

Figure 1.1: The concept of chirality. L- and D-alanine which are enantiomers are depicted as an example of chiral objects.

1.1   Non-equilibrium thermodynamics

1.1.1   Framework of non-equilibrium thermodynamics

In non-equilbrium thermodynamics, the concept of entropy, which is defined as a quantity indicating the irreversibility of the system in equilibrium is extended to non-equilibrium system assuming the local equilibrium.

We consider an adiabatically isolated system composed of a system and its surrounding. The variation of the entropy dS of the system is written as the sum of the entropy production dS_i of the system and the entropy dS_e supplied from its surrounding as follows,

$$dS = dS_e + dS_i. \tag{1.1}$$

According to the second law of thermodynamics, entropy production dS_i of the system is non-negative,

$$dS_i \geq 0. \tag{1.2}$$
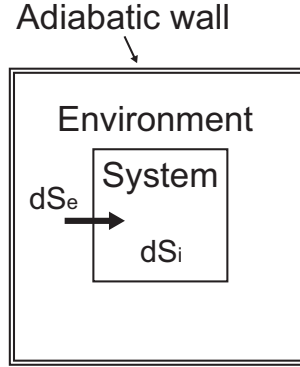
Figure 1.2: An adiabatically isolated system composed of a system and its surrounding environment.

Furthermore, considering a situation where the entropy density is written as a continuous function of space coordinates, we obtain,

$$\frac{\partial \rho s}{\partial t} = -\mathrm{div} \boldsymbol{J}_s + \sigma. \tag{1.3}$$

Here, ρ, s, $\boldsymbol{J}_s$ and σ are the density, entropy per unit mass, entropy flux per unit area and entropy production per unit volume and unit time. Also in the continuum description, we have the following non-negativity of entropy production σ according to the second law of thermodynamics,

$$\sigma \geq 0. \tag{1.4}$$

In the framework of the non-equilibrium thermodynamics, we describe the time evolution of the system by relating the entropy production σ and the irreversible processes in the system.

In equilibrium, entropy is written as a function of macroscopic physical quantities such as temperature, energy and pressure, etc. Assuming local equilibrium, in which the functional form of entropy in non-equilibrium states is identical with that in equilibrium, we can write σ as the product of flux $\boldsymbol{J}$ and thermodynamic force $\boldsymbol{X}$ in the system as follows,

$$\sigma = J_i X_i. \tag{1.5}$$

Here, we follow the Einstein summation convention, and J_i and X_i are cartesian components of $\boldsymbol{J}$ and $\boldsymbol{X}$, respectively. The thermodynamic force $\boldsymbol{X}$ represents the inhomogeneity of the system; for instance, temperature gradient, concentration gradient and density gradient. For instance, in a 1-component isotropic fluid, we may write,

$$\sigma = -\frac{1}{T} \boldsymbol{J}_q \cdot \frac{\nabla T}{T} - \frac{1}{T} \boldsymbol{\Pi} : \nabla \boldsymbol{v}, \tag{1.6}$$

where $\boldsymbol{J_q}, \Pi, \nabla T$ and $\nabla \boldsymbol{v}$ are the thermal flux, a flux which is the total stress subtracted by hydrostatic pressure, temperature gradient and velocity gradient tensor.[1] Here, since the flux $\boldsymbol{J}$ is not determined *a priori*, we need to phenomenologically represent the flux $\boldsymbol{J}$ as functions of thermodynamic force $\boldsymbol{X}$. Assuming the linear response, which actually holds in a wide range of experiments, we may write $\boldsymbol{J}$ defining the transport coefficient L_{ij},

$$J_i = L_{ij}X_j. \tag{1.7}$$

In the 1-component isotropic fluid, we obtain the Fourier's law $\boldsymbol{J_q} = -\lambda \nabla T$, where λ is the thermal conductivity. With the help of this phenomenological linear relation, we can describe the time evolution of the system using the conservation laws such as momentum conservation, energy conservation and angular momentum conservation.

In the 1-component isotropic fluid, we have only couplings between the conjugated fluxes and thermodynamic forces. However, couplings between fluxes and thermodynamic forces which are not conjugated are generally possible. Phenomena due to such couplings are called "cross effects". In such cases, we have non-zero value in off-diagonal elements of the transport coefficient matrix L. We will show the cross effects in detail below.

1.1.2   Cross effects

For instance, the Ludwig-Soret effect [13], in which particles in a solution are transported by temperature gradient, and the Peltier effect [11], where heat is transported by electric voltage are known as examples of cross effects. In the Ludwig-Soret effect, particles are transported not only by diffusion due to the brownian motion of particles but also by a temperature gradient. Hence, we can write the flux of particles J_{particle} as follows,

$$J_{\text{particle}} = -D\nabla c - cD_T\nabla T, \tag{1.8}$$

where the concentration, diffusion constant and thermal diffusion constant are denoted as c, D and D_T, respectively. Importantly, the flux J_{particle} of particles is coupled not only with the concentration gradient ∇c but also with the temperature gradient ∇T.

1.1.3   Curie principle

However, all fluxes and thermodynamic forces cannot necessarily couple. The spatial symmetry of the system provides restrictions on the couplings. The "Curie principle [11]" states the restriction as follows.

---

[1]The scalar product of two tensors is indicated by inserting the symbol ":" between the two tensors; for instance, $\boldsymbol{S} : \boldsymbol{T} = \sum_{i,k} S_{ik}T_{ki}$ for the second rank tensors $\boldsymbol{S}$ and $\boldsymbol{T}$. In contrast, we define exterior products of two vectors as $(\boldsymbol{ab})_{ij} = a_i b_j$.
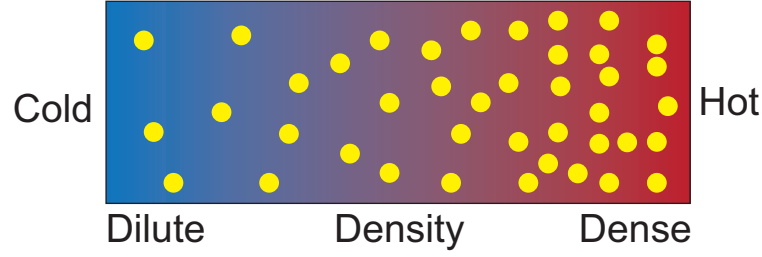
Figure 1.3: Schematic of Ludwig-Soret effect. Particles in a solution are transported not only by thermal diffusion but also by a cross effect between the particle flux and the temperature gradient.

Generally, fluxes and thermodynamic forces are represented as tensors. Tensors with different characters such as scalars, vectors, second-rank tensors and so on, are transformed in different ways by spatial symmetry operations. On the other hand, when the system has some spatial symmetries, fluxes should be invariant under the corresponding symmetry operations. Hence, tensors with different characters cannot always couple. Especially in an isotropic system, which has the highest spatial symmetry, only tensors with the same tensorial characters can couple. For instance, in the 1-component isotropic fluid we saw above, the heat flux represented as vector and the velocity gradient represented as second-rank tensor cannot couple according to the isotropy of the system. In this way, transport coefficient matrices are restricted by the spatial symmetry of systems. This statement is called the "Curie principle". To put it the other way around, *the Curie principle states that cross effects forbidden by spatial symmetries of systems can occur when the spatial symmetries are broken.*

1.2 Cross effects in chiral fluids

What can we claim on the hydrodynamics of a chiral fluid, the cholesteric liquid crystal (CLC)? In achiral fluids such as the Newtonian fluid, we can introduce only "scalars" as transport coefficients due to the space-reflection symmetry.

In contrast, since the CLC breaks the space-reflection symmetry, "pseudo scalars" can be introduced as transport coefficients in addition to scalars according to the Curie principle.

Here, we can classify scalars and pseudo scalars by inversing the cartesian coordinates $x \to -x, y \to -y, z \to -z$. Under such coordinate inversion,

$$\text{if } \phi \text{ is a scalar,} \quad \phi \to \phi, \tag{1.9}$$

$$\text{if } \phi \text{ is a pseudo scalar,} \quad \phi \to -\phi. \tag{1.10}$$

Consequently, "polar" vectorial external fields such as temperature gradient and concentration gradient can couple with rotational motion, which is an "axial" vectorial

quantity, via pseudo scalar transport coefficients. For instance, if we have a chiral object under a external field $\boldsymbol{E}$, the angular velocity $\boldsymbol{\omega}$ of the object can couple with the external field $\boldsymbol{E}$ by symmetry argument as,

$$\boldsymbol{\omega} = \phi\boldsymbol{E}, \tag{1.11}$$

where ϕ is a pseudo scalar coefficient. The relation (1.11) satisfies parity, since both $\boldsymbol{\omega}$ and $\phi\boldsymbol{E}$ are axial vectors. Actually, such cross effects emerge in the dynamics of the CLC due to the space-reflection symmetry breaking as we will see in the dissertation.

1.3   Overview of the dissertation

In this section, we overview the contents of the dissertation.

1.3.1   Lehmann effect: Rotation of cholesteric liquid crystal droplets under a temperature gradient (Chapter 3)

The liquid crystal (LC) exhibits exotic hydrodynamic properties which do not emerge in the Newtonian fluid [10, 14]. Since LC is composed of rod-like molecules, LC has local orientational order as shown in Fig. 1.4, called director field denoted as $\boldsymbol{n}$, in addition to the fluidity as the Newtonian fluid has. For instance, due to the anisotropy of LC, viscous torque is exerted on LC molecules, even under irrotational flow. Not only to the hydrodynamic flow, LC exhibits anisotropic responses under various non-equilibrium external fields such as electric field, magnetic field and temperature gradient, etc.

Nematic Liquid Crystal
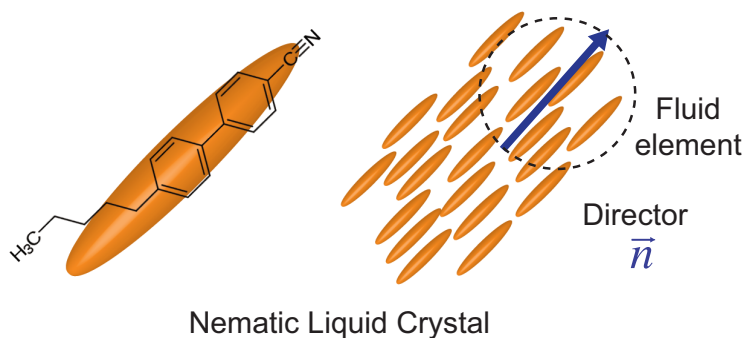
Figure 1.4: Schematic of nematic liquid crystal (NLC). A famous NLC molecule 5CB (4-Cyano-4'-pentylbiphenyl) is shown in the left figure. The orange rod indicates the elongated shape of the molecule. Also, the arrow represents the direction of director $\boldsymbol{n}$.

In addition to the local anisotropic properties, if constituent molecules of LC is chiral, macroscopic property of LC is dramatically changed. A noteworthy feature of the chiral phase of LC, called cholesteric liquid crystal (CLC), is a helical director field as depicted in Fig. 1.5. Cholesteric liquid crystal (CLC) has attracted a great

deal of attention due to such self-assembled chiral structure (Fig. 1.5). While CLC has been vigorously studied in liquid crystal (LC) physics [10], the importance of understanding CLC is growing also in other scientific fields: in biology, there are a variety of chiral bio-molecules and -supramolecules including deoxyribonucleic acid (DNA) and *fd*-virus, some of which exhibit the cholesteric phase [15, 16]. Moreover, CLC is of practical interest due to its unique optical property called the selective reflection [17, 18], in which circularly polarized light is reflected depending on the handedness and pitch of the helical structure. In contrast to these equilibrium properties, non-equilibrium behaviors have been far from understood due to the complex coupling between the chiral structure and dynamics.

When the CLC was discovered for the first time by O. Lehmann in 1900, he also reported that the texture of CLC rotated when heated from below, which is now called the "Lehmann effect [19]". His sketch of the Lehmannn effect is shown in Fig. 1.6. After his discovery, in the hydrodynamic theory of LC (the Ericksen-Leslie theory [20, 10, 14], which we introduce in Chapter 2), the Lehmann effect was predicted as the themo-mechanial coupling between the rotational motion of CLC molecules and the thermal flux, which is a cross effect emerging due to the chirality of CLC.
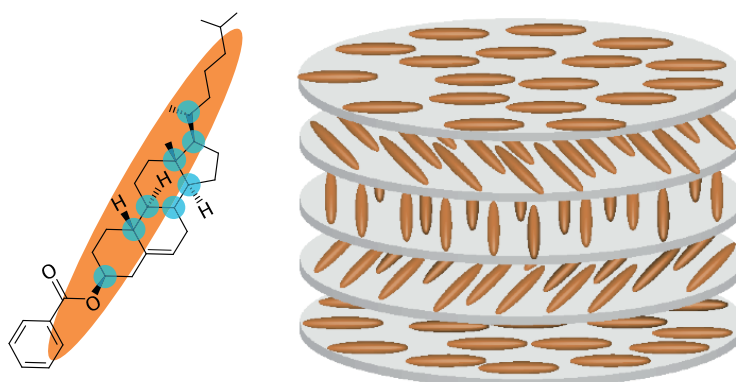
Figure 1.5: Cholesteric liquid crystal (CLC). An example of CLC molecule, cholesteric benzoate, is shown in the left figure. The carbons indicated with the blue circles are chiral carbons. The CLC exhibits helical director field as shown in the right figure.

However, until the recent seminal work by Oswald et al. [21], the Lehmann effect has not been experimentally reproduced due to the difficulty in inducing the temperature gradient to CLC precisely. Although understandings of the Lehmann effect have been advanced thanks to the seminal work and other works including analogs of the Lehmann effect, where the rotation of the CLC is induced by chemical potential gradient [22] and electric field [23], the Lehmann effect is not fully understood yet due to the few experimental observations. *Since the Lehmann effect is certainly a fundamental chirality-induced cross effect emerging in chiral fluids, elucidating the Lehmann effect should be essential to understand the role of chirality in hydrodynamics.*

Figure 1.6: Sketch of a rotating CLC droplet under a temperature gradient, which was drawn by O. Lehmann [19]. The figures in the right side are adapted from Fig. 44-49 in [19]. He reported that when 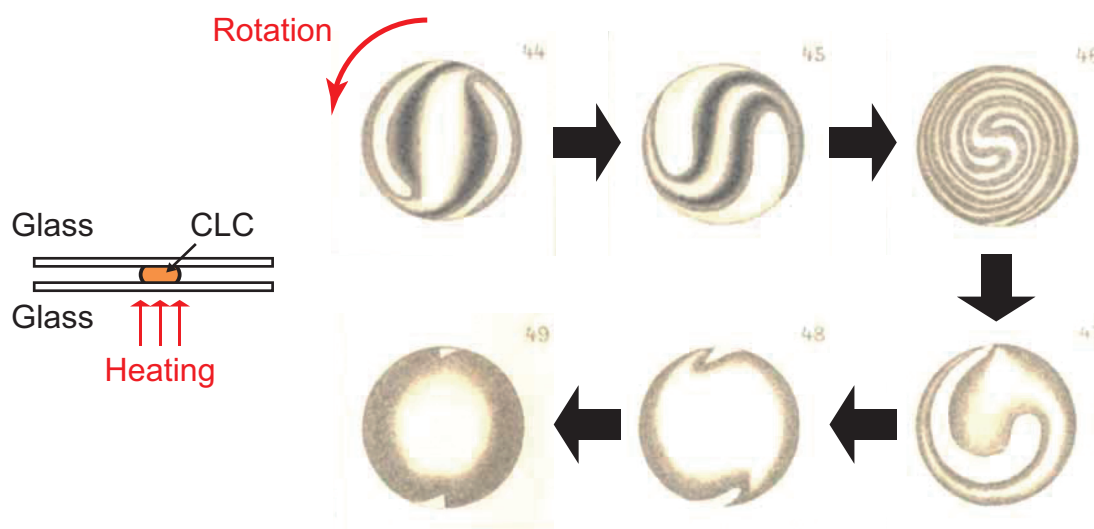a CLC droplet sandwiched between two glasses was heated from below as shown in the left figure, the texture of CLC showed anti-clockwise rotational motion [19].

In Chapter 3, we experimentally study the Lehmann effect using a hand-made chamber controlling the temperature gradient on the CLC precisely. Furthermore, we obtained 3D structural information of the CLC rotating under a temperature gradient using a 3D microscopy by a confocal microscope. One of the difficulties in investigation on the Lehmann effect was due to the lack of the 3D information of the rotating CLC droplets. In the theoretical framework of the hydrodynamics of LC, since a lot of nonlinear terms due to the anisotropy are added to the Navier-Stokes equations, it is challenging to solve the equations even numerically. Hence, we provide the phenomenological model to explain the Lehmann effect based on the concept of the hydrodynamic theory of LC utilizing the 3D structural information of the CLC obtained in our experiments.

1.3.2 Chirality-induced helical self-propulsion of CLC droplets (Chapter 4 and 5)

Although CLCs used for research and industry, nowadays, are synthesized artificially, the CLC molecule discovered for the first time, was a derivative of cholesterol which is a chiral biomolecule (Fig. 1.5). However, not only the cholesterol but most of biological molecules and supramolecules are chiral; for instance, DNA, amino acids and proteins. Hence, it is quite natural to raise a question *how such structural chirality plays roles in the biological processes.* For instance, it is intensively investigated that

molecular motors can function by converting the energy (Adenosine TriPhosphate, ATP) into a unidirectional rotational motion [6], where the chirality of the motor proteins is necessary for the coupling between the rotational motion and chemical reaction.

Due to such biomolecular chirality, also in the scales of single cells and microorganisms, they often exhibit chiral motions such as rotational [24, 25], circular [26, 27] and helical motions [28, 29] as depicted in Fig. 1.7. For instance, *volvox*, a sphere-shaped multicelluler green algae, rotates unidirectionally at the surface of water, by modulating their flagella at the surface of the body in chiral manner [24]. *E. coli* also swims in a circular path near the wall [26]. The circular motion of *E. coli* is driven by the hydrodynamic interaction between wall and rotating helical-shaped flagella. Such chiral motions of *volvox* and *E. coli* are observed when they are confined quasi-2D plane such as surface of water and near wall. In contrast, it is known that a sperm of a sea urchin swims in a 3D helical path [28, 29]. Such helical motions are considered to be derived from the rotational motion of chiral shaped flagellum. Certainly, *chirality plays essential and central roles in the dynamics of such cells and microorganisms.*
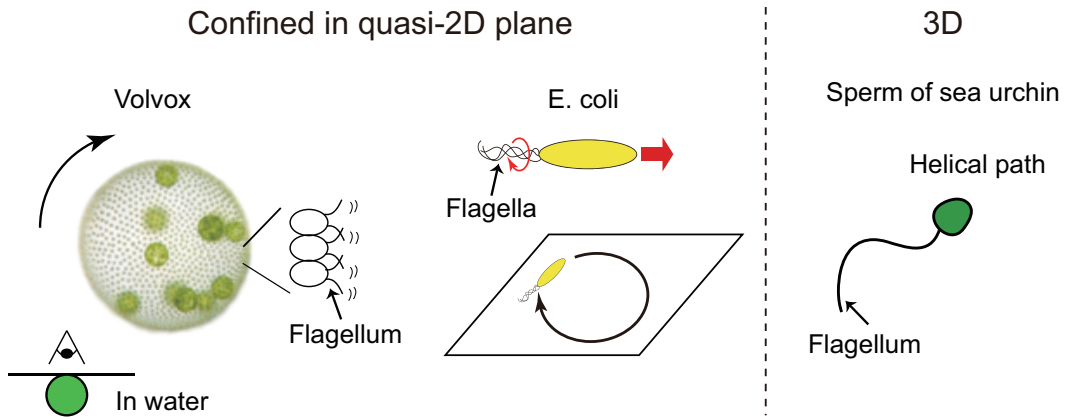
Figure 1.7: Schematic diagram of examples of microorganisms swimming in chiral manner in 2D and 3D. The picture of *volvox* is adapted from [30].

Recently, a field of physics studying the dynamics of such "Microswimmers" [31, 32, 33] which *swim spontaneously without external field in micro scale* like cells and microorganisms as we saw above, is receiving much attentions as a part of "Active matter physics" [34, 35], which are trying to elucidate the properties or laws existing in the active systems composed of self-propelled objects. In experimental studies of "Microswimmers", we can classify the types of research into two types, i.e. experiments with either "living matters" or "artificial microswimmers". While living matters exhibit very attractive and interesting features associated with the complicated activity inside their bodies, the control of experimental parameters is difficult. In contrast to such experiments with living matters, approaches with artificial microswimmers enable us to control experimental parameters and extract the physics behind the dynamics; for

instance, by changing materials, concentration of fuels of the self-propelled motion, etc.

So far, various artificial microswimmers [36, 37, 38, 31, 39], which move around without external fields such as electromagnetic field and gravity, have been invented. The first example of artificial microswimmers was proposed by W. F. Paxton et al. (Fig. 1.8) [36]. Their microswimmer was a Pt/Au bimetallic rod dispersed in aqueous hydrogen peroxide solutions. In the solution, Pt catalyzes the formation of O_2, and the concentration gradient of O_2 occurs spontaneously in the elongated direction of the swimmer as shown in Fig. 1.8. Although various mechanisms are proposed [36, 40, 41, 42], Paxton et al. claimed in [36] that fluid flow induced by a surface tension gradient due to the concentration gradient O_2 allows the microswimmer swim in the opposite direction with respect to the fluid flow toward the end of gold.
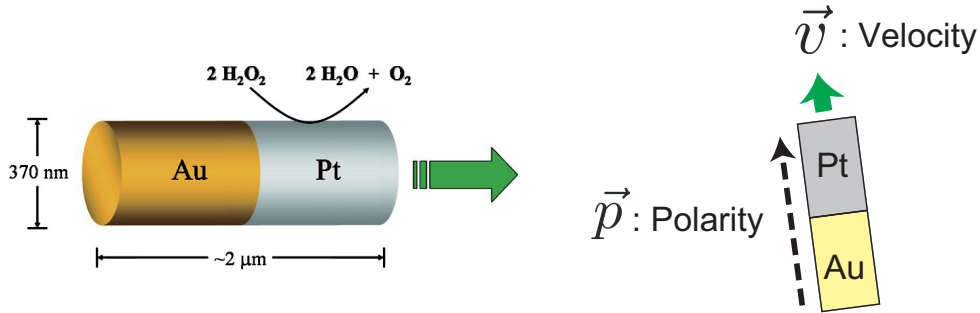

Figure 1.8: Schematic of Pt/Au microswimmer proposed by W. F. Paxton et al. [36]. The left figure is adapted from the figure in the abstract of [36]. The green arrow indicates the direction of the motion of the microswimmer. The right sketch explains the notation of the velocity and polarity of the microswimmer in 2D.

Although many artificial microswimmers have been reported after the invention of the Pt/Au mciroswimmer, reports on "chiral artificial microswimmers", which *have chiral shapes and move around without any external field*[2], have been limited [46, 47]. If any, they were limited only in 2D systems [46, 47] due to the experimental difficulty in 3D. In the seminal work on the 2D chiral microswimmer [46], the authors proposed a L-shaped bimetallic microswimmer which is chiral in 2D as shown in Fig. 1.9. Although the detail mechanism of the self-propulsion is different from that of the Pt/Au microswimmer, the L-shaped microswimmer self-propelles due to the fluid flow induced by the interfacial tension gradient which spontaneously emerges around the microswimmer. They reported such 2D artificial microswimmer shows circular motion in 2D.

Here, in the latter part of the dissertation, we investigate *how chirality plays roles in the "3D dynamics of chiral microswimmer" by proposing an artificial chiral*

---

[2]Chiral-shaped objects whose motions are controlled by external fields such as magnetic field have been reported [43, 44, 45]. Most of the reports concern the remote control of micro objects in microfluidic devices.
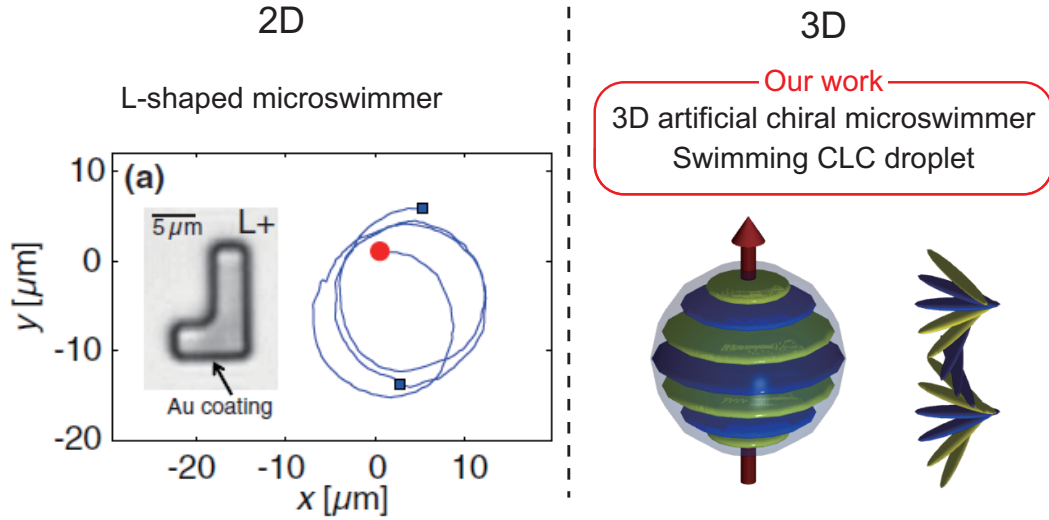
Figure 1.9: Previous and our studies on artificial chiral microswimmers in 2D and 3D. The figure of the 2D L-shaped microswimmer in the left-hand side is adapted from Fig. 1 in [46]. In contrast, there has not been realization of chiral artificial microswimmers in 3D. Our CLC droplet with helical director field is depicted in the right figure.

microswimmer, which has advantages that experimental conditions are controllable compared to living matters. In Chapter 4, we report the first experimental realization of an artificial chiral microswimmer exhibiting helical motion in 3D. We focus on the self-propelled LC droplet dispersed in a surfactant solution which moves spontaneously due to the Marangoni effect [48, 49], which is known as an effect that fluid flow is induced by a gradient of surface tension. We hypothesized that if the CLC, which can exhibit rotational motion under external fields (the Lehmann effect), is used as a LC droplet, the macroscopic motion of the CLC self-propelled droplet can exhibit chiral motions due to the chirality of CLC.

Consequently, we discovered that the CLC self-propelled droplet shows helical motion in 3D. Furthermore, we experimentally confirmed that the helical motion is derived from the chirality of CLC by investigating the handedness of the helical motion of CLC droplets with opposite chirality. The handedness of the helical motion was reversed when we changed the chirality of the CLC. In contrast, nematic LC (NLC) droplets swam only ballistically. Accordingly, we concluded that helical motions of our CLC droplets is induced by the chirality of CLC.

In Chapter 5, we construct the theoretical model of the chirality-induced helical self-propulsion of CLC droplets in 3D. In 2D case, if a microswimmer is "achiral" like Pt/Au microswimmer we saw above, the dynamics of such microswimmer are often described by a model "Active Brownian particle (ABP)" [50, 51], the concept of which

is given by,

$$\frac{d\mathbf{r}}{dt} = v_0\mathbf{p} + \sqrt{2D^T}\boldsymbol{\xi}^T(t), \tag{1.12}$$

$$\frac{d\mathbf{p}}{dt} = \sqrt{2D^R}\boldsymbol{\xi}^R(t) \times \mathbf{p}, \tag{1.13}$$

where $\mathbf{r}$ and $\mathbf{v}$ represent the position and velocity of the swimmer, D^T, D^R denote the diffusion constant for translation and rotation, and a unit vector $\mathbf{p}$ is defined as the polarity of the swimmer since the particle is asymmetric in the elongated direction (Fig. 1.8). v_0 is the mean velocity. Also, Gaussian white noises $\boldsymbol{\xi}^T(t)$ and $\boldsymbol{\xi}^R(t)$ are added to represent the translational and rotational diffusion. The rescaled noise terms are introduced to safisfy $< \boldsymbol{\xi}^{T,R}(t) >= 0$ and $< \boldsymbol{\xi}^{T,R}(t_1) \otimes \boldsymbol{\xi}^{T,R}(t_2) >= \mathbf{1}\delta(t_1 - t_2)$. Note that $\mathbf{v} \perp \boldsymbol{\xi}^R$ in 2D. Since the model assumes low Reynolds number (explained in Chapter 5), the inertia of the swimmer is neglected in the ABP model.

Such phenomenological models are powerful approach to describe the dynamics of the microswimmers since it is quite tough to solve hydrodynamic equations including the relevant field variables such as concentration field. Especially, the hydrodynamic equations of LC is almost impossible to solve analytically. Thus, we construct our model of CLC droplets phenomenologically.

Our model is based on the concept of a phenomenological model originally constructed by T. Ohta et al. to describe the dynamics of deformable cells [52]. We constructed a coupled time-evolution equations in terms of a velocity, an angular velocity and a tensor variable representing the symmetry of the helical director field of the droplet. Our model reveals that the nonlinearity of the model equations and the chiral coupling terms between the velocity and the angular velocity play a crucial role in the emergence of the helical swimming of the droplet.

1.4   Outline of the dissertation

In Chapter 2, we review the Lehmann effect and the Ericksen-Leslie theory, which is a hydrodynamic model of LC. In Chapter 3, we report our experimental results and phenomenological model on the Lehmann effect. In Chapter 4, we report our experimental discovery of the chirality-induced helical self-propulsion of CLC droplets. In Chapter 5, we report our theoretical model on the chirality-induced helical self-propulsion of CLC droplets. Finally, we remark conclusion and future perspectives in Chapter 6.

Chapter 2

Review of the Lehmann effect and hydrodynamics of cholesteric liquid crystal

After O. Lehmann discovered the rotational motion of a CLC droplet under a temperature gradient in 1900 as shown in Fig. 1.6 [19], a hydrodynamic theory of LC, which is now called the Ericksen-Leslie theory (ELT [10]), predicted the Lehmann effect. In the first half of this chapter, we overview the ELT.

In contrast to the proposal of the theory for the Lehmann effect and related theoretical predictions [53, 54, 55], the Lehmann effect has not been reproduced until Oswald et al. constructed an appropriate experimental system in 2008 [21]. In the latter part of this chapter, we overview essential experimental reports after the seminal work by Oswald et al. [21].

2.1 Ericksen-Leslie theory

First, we introduce the Frank elastic energy and molecular field, which play crucial roles in the ELT. In this chapter, we underline the terms which cannot appear in NLC but exist only in CLC for clarity.

2.1.1 Frank elastic energy

When we construct the hydrodynamic equations of LC, degrees of freedom of director $n = (n_x, n_y, n_z)$, which is the average orientational direction of LC molecules in a fluid element, should be taken into consideration in addition to the velocity field $v = (v_x, v_y, v_z)$ (See Fig. 1.4). Here, n is a unit vector. In the case of nematic liquid crystal, since LC molecules tend to align in the same direction, we may introduce the following elastic energy density, which is called Frank elastic energy,

$$f_{\text{nem}} = \frac{1}{2}K_1(\nabla \cdot n)^2 + \frac{1}{2}K_2(n \cdot (\nabla \times n))^2 + \frac{1}{2}K_3(n \times (\nabla \times n))^2, \qquad (2.1)$$
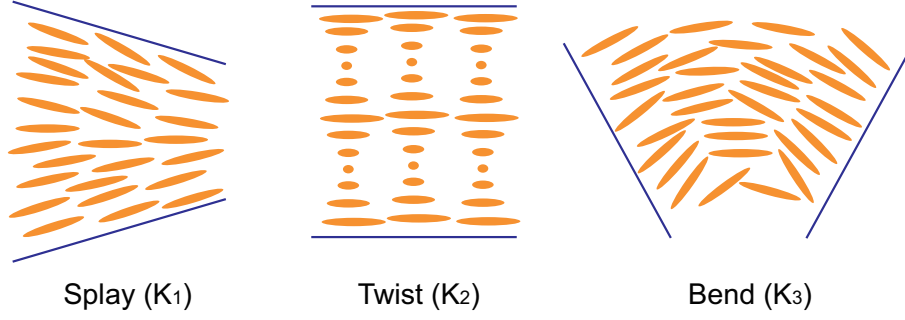
13

Figure 2.1: Distortion of the director field corresponding to the Frank elastic terms in Eq. (2.1) [10].

where K_1, K_2, K_3 are Frank's elastic constants, respectively. The origin of each term is the distortion of the director field as shown in Fig. 2.1.

In CLC, we need a following additional term describing the twisting director field of CLC,

$$f_{\mathrm{d}} \;=\; f_{\mathrm{nem}} + \underline{K_2 q_0 \boldsymbol{n} \cdot (\nabla \times \boldsymbol{n})}, \tag{2.2}$$

where q_0 is a pseudo scalar parameter which is allowed only in chiral systems. Due to the term with q_0, CLC exhibits helical director field with pitch $P = 2\pi/q_0$ in equilibrium without external fields.

Here, the ELT is formulated with director represented by a unit vector $\boldsymbol{n}$. Hence, the ELT is not applicable to the situation associated with the phase transition and topological defects, where the director cannot be defined by $\boldsymbol{n}$. To overcome these drawbacks in the ELT, other formulations, so called Beris-Edwards equation [56] and Qian-Sheng equation [57], are established using the second rank symmetric tensor representing the director field which is given by [56, 57, 58],

$$Q_{ij} = \frac{S}{2}(3 n_i n_j - \delta_{ij}) + \frac{P}{2}(e_i^{(1)} e_j^{(1)} - e_i^{(2)} e_j^{(2)}), \tag{2.3}$$

where S is the uniaxial order parameter which represents the nematic degree of order, P is the biaxial order parameter which represents the degree of the biaxiality, and δ_{ij} is the Kronecker delta. $\boldsymbol{n}, \boldsymbol{e}^{(1)}$ and $\boldsymbol{e}^{(2)}$ are the eigenvectors of Q_{ij} corresponding to the eigenvalues $S, -\frac{1}{2}(S + P)$ and $\frac{1}{2}(S + P)$. In the case of uniaxial NLC, P vanishes and the eigenvectors $\boldsymbol{e}^{(1)}, \boldsymbol{e}^{(2)}$ degenerate. Hence, the tensor order parameter is denoted as,

$$Q_{ij} = \frac{S}{2}(3 n_i n_j - \delta_{ij}). \tag{2.4}$$

In this formulation, isotropic phases and cores of defects can be represented by $S = 0$. Nevertheless, in the following sections, we explain the hydrodynamics of LC using $\boldsymbol{n}$ just for simplicity.

2.1.2 Molecular field

The molecular field, which is an elastic torque exerted on director field, is introduced from the Frank elastic energy. In equilibrium state, director field $n(r)$ is determined to minimize the Frank elastic energy of a whole system under a constraint $|n|^2 = 1$ according to variational principle. Representing the elastic energy F of a whole system as a functional of director field $n(r)$, we obtain,

$$F[n(r)] = \int f_d(n, \nabla n) dV. \tag{2.5}$$

Considering an arbitrary variation of the director field $n(r) \to n(r) + \delta n(r)$, we have,

$$\begin{aligned} \delta F &= F[n(r) + \delta n(r)] - F[n(r)] \\ &= \int \left\{ \frac{\partial f_d}{\partial n_\alpha} - \frac{\partial}{\partial x_\beta} \pi_{\beta\alpha} \right\} \delta n_\alpha dV + \text{(Surface integral)}, \end{aligned} \tag{2.6}$$

where we follow the Einstein summation convention and, $\pi_{\beta\alpha}$ is defined as follows,

$$\pi_{\beta\alpha} = \frac{\partial f_d}{\partial(\partial n_\alpha/\partial x_\beta)}. \tag{2.7}$$

Defining a molecular field $h(r)$ as follows,

$$h_\alpha = -\frac{\partial f_d}{\partial n_\alpha} + \frac{\partial}{\partial x_\beta} \pi_{\beta\alpha}. \tag{2.8}$$

In most practical cases, surface forces are strong enough to make director align in a preferred direction. Hence, we only need to minimize the bulk terms in Eq. (2.6) with some fixed boundary conditions. Thus, neglecting surface terms in Eq. (2.6), we can write,

$$h_\alpha = -\frac{\delta F}{\delta n_\alpha(r)}. \tag{2.9}$$

We find that the molecular field $h(r)$ is the elastic force torque on the director field.

2.1.3 Ericksen-Leslie theory

The Ericksen-Leslie theory was constructed using the molecular field $h(r)$ introduced above. In Chapter 1, we showed that, in the framework of the non-equilibrium thermodynamics, the derivation of the hydrodynamic equation starts from writing an entropy production σ as products of fluxes and thermodynamic force. Extending the argument for a 1-component isotropic fluid in Chapter 1, entropy production σ of CLC under a temperature gradient G is given as,

$$T\sigma = A : \sigma^s + h \cdot N + J \cdot G, \tag{2.10}$$

where A is a symmetric part of velocity gradient tensor ∇v, σ^s is a symmetric part of viscous stress tensor, h is a molecular field, N is a rotational velocity of director field relative to the rotation of fluid, J is a thermal flux and G is a temperature gradient. These quantities are explicitly written as,

$$A_{\alpha\beta} = \frac{1}{2}(\partial_\alpha v_\beta + \partial_\beta v_\alpha), \tag{2.11}$$

$$N = \dot{n} - \omega \times n, \; \omega = \frac{1}{2}\nabla \times v, \tag{2.12}$$

$$G = -\frac{\nabla T}{T}, \tag{2.13}$$

where $\dot{n}$ is material derivative. In the framework, we represent fluxes as linear combinations of thermodynamic forces. However, the choice of fluxes and thermodynamic forces are arbitrary. Here, we take A, N, G as thermodynamic forces and σ^s, h, J as fluxes.

Besides, Curie principle in Chapter 1 requires us to take into consideration the spatial symmetry of the system when we write the linear combination. Since LC does not have polarity in average, either n or $-n$ should describe the same state. Considering such symmetry with respect to the operation $n \leftrightarrow -n$, we obtain,

$$\sigma'_{\alpha\beta} = \sigma^H_{\alpha\beta} + \underline{\mu_1 n_\alpha (G \times n)_\beta + \mu_2 n_\beta (G \times n)_\alpha}, \tag{2.14}$$

$$h = h^H + \underline{\nu n \times G}, \tag{2.15}$$

$$J = \sigma_\perp G + (\sigma_\parallel - \sigma_\perp)(n \cdot G)n + \underline{\nu n \times N - (\mu_1 + \mu_2)n \times (A \cdot n)}. \tag{2.16}$$

Here, σ^H and h^H are fluxes in the absence of a temperature gradient, and written as,

$$\sigma^H_{\alpha\beta} = \alpha_1 n_\alpha n_\beta n_\mu n_\rho A_{\mu\rho} + \alpha_4 A_{\alpha\beta} \quad + \quad \alpha_5 n_\alpha n_\mu A_{\mu\beta} + \alpha_6 n_\beta n_\mu A_{\mu\alpha}$$
$$+ \quad \alpha_2 n_\alpha N_\beta + \alpha_3 n_\beta N_\alpha, \tag{2.17}$$

$$h^H_\mu = \gamma_1 N_\mu + \gamma_2 n_\alpha A_{\alpha\mu}, \tag{2.18}$$

where $\alpha_1 \sim \alpha_6$ are called the Leslie coefficients, γ_1, γ_2 are viscosity, and ν, μ_1, μ_2 are called *the Lehmann coefficients which are pseudo scalar coefficients introduced to explain the Lehmann effect.* Furthermore, we have following relations between these transport coefficients due to the Onsager's reciprocal theorem[1],

$$\gamma_1 = \alpha_3 - \alpha_2, \tag{2.19}$$

$$\gamma_2 = \alpha_2 + \alpha_3 = \alpha_6 - \alpha_5, \tag{2.20}$$

$$\nu = \mu_1 - \mu_2. \tag{2.21}$$

---

[1]In the absence of a magnetic field B, transport coefficient matrix L satisfies $L_{ij} = L_{ji}$ [11].

Using the representations for the fluxes in Eqs. (2.14)-(2.16) and conservation laws for momentum and angular momentum, the following time-evolution equations for the velocity field v and the director field n are obtained as,

$$\begin{aligned}
\rho \frac{dv_\beta}{dt} &= \partial_\alpha(\alpha_1 n_\alpha n_\beta n_\mu n_\rho A_{\mu\rho} + \alpha_4 A_{\alpha\beta} + \alpha_5 n_\alpha n_\mu A_{\mu\beta} + \alpha_6 n_\beta n_\mu A_{\mu\alpha} \\
&\quad + \alpha_2 n_\alpha N_\beta + \alpha_3 n_\beta N_\alpha + \underline{\mu_1 n_\alpha (G \times n)_\beta + \mu_2 n_\beta (G \times n)_\alpha} + \sigma^e_{\alpha\beta}), \quad (2.22) \\
h_\mu &= \gamma_1 N_\mu + \gamma_2 n_\alpha A_{\alpha\mu} + \underline{\nu(n \times G)_\mu}. \quad\quad (2.23)
\end{aligned}$$

We find that Eq. (2.23) is a time-evolution equation for n, since N is defined as Eq. (2.12). In Eq. (2.22), σ^e is called Ericksen stress and written as,

$$\sigma^e_{\beta\alpha} = -\pi_{\beta\gamma}\partial_\alpha n_\gamma - p(r)\delta_{\alpha\beta}, \quad\quad (2.24)$$

where $p(r)$ is a Lagrangean multiplier introduced to satisfy the incompressibility. Importantly, since the Ericksen stress is derived from the elasticity of LC, it does not contribute to the dissipation of the system.

2.1.4 Symmetry of LC phase and the Lehmann effect

We showed above how to construct a set of hydrodynamic equations of CLC under a temperature gradient. Here, we consider the effect of the symmetry of LC phase on the model equations. Since the transport coefficients μ_1, μ_2, ν introduced in Eq. (2.14)-(2.16) are *pseudo scalars*, these coefficients vanish in the NLC due to the reflection symmetry. Hence, in the case of NLC, we obtain,

$$\nu = \mu_1 = \mu_2 = 0. \quad\quad (2.25)$$

Consequently, couplings between a temperature gradient and director field cannot occur in NLC but only in CLC. The Lehmann effect was predicted as such chiral coupling terms in the framework of the ELT.

2.1.5 Application of the ELT on the Lehmann effect

Here, we introduce an application of the ELT in a simple setup of CLC under a temperature gradient to understand the chiral terms. Since the model equations are highly nonlinear, we can solve the dynamics analytically only in a few setups.

Consider the situation where the CLC is subjected to a temperature gradient G which is parallel to the helical axis of the CLC as shown in Fig. 2.2. In this case, we can exceptionally solve the equations, since the velocity field does not appear and we only need to consider the director field n as stated in [10]. We verify this fact in Appendix A. However, note that, *velocity field generally appears in the dynamics governed by the ELT* as we can readily find if looking at the model equations.

We define ψ as the angle between the director field $\boldsymbol{n}$ and x-axis as depicted in Fig. 2.2. Rewriting Eq. (2.23) with the spatial variable ψ, we obtain,

$$\gamma_1 \frac{\partial \psi}{\partial t} = K_2 \frac{\partial^2 \psi}{\partial z^2} + \underline{\nu G}. \tag{2.26}$$

where $G = |\boldsymbol{G}|$. To solve Eq. (2.26), we need to assume some boundary condition. Here, we assume a boundary condition, where the CLC is bounded between two glasses perpendicular to the temperature gradient. In addition, we assume that the surface of the glass has weak anchoring effect and molecules can freely rotate at the surface. In such a case, the boundary condition at the surface of glasses are given as [10],

$$\left.\frac{\partial \psi}{\partial z}\right|_{z=0} = \left.\frac{\partial \psi}{\partial z}\right|_{z=D} = q_0, \tag{2.27}$$

where $z = 0$ and $z = D$ is the z-coordinates of two glasses, and q_0 denotes the wave number of the helical structure of CLC in equilibrium state. Equations (2.26) and (2.27) provide analytically,

$$\psi(z, t) = q_0 z - \frac{\nu G}{\gamma_1} t + \text{const.} \tag{2.28}$$

Hence, we find that the rotational velocity $\dot{\psi} = \omega$ of the director field is given as,

$$\dot{\psi} = \omega = -\frac{\nu G}{\gamma_1}. \tag{2.29}$$
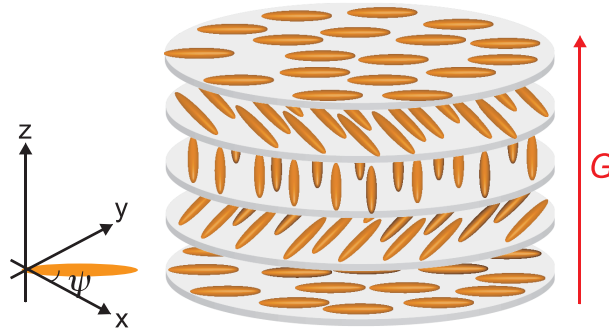

Figure 2.2: A simple configuration where the temperature gradient $\boldsymbol{G}$ is parallel to the helical axis of CLC in z-direction. The definition of the coordinates applied here is shown schematically in the left figure.

2.2   The Lehmann effect reproduced by Oswald et al.

We overview the seminal experimental work on the Lehmann effect by Oswald et al. [21].

2.2.1   Experimental setup

The authors prepared an experimental setup which can apply a temperature gradient perpendicularly to a liquid crystal cell as shown in Fig. 2.3 [21]. They controlled temperatures of the upper and bottom sides of the LC cell by flowing temperature-controlled waters. They prepared LC sample by sandwiching CLC between two glasses whose surfaces are treated with epoxy hardener which can make the glass surface sliding planar anchoring conditions, where the LC molecules rotate freely [59].
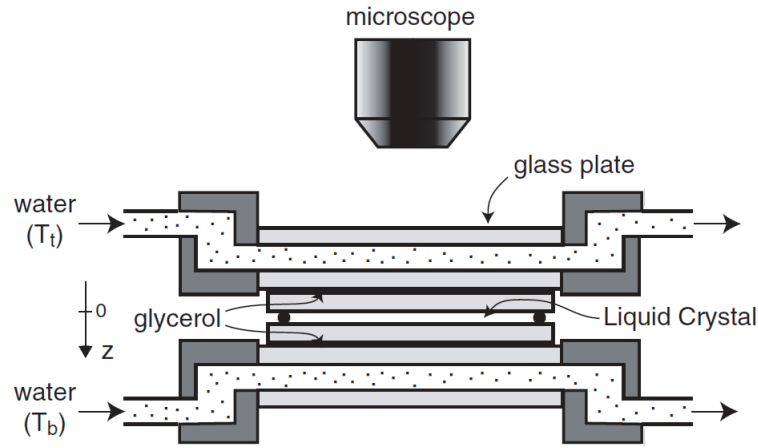

Figure 2.3: Schematic of the temperature controlling chamber devised by Oswald et al. [21]. They controlled a temperature gradient induced on a LC cell by flowing temperature-controlled water. The image was adapted from Fig. 1 in [21].

2.2.2   Results

As shown in Fig. 2.4, they realized rotating CLC droplets which coexist with the isotropic phase by setting average temperature between the temperatures of upper and bottom sides near the isotropic-cholesteric phase transition temperature. The droplets they observed had the striped patterns which correspond to the periodic helical director field, where *the helical axis is parallel to the glasses.*

They also found that the rotational velocity of the droplet depends on the diameter of the droplet as shown in Fig. 2.5. The larger droplets showed slower rotational motion. They explained the trend using the ELT by *assuming that there is no velocity field.* With the assumption of no flow, they rewrote Eq. (2.23) as follows:

$$\gamma_1 \frac{\partial \boldsymbol{n}}{\partial t} = \boldsymbol{h} + \underline{\nu \boldsymbol{n} \times \boldsymbol{G}}. \tag{2.30}$$
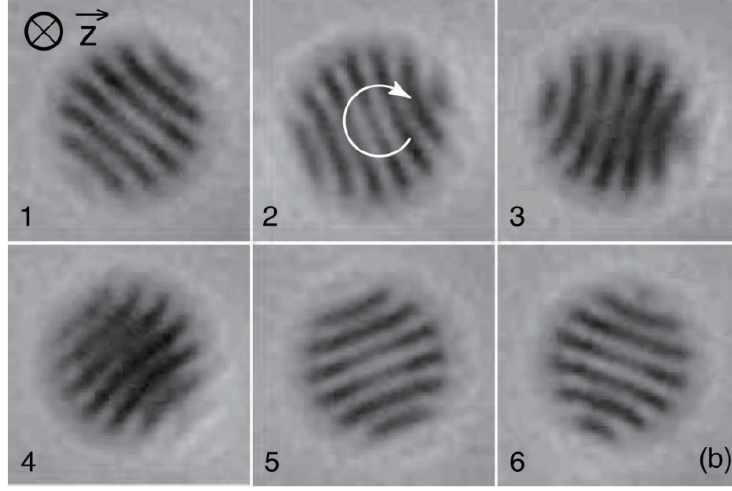
Figure 2.4: Time evolution of a rotating CLC droplet (Diameter $D \sim 12.5\ \mu$m) with a striped pattern observed by Oswald et al. [21]. The striped pattern corresponds to the helical director field of the CLC, and the droplet is surrounded by the isotropic phase of CLC. The direction of the temperature gradient is in z-direction perpendicular to the glasses as shown in the first picture. The image was adapted from Fig. 2 in [21].
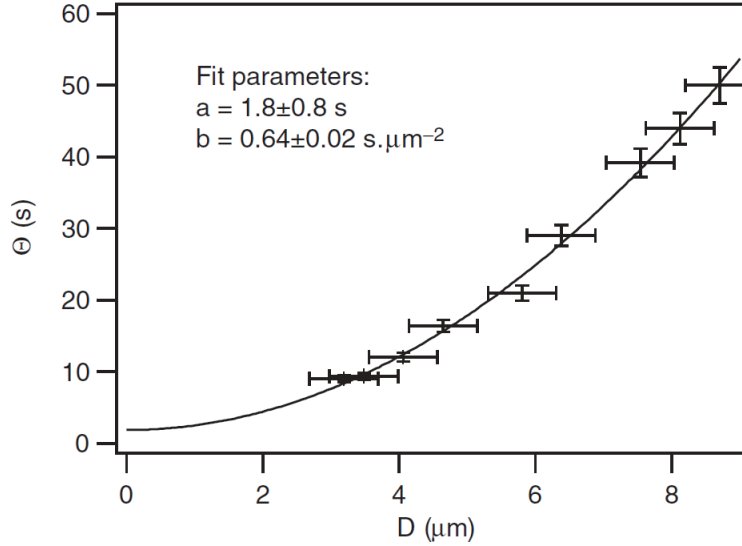
Figure 2.5: Period Θ of rotation vs. diameter D of CLC droplets. The data were fitted using Relation (2.36). The figure was adapted from Fig. 4 in [21].

Furthermore, since the striped pattern itself did not change during the rotation, they considered that the total Frank elastic energy is constant during the rotation. Hence, they obtained,

$$\frac{d}{dt} \int_{\text{drop}} f_d \, dV = 0,$$

(2.31)

where the integral was taken over the volume of the droplet. Thus, using Eq. (2.9), they obtained,

$$-\frac{d}{dt} \int_{\text{drop}} f_d \, dV = -\int_{\text{drop}} \frac{\delta f_d}{\delta n} \cdot \frac{\partial n}{\partial t} \, dV = \int_{\text{drop}} h \cdot \frac{\partial n}{\partial t} \, dV = 0.$$

(2.32)

According to Eq. (2.30), they obtained,

$$\int_{\text{drop}} h \cdot \frac{\partial n}{\partial t} \, dV = \int_{\text{drop}} \left\{ \gamma_1 \frac{\partial n}{\partial t} - \nu n \times G \right\} \cdot \frac{\partial n}{\partial t} = 0.$$

(2.33)

Since they observed the rotation of the striped texture with a constant angular velocity ω, they obtained the time-evolution equation of n as follows,

$$\frac{\partial n}{\partial t} = \omega e_z \times n - \omega \frac{\partial n}{\partial \theta},$$

(2.34)

where e_z is a unit vector representing the z-direction and θ is the polar angle. In addition, as they imposed a temperature gradient in z-direction, defining the temperature gradient as $G = Ge_z$, they obtained,

$$-\frac{\nu G}{\gamma_1 \omega} = 1 + \frac{\iiint_{\text{drop}} \left[e_z \cdot \frac{\partial n}{\partial \theta} \times n + \left(\frac{\partial n}{\partial \theta} \right)^2 \right] dV}{\iiint_{\text{drop}} \left[e_z \cdot \frac{\partial n}{\partial \theta} \times n + 1 - (e_z \cdot n)^2 \right] dV}.$$

(2.35)

Consequently, they can calculate the right-hand side by assuming a director field $n(r)$ and a shape of the droplet. Actually, they assumed a periodic modulation of the director field with a pitch $P = 2\pi/q$ and a cylindrical shape [21]. Finally, they obtained the following relation between diameter and rotational velocity applying some approximations,

$$-\frac{\nu G}{\gamma_1 \omega} - 1 \propto D^2.$$

(2.36)

The data in Fig. 2.5 is well fitted with this relation.

However, *the assumption of no velocity field* had not been confirmed experimentally at that time.

Furthermore, in [60], the authors investigated the effect of strength of chirality on the Lehmann effect by changing the ratio of chiral dopant, which control the pitch of the helical director field. As a result, they reported that the rotational velocity is almost proportional to the strength of the chirality which is measured by the wave number q of the helical director field.

2.3   Another type of CLC droplet

In [21], Oswald et al. observed the CLC droplets with striped pattern as shown in
Fig. 2.4, which we call "striped droplet" in this dissertation. In the striped droplet, *the
helical axis was speculated to be parallel to the glasses.*

However, another type of droplet was observed in 2014 [61, 62]. Fig. 2.6 shows the
droplets, which we call "target droplet" in this dissertation. The target droplets showed
oscillation of the target pattern, which corresponds to rotation of the helical director
field, where *the helical axis of CLC is speculated to be perpendicular to the glasses.*

Note that this configuration is the situation we considered in Sec. 2.1.5 (Fig. 2.2).
By measuring the periodicity of the oscillation of texture, the authors in [61, 62]
respectively measured the rotational velocity. In [62], the rotational velocity was
independent on the sizes of the target droplet as predicted in Eq. (2.29). In contrast,
the rotational velocity in [61] was inversely proportional to the diameters. The
authors in [61] speculated that the reason why the rotational velocity did not follow
Eq. (2.29) in their experiments is that there may be other mechanisms of rotation of CLC
droplets than the thermo-mechanical couplings predicted in Eq. (2.29). As a possible
mechanism, they mentioned a Marangoni effect due to the gradient of interfacial tension
at the surface of the droplets. However, the contradiction in experimental results in
[61, 62] has not been clarified yet.
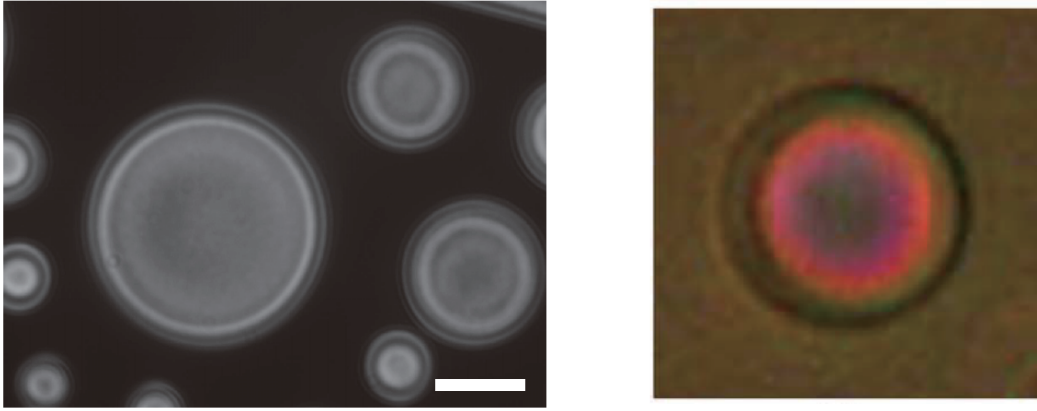
Figure 2.6: Target droplets observed in [61] and [62]. Each figure is adapted from
Fig. 3 in [61] and Fig. 2 in [62], respectively. In the left figure, the scale bar is 30 μm.
Meanwhile, we speculate the size of the droplet in the left figure is around 15 μm.

2.4   Observation of the velocity field in the rotating CLC droplet by Yoshioka et al.

While *the assumption of no velocity field* worked well in the arguments in [21], it
is essential to experimentally investigate the hydrodynamic field inside the droplet.

Although there had been no established method to observe the hydrodynamic field without disturbing the director field, Yoshioka et al. recently measured the hydrodynamic field inside the striped and target droplet by photobleaching method [62] as we depict schematically in Fig. 2.7. As shown in Fig. 2.8, they reported that *the flow field in the rotating target droplet is negligible, while the CLC droplet with striped pattern had the rotating flow inside and rotated as a rigid body.* Note that this observation for the striped droplet is contradictory to *the assumption with no flow* in [21].
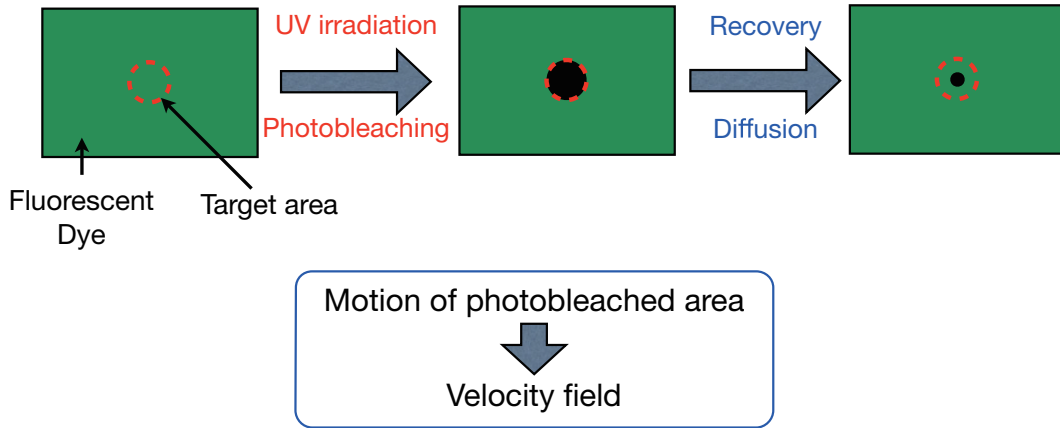
Figure 2.7: Schematic picture of photobleaching method proposed by Yoshioka et al. [62]., which enables us to observe hydrodynamic field in LC.
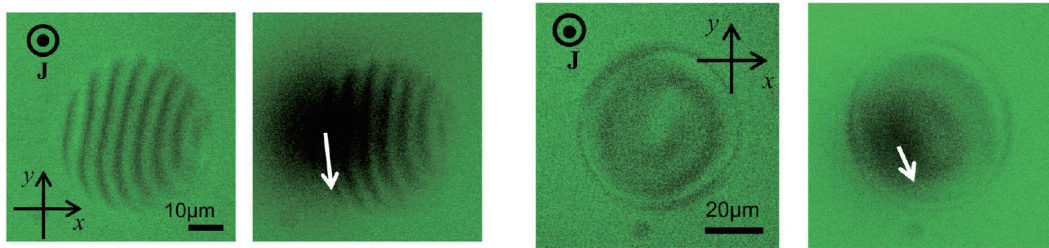
Figure 2.8: Results of photobleaching of a striped droplet (two images in the left) and a target droplet (two images in the right) [62]. The white arrows in the figures indicate the direction of the motion of the photo bleached region. Note that, although the white arrow is shown in the target droplet, the authors claimed that the motion of the bleached area is negligible comparing the motion in the striped droplet. The images are adapted from Fig. 4 and Fig. 6 in [62], respectively.

Yoshioka et al. also observed the 3D structure of the striped droplet by using the fluorescence confocal polarizing microscopy (FCPM [63], we will explain in Chapter 3) as shown in Fig. 2.9. They reported that the shape of striped droplet is semi-sphere and it has a uniform helical director field, where the helical axis is parallel to the glasses. Also,

they claimed that the *convex-concave modulation exists on the surface of the striped droplet* (Fig. 2.9). Consequently, the authors conjectured that *the surface torque on the striped droplet* due to such convex-concave modulation may exist in the case of the rotation of the striped droplet.
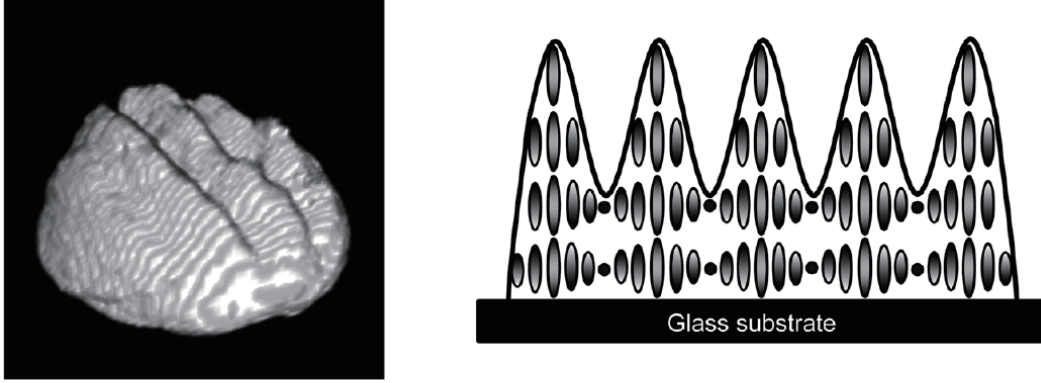
Figure 2.9: Structure of the striped droplet observed using a confocal fluorescence microscopy by Yoshioka et al. [62]. The reconstructed 3D structure of a striped droplet is shown in the left, while the schematic picture is depicted in the right. Each figure is adapted from Fig. 7 and Fig. 8 in [62], respectively.

2.5 Remarks

After the seminal work by Oswald et al. [21]., the three other works on the rotation of the CLC droplets [60, 61, 62], which we overviewed in this chapter, had been reported before our work in this dissertation. Nevertheless, we are now far from complete understanding of the Lehmann effect, as we encountered some incompatibilities between each work. In Chapter 3, we show our motivations and experimental works on the Lehmann effect.

2.6 Appendix A: Flow field when a temperature gradient is parallel to the helical axis of CLC

In [10], the authors remark that flow field of CLC vanishes when an external field G is parallel to the helical axis of the CLC. Here, we verify it. We define the viscous stress σ^{Lehmann} induced by an external field G in Eq. (2.22) as follows:

$$\sigma_{\alpha\beta}^{\text{Lehmann}} = \underline{\mu_1 n_\alpha (G \times n)_\beta + \mu_2 n_\beta (G \times n)_\alpha}. \tag{2.37}$$

Considering the helical axis is parallel to G, we denote the directer field and the external field as $n = (n_x(z), n_y(z), 0)$ and $G = (0, 0, G)$. Substituting $n = (n_x(z), n_y(z), 0)$ and $G = (0, 0, G)$ in the Eq. (2.37), we obtain,

$$\sigma_{\alpha\beta}^{\text{Lehmann}} = \frac{1}{2}(\mu_1 + \mu_2)G \begin{pmatrix} -2n_x n_y & n_x^2 - n_y^2 & 0 \\ n_x^2 - n_y^2 & -2n_x n_y & 0 \\ 0 & 0 & 0 \end{pmatrix} + \frac{1}{2}\nu G \begin{pmatrix} 0 & 1 & 0 \\ -1 & 0 & 0 \\ 0 & 0 & 0 \end{pmatrix}. \tag{2.38}$$

Since n_x and n_y is functions of only z, we find $\partial_\alpha \sigma_{\alpha\beta}^{\text{Lehmann}} = 0$. Hence, if there is no flow field in the initial state, no flow field occurs.

Chapter 3

Experiment on the Lehmann effect

In this chapter, we investigate the Lehmann effect [19], which is one of the unsolved non-equilibrium phenomena of CLC.

3.1 Introduction

In 1900, O. Lehmann observed the rotating texture of a CLC sample heated from below (Fig. 1.6). After his discovery, the Lehmann effect was predicted in the framework of the Ericksen-Leslie theory (ELT, described in the section 2.1) as a cross effect induced by thermo-mechanical coupling between rotational motion of director and temperature gradient. In general, chiral symmetry breaking enables the coupling of axial vectorial fluxes and polar vectorial thermodynamic forces, which are not coupled in the achiral system [64]. Since the ELT, there have been some theoretical studies [65, 66, 67] about the Lehmann effect including a fascinating prediction about its application as a microscopic pump [67]. In contrast, there are still only few experiments [62, 60, 21, 61] after the first reproductive experiment reported in [21]. In [21], Oswald et al. have successfully observed the rotation of CLC droplets by making a device which can induce temperature gradient perpendicular to the LC cell as shown in Fig. 2.3. The CLC droplets were realized in the coexisting region between isotropic and cholesteric phase near the clearing point as shown in Fig. 2.4.

In previous studies [62, 60, 21, 61], two types of rotating CLC droplets have been investigated. One is the "striped droplet" which shows a striped pattern in the bright-field microscopy (BFM) image, which is reminiscent of the fingerprint pattern of CLC (Fig. 3.1(a)). The other one is the "target droplet" with concentric target pattern (Fig. 3.1(b)), which is called "CC-type droplet" in [62]. Interestingly, the rotational velocity of these droplets depends differently on their size [62, 60, 21, 61]. Moreover, it has been deduced from the BFM observation that they have different directions of the helical axes with respect to the temperature gradient: perpendicular for the striped droplets, parallel for the target droplets (Fig. 3.1). Therefore, *we considered that the angle between the helical axis and the temperature gradient may be a key to understand the mechanism of the rotating CLC droplets. So, how can we change this angle?*
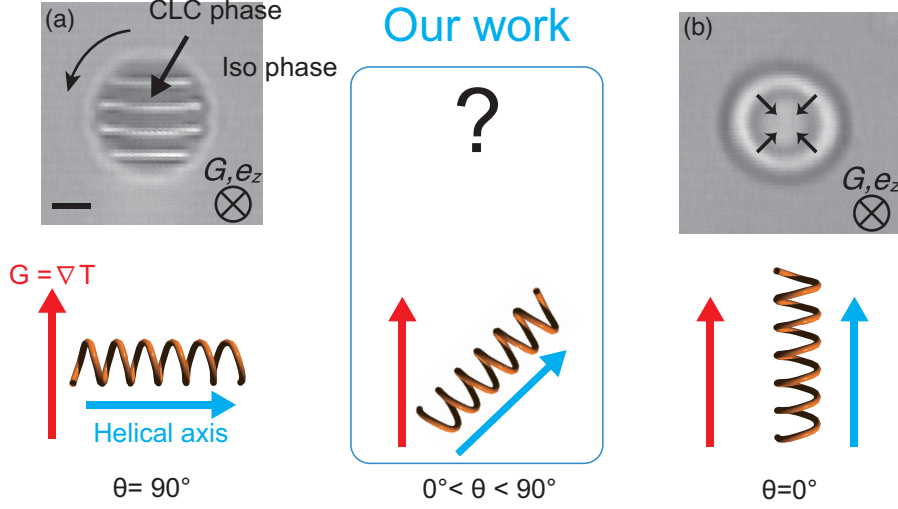
Figure 3.1: Rotating CLC droplets under a temperature gradient, whose textures had been already reported before our study [62, 60, 21, 61]. A striped droplet whose helical axis was speculated to be perpendicular to the temperature gradient is shown in (a). A target droplet whose helical axis was speculated to be parallel to the temperature gradient is shown in (b). The direction of the temperature gradient G is indicated in each image. The scale bar is 10 μm.

Here, we report that the anchoring condition of the LC plays a crucial role for the geometry of CLC droplets. While the droplets in [62, 60, 21, 61] were observed in either planar cells or cells with bare glasses, we observed a novel type of rotating CLC droplet whose helical axis tilted from the temperature gradient with an intermediate angle between 0 and $\pi/2$ in homeotropic cells. We call this droplet the "stripeless droplet", because the striped pattern could not be observed with BFM as shown in Fig. 3.6(c). As we show below, the stripeless droplet showed an anomalous dependence of the rotational velocity on the diameter (Fig. 3.9).

For the quantitative analysis of the rotational behaviors, the three-dimensional (3D) information on the droplet structures, such as the shapes and director field, is essential. However, the usual imaging technique by BFM provides only 2D images which do not contain the full 3D information of the sample. Here, we determined the 3D structures of all the three types of the droplets by utilizing the fluorescence confocal polarizing microscopy (FCPM [63]), which is one of the powerful 3D imaging techniques developed recently for LC [63, 68]. On the basis of the 3D structural information of the droplets obtained by FCPM, we constructed a phenomenological equation that explains the rotational behaviors of the three types of droplets (Eq. (3.9)).

3.2 Experimental setup for the observation of the Lehmann effect

3.2.1 Temperature controlling chamber

As shown in Fig. 3.2, we prepared the temperature controlling chamber to induce a temperature gradient perpendicularly to a cell for the BFM observations (40×, IX71, OLYMPUS). The temperature of the chamber was controlled by temperature-controlled circulating water (RE630G, LAUDA). As summarized in Table 3.1, the fluctuation in the temperature of circulating water measured by Pt100 resistance thermometer in the top and bottom chambers (T_t and T_b) is ± 0.002 K (for the period of our observations, ~ 3 min). That for the average temperature T_{ave} is ± 0.001 K. The corresponding raw data for the time evolution of T_t, T_b and T_{ave} are shown in Fig. 3.3. Also, the absolute accuracy of the temperature difference $\Delta T = T_t - T_b$ is ± 0.02 K by using calibrated Pt100 thermometers.

In our experiments, we evaluated the temperature gradient $\boldsymbol{G} = G\boldsymbol{e}_z$ ($\boldsymbol{e}_z$: unit vector to z-direction) across the LC layer using the typical thermal conductivities of glass ($\kappa_g \sim$ 1.05 W/K · m) and LCs ($\kappa_{LC} \sim$ 0.15 W/K · m [69]). The detail calculation is shown in Appendix A.
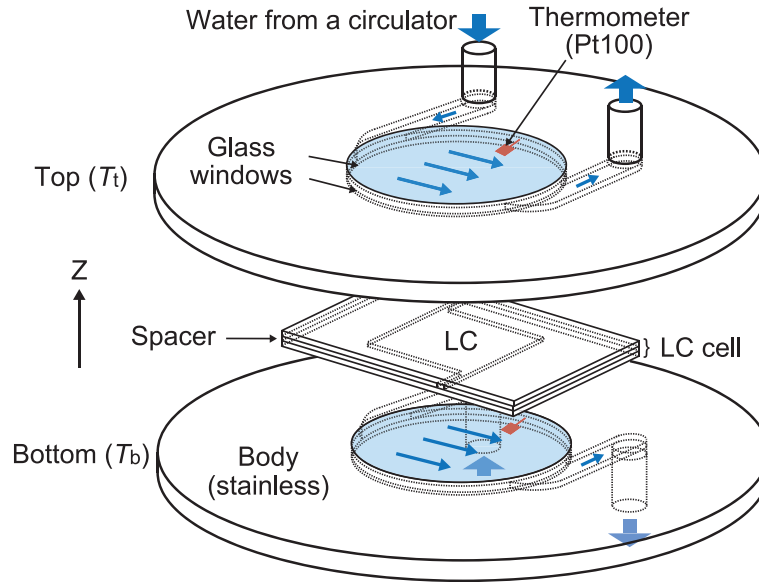
Figure 3.2: Schematic of the temperature controlling chamber. Circulating water flows between glass windows, whose thickness are 0.5 mm. We used glycerol to improve the thermal contact between the chambers and LC cells. The z-direction is defined as the direction of optical axis. The figure is adapted from Fig. 2 in [70].

Sensor	Set temperature (°C)	Avarage (°C)	Standard deviation (K)
T_t	53.84 (± 0.01)	53.732	0.002
T_b	54.96 (± 0.01)	54.731	0.002
T_{ave}	-	54.231	0.001

Table 3.1: Time average and standard deviation of measured temperature ($\Delta T = -1.0$ K).

(a)

(b)

(c)
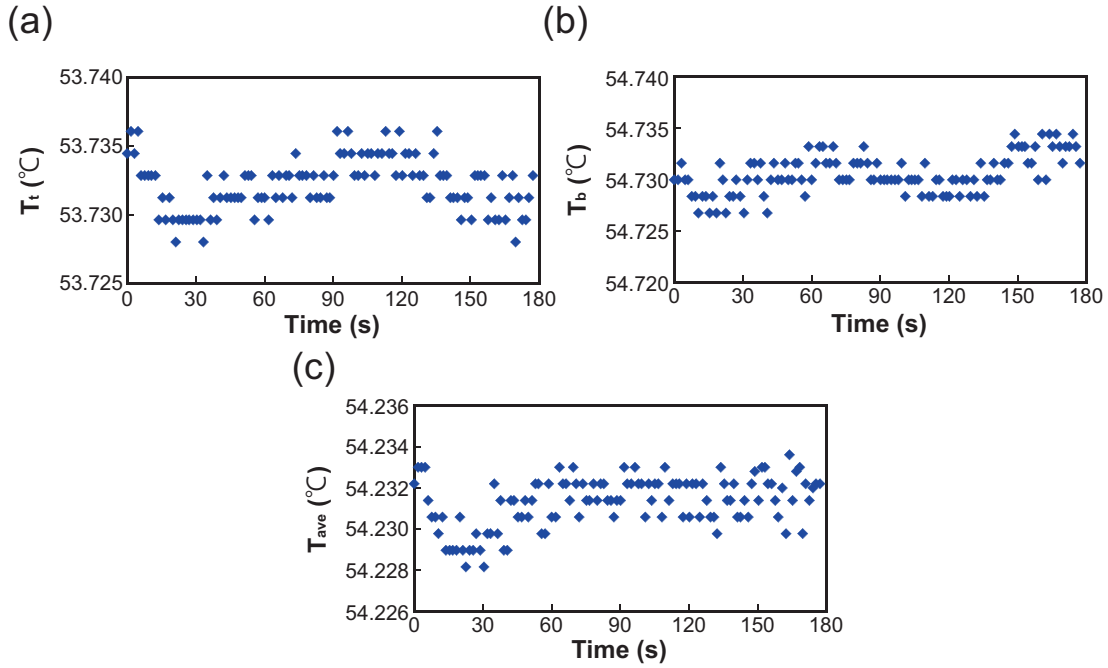
Figure 3.3: Time evolution of measured temperatures T_t, T_b and T_{ave}. The corresponding time average, standard deviation and the set temperatures of the circulators are summarized in Table 3.1.

3.2.2   Preparation of cell

Our LC cells were prepared with either planar anchoring or homeotropic anchoring, which are schematically depicted in Fig. 3.5. For planar anchoring, we modified the surface of glasses with the polymercaptan hardener of an epoxy glue (Epoxy+ from Eleco) following [59]. It has been reported that the hardener provides the planar and sliding anchoring condition [59]. For homeotropic anchoring, we modified the glass surface with *N,N*-dimethyl-*N*-octadecyl-3-aminopropyltrimethoxysilyl chloride (DMOAP) following the protocol in [71]. The detailed procedure is in Appendix A. A mixture of MLC-2039 (73.7wt%, Merck Ltd) and 4-cyano-4'-octylbiphenyl (24.5wt%, 8CB, WAKO) doped with chiral dopant R-811 (1.8wt%, WuXi AppTec Co., Ltd) was used as the CLC sample and enclosed in the LC cells. Here, a LC cell was composed of two cover glasses (the thickness is $\sim$ 0.5 mm for BFM and $\sim$ 0.15 mm for FCPM) sandwiching 25 μm polyester films as a spacer as shown in Appendix B. 8CB was added to lower the clearing point T_{cl} of the sample to a moderate temperature $\sim$ 69°C. We added to the LC sample a small amount of *N,N'*-bis(2,5-di-*tert*-butylphenyl)-3,4,9,10-perylenedicarboximide (0.01wt%, BTBP, Sigma-Aldrich) only as the fluorescent dye for FCPM. Also, a small optical anisotropy of MLC-2039 (Δn = 0.08) improved the resolution of FCPM.

8CB
4'-Octyl-4-biphenylcarbonitrile

R-811
Benzoic acid, 4-(hexyloxy)-4,
[[[(1R)-1-methylheptyl]oxy]carbonyl]phenyl ester

BTBP
N, N' -bis(2,5-di-tert-butylphenyl)
-3,4,9,10-perylenedicarboimide
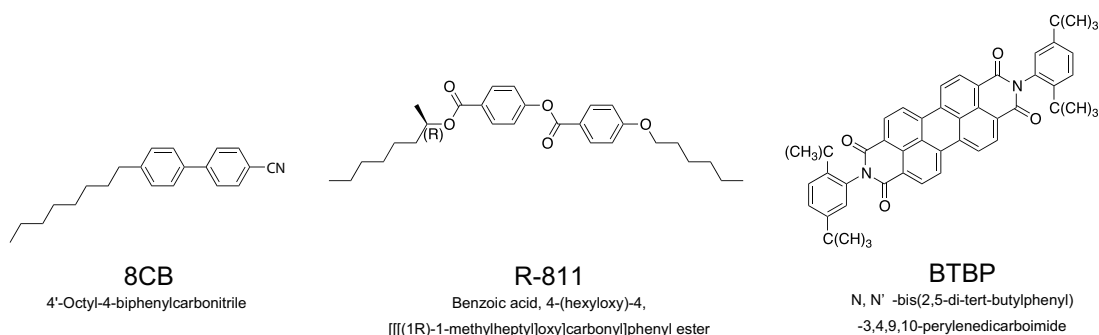
Figure 3.4: Chemical structures of materials.

Planar anchoring   Homeotropic anchoring
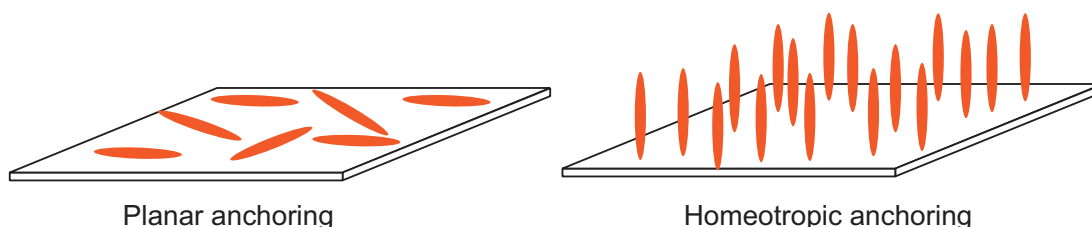
Figure 3.5: Schematic images of planar and homeotropic anchorings.

3.3   Results

We observed the three types of rotating CLC droplets under a temperature gradient as shown in Fig. 3.6. The droplets which coexist with the isotropic phase, were realized by setting the average temperature $T_{ave} = (T_t + T_b)/2$ around their clearing point T_{cl} (phase transition temperature from isotropic phase to cholesteric phase).
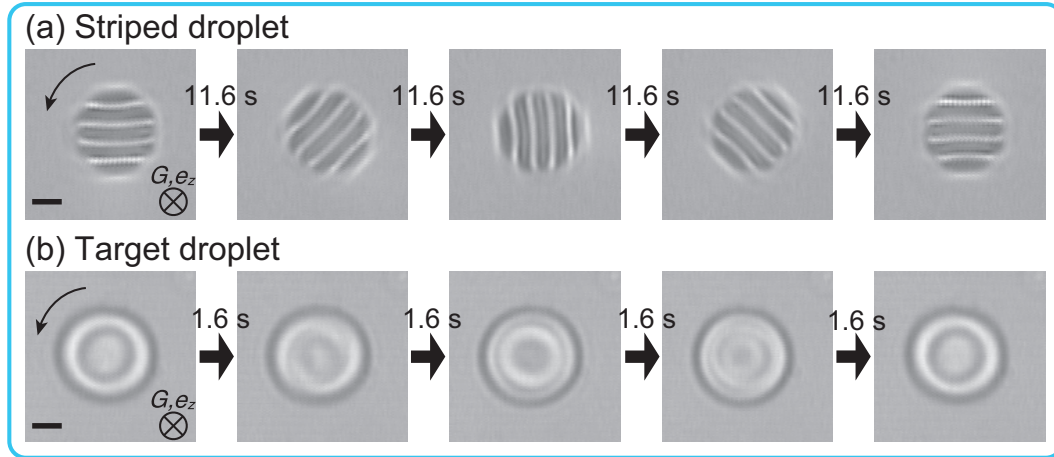
Figure 3.6: Three types of rotating CLC droplets under temperature gradient (BFM image). For the planar anchoring condition, (a) striped droplets and (b) target droplets (with a polarizer) are observed. For the homeotropic condition, stripeless droplets are observed, as shown in (c). ΔT is adjusted to ~ 2K (G ~ 6400 K/m). The curved arrows indicate the rotational directions and the length of the scale bar is 5 μm.

3.3.1   Planar cell

In the planar cell, striped droplets and target droplets coexisted (Fig. 3.6(a)(b)). The striped droplets rotate with their striped pattern (Fig. 3.6(a)), while the target pattern of the target droplets propagates radially when observed with a single polarizer (Fig. 3.6(b)). As confirmed by our FCPM observations, the helical axis of the target droplet is perpendicular to the glass and the director field homogeneously rotates around

the z-axis. Accordingly, the intensity of the transmitted light in the target droplet changes periodically depending on the phase of the director n when observed with a polarizer. As for the rotational velocity $\boldsymbol{\omega} = \omega \boldsymbol{e}_z$ of the target droplet, we calculated $|\omega|$ as $|\omega| = \pi f$, in terms of the frequency f of the oscillating intensity of the transmitted light at the center of the target pattern. This π (not 2π) periodicity is derived from the invariance of the optical property of the CLC under the transformation n into $-n$. We confirmed this and also the sign of ω by mechanically rotating the polarizer for the target pattern not to propagate ($\omega < 0$ when $G > 0$).

The practical method for the measurement of the oscillation is as follows.

1. Extract the 4 pixels × 4 pixels (1 pixel = 0.23 μm, ×40 objective) at the center of the target droplet (Fig. 3.7)

2. Average the intensity of the extracted pixels and plot the time vs. intensity (Fig. 3.8(a)).

3. Fourier transform of the time series of the averaged intensity (Fig. 3.8(b))

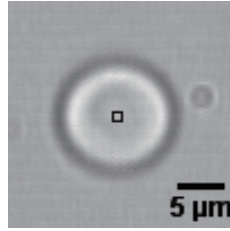Figure 3.7: Sampling of the central square (4 pixels×4 pixels).
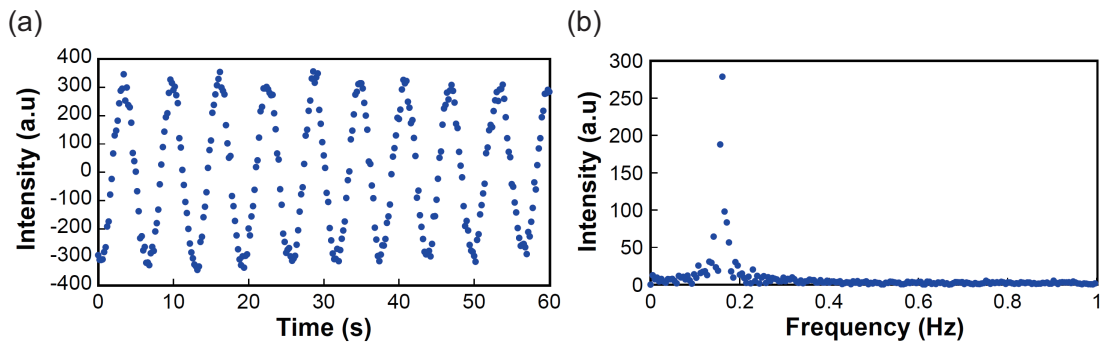
Figure 3.8: (a) An example of the time-evolution of the averaged intensity of sampled pixels as shown in Fig. 3.7 ($\Delta T \sim 2$ K). (b) Fourier transform of the time series in (a).

3.3.2   Homeotropic cell

In the homeotropic cell, we observed rotation of stripeless droplets (Fig. 3.6(c)) and "non-rotating" striped droplets, which have a striped pattern as well as the rotating striped droplets observed in planar cells. The texture of the stripeless droplet is similar to that of the target droplet but does not have rotational symmetry. We will discuss a possible reason for the non-rotating nature of the striped droplet in Sec. 3.6.4.

3.3.3   Summary of rotational velocity of the CLC droplets

Figure 3.9 shows the rotational velocities of the three types of droplets which were measured using BFM. We found that the normalized rotational velocity $-\omega/G$ strongly depended on the diameter D of the droplets. Here, D was changed by controlling T_{ave}. Intriguingly, it turned out that the three types of droplets exhibited totally different trends; $-\omega/G$ of the target droplet is constant, while that of the striped droplet decreases with increasing diameter. These trends are consistent with previous studies [62, 60, 21]. In contrast, the stripeless droplets with larger diameter have larger $-\omega/G$. Note that we could not observe the stripeless droplets with $D < 9\ \mu$m.
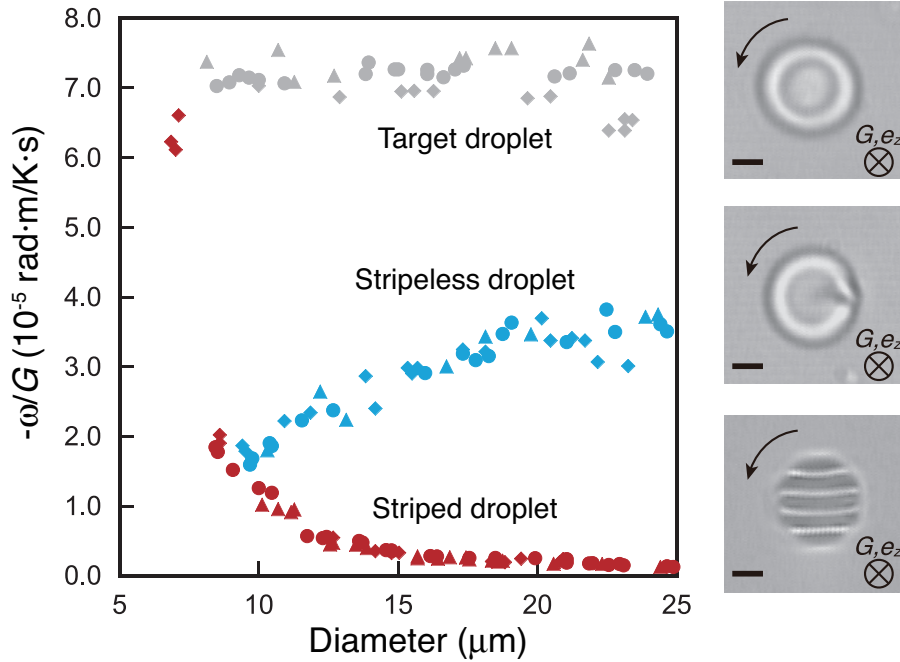
Figure 3.9: Normalized rotational velocity $-\omega/G$ vs. diameter D for the three kinds of droplets: the target droplet (gray), the stripeless droplet (blue) and the striped droplet (red). The image of each droplet is shown for clarity. Each symbol corresponds to different values of the temperature difference ΔT (triangle: 2 K, bullet: 4 K and diamond: 6 K). The scale bars are 5 μm. The left figure is adapted from Fig. 3 in [70].

3.4 Fluorescence confocal polarizing microscopy (FCPM)

In the following section, we determine the 3D structures of the rotating droplets using fluorescence confocal polarizing microscopy (FCPM [63]). FCPM was invented to determine the 3D director field of LC. FCPM utilizes the anisotropy of fluorescence of dye molecules. The intensity of fluorescence of a dye molecule depends on the angle α between the transition moment of a molecule and the direction of polarization of excitation light (Fig. 3.10). The intensity I_f of fluorescence is proportional to $\cos^2 \alpha$. In FCPM experiments, we mix LC sample and a small amount of rod-like dye molecules BTBP which can align with the direction of LC molecules. Regarding the optical system, the LC sample is scanned three-dimensionally by a confocal microscope (Fig. 3.11). Finally, we know the 3D orientation of molecules from the fluorescence intensity I. Both the incident light and the fluorescence are polarized in the same direction using a common polarizer to enhance the contrast of images. Accordingly, I is proportional to $\cos^4 \alpha$.

Figure 3.10: Principle of FCPM. The dye molecule can align in the same direction as the LC molecules. We can detect the direction of the LC molecules by using polarized excitation light, since the intensity of fluorescence depends on the angle between the dye molecule and polarization.
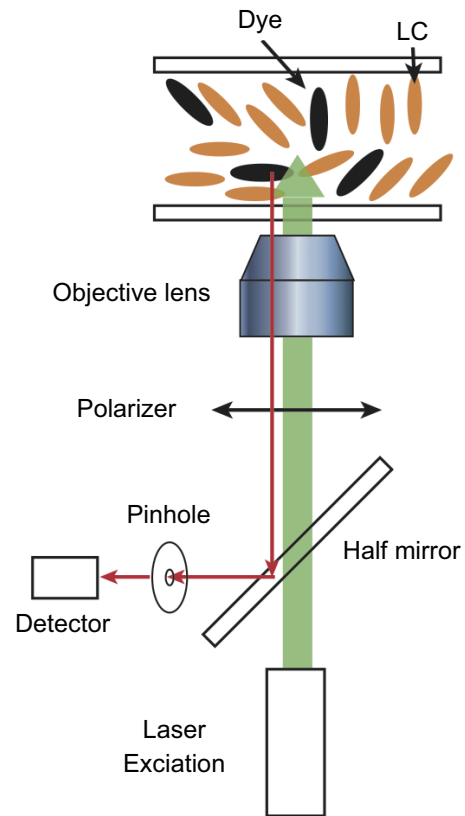
Figure 3.11: Optical system of FCPM.

In FCPM, the resolution of images strongly depends on the anisotropy of optical

index of LC, since the excitation light is divided into the ordinary and extraordinary light with different velocity in anis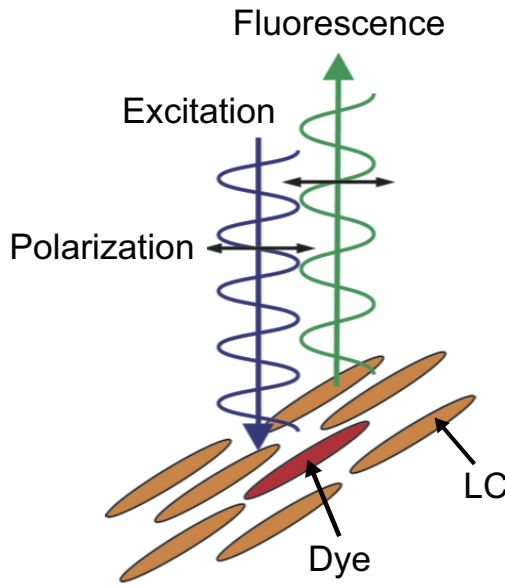tropic medium, which provides blurring of images. The spatial resolution Δx is estimated as $\sim g(\Delta n/n_{\mathrm{av}})d$ [63]. Here, g is a coefficient of $O(1)$ dependent on the configuration of samples. d, Δn and n_{av} denote the depth in z direction, difference of optical indexes between ordinary and extraordinary light and the average of them, respectively. Although the blur is inevitable in principle, we can suppress the blur using appropriate LC materials with low optical anisotropy. When $\Delta n = 0.05$ and $d = 20$ μm, Δx is suppressed to ~ 1 μm. In our experiments, we used such an appropriate LC material with low optical anisotropy to suppress the blur of images.

3.5   Our experimental setup of FCPM

In FCPM, we used an inverted fluorescence confocal microscope (SP-5, Leica) with an oil-immersion objective lens ($\times$63). Due to the short working distance of the objective lens, the bottom temperature controlling chamber was unavailable in FCPM. Therefore, we controlled the temperature of the objective lens itself by another handmade chamber with circulating water, while the temperature of the top glass of the cell was controlled by the chamber in Fig. 3.2. Although the accurate evaluation of G was difficult in this setup, we took FCPM images at G (> 0) of the same order of that in BFM.
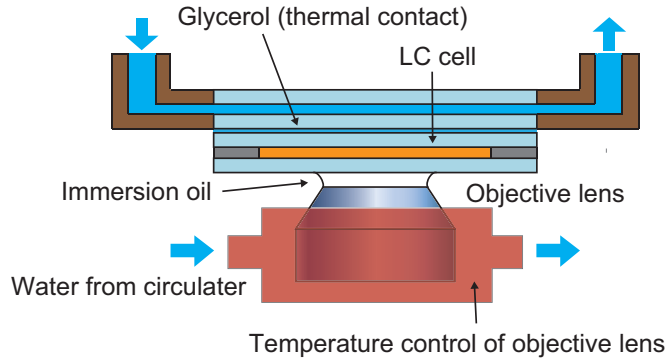
Figure 3.12: Temperature controlling chamber in our FCPM experiments.

3.6   Determination of 3D structures of CLC droplets using FCPM

As a first step for understanding these puzzling rotational behaviors, we determined the 3D structures of the droplets by FCPM. Using linearly polarized light for the excitation, we detected the fluorescent signal from the rod-shaped dye (BTBP) which aligned in the direction of n. The n field was determined from the signal, which depends on the

angle between the transition dipole of the dye and the polarization [63]. The direction of polarization and the optical axis were defined respectively as y- and z-axis. The cross-sectional (xz-plane passing through the center of the droplet) FCPM images of the droplets are shown in Fig. 3.13. The bottom dark part of each image indicates the colder glass attached to the oil-immersion objective lens ($G > 0$). Note that, Yoshioka et al. reported that the striped droplet has hemispherical shape as shown in Fig. 2.9 [62], and Oswald et al. assumed the cylindrical shape in their analysis [21]. However, we found that the shapes of all the rotating droplets were almost spherical and they attached to the colder glass with contact angles larger than 90°. Since Yoshioka et al. used bare glasses for the experiments [62], the difference of the shapes of the striped droplets is probably derived from the difference on surface conditions.
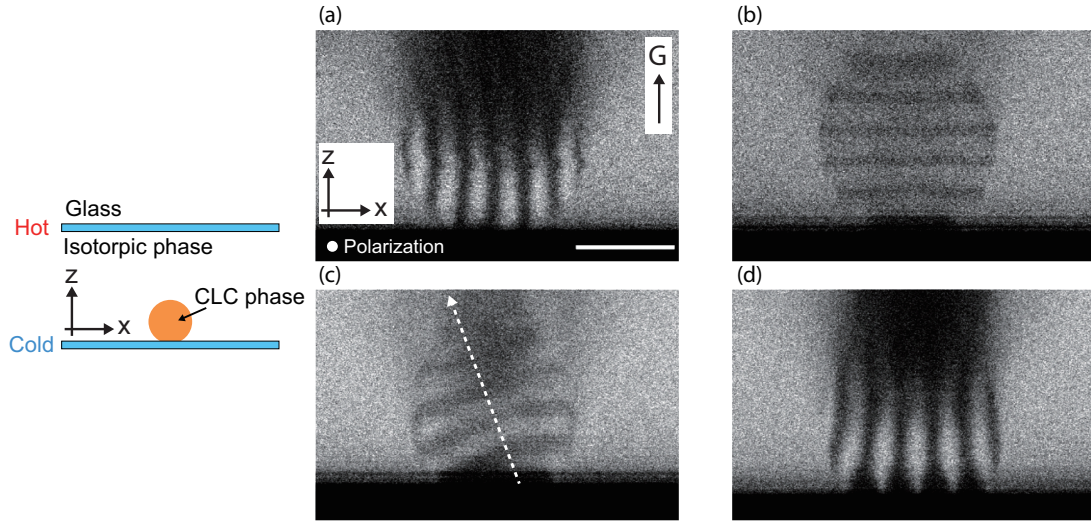
Figure 3.13: Cross-sectional (xz-plane) images of FCPM: (a) the striped droplet (planar), (b) target droplet (planar), (c) stripeless droplet (homeotropic) and (d) non-rotating striped droplet (homeotropic). The bottom dark part of each image indicates the colder glass ($G > 0$). The direction of the linear polarization is indicated in (a). The dashed arrow in (c) shows a direction of helical axis. The scale in z-direction was reduced (×0.83) based on the helical pitch of the striped droplet measured in (a). The length of the scale bar is 10 μm. The figures (a)-(d) are adapted from Fig. 4 in [70].

3.6.1 Striped droplet

Figure 3.13(a) shows the result for the striped droplet in the planar cell. It turned out that the striped droplet had its helical axis parallel to the glass. In this geometry, the upper half of the striped pattern is blurred by lensing due to the birefringence of LCs. The n field of the striped droplet does not seem to be deformed even near the glass. This can be attributed to the weak anchoring effect of the planar and sliding anchoring [59].

3.6.2   Target droplet

We also observed the FCPM image of the rotating target droplet (Fig. 3.13(b)). The striped pattern in the xz-plane propagated in z-direction as shown in Fig. 3.14, while the target pattern was propagating radially in the xy-plane. This means that the helical axis is perpendicular to the glass and the n field homogeneously rotates around the z-axis. Considering that the striped pattern in the xz-plane propagated toward the z-direction, and that ω was negative, we can also know that our CLC sample had a right-handed helix.

3.6.3   Stripeless droplet

As shown in Fig. 3.13(c), we found that the striped pattern was also present in the cross-sectional image of the stripeless droplet. However, the axis of the striped pattern tilted from the z-axis and the striped pattern propagated to the z-direction with the tilt angle changing periodically like seesaw motion as shown in Fig. 3.15(a). Therefore, we concluded that, in 3D, the helical axis of stripeless droplets tilted from and precessed around the z-axis. A schematic of the stripeless droplet with the tilt angle ϕ is shown in Fig. 3.15(b). Note that $\phi = 0$ and $\phi = \pi/2$ correspond respectively to the target droplet and striped droplet.

3.6.4   Non-rotating striped droplet in the homeotropic cell

In Fig. 3.13(d), we show the result for the non-rotating striped droplet in the homeotropic cell. The width of the dark region of the striped pattern near the glass is wider than that in the bulk, which means that the n field deforms near the glass. Hence, we consider that the non-rotating nature is originated from the pinning effect due to the strong anchoring effect on the striped droplet in the homeotropic cell. In contrast, we consider that the n field of the stripeless droplet near the glass was almost homeotropic due to its moderate tilt angle. Therefore, the pinning effect would have little effect on the rotational motion of the stripeless droplet.

3.7   Phenomenological model

In the following, we account for the size-dependence of the rotational velocity obtained in Fig. 3.9. It is known that the ELT is one of the powerful theories describing the LC dynamics. However, it is, in general, almost impossible to solve the equations analytically, and numerical simulation of the dynamics is also tough, since the ELT includes complicated couplings among the n field and the hydrodynamic field. Therefore, we describe the phenomena more phenomenologically, following the basic ideas in the ELT.

Figure 3.14: Time evolution of FCPM cross-sectional images for a rotating target droplet. The dashed circle in each image indicates the edge of the same band, which propagates in the z-direction. The scale bar is 10 μm.
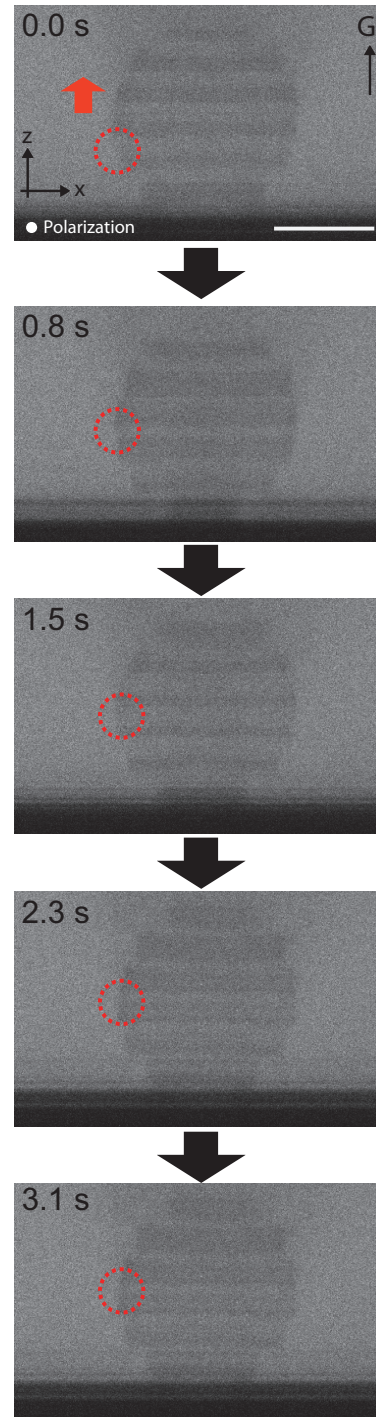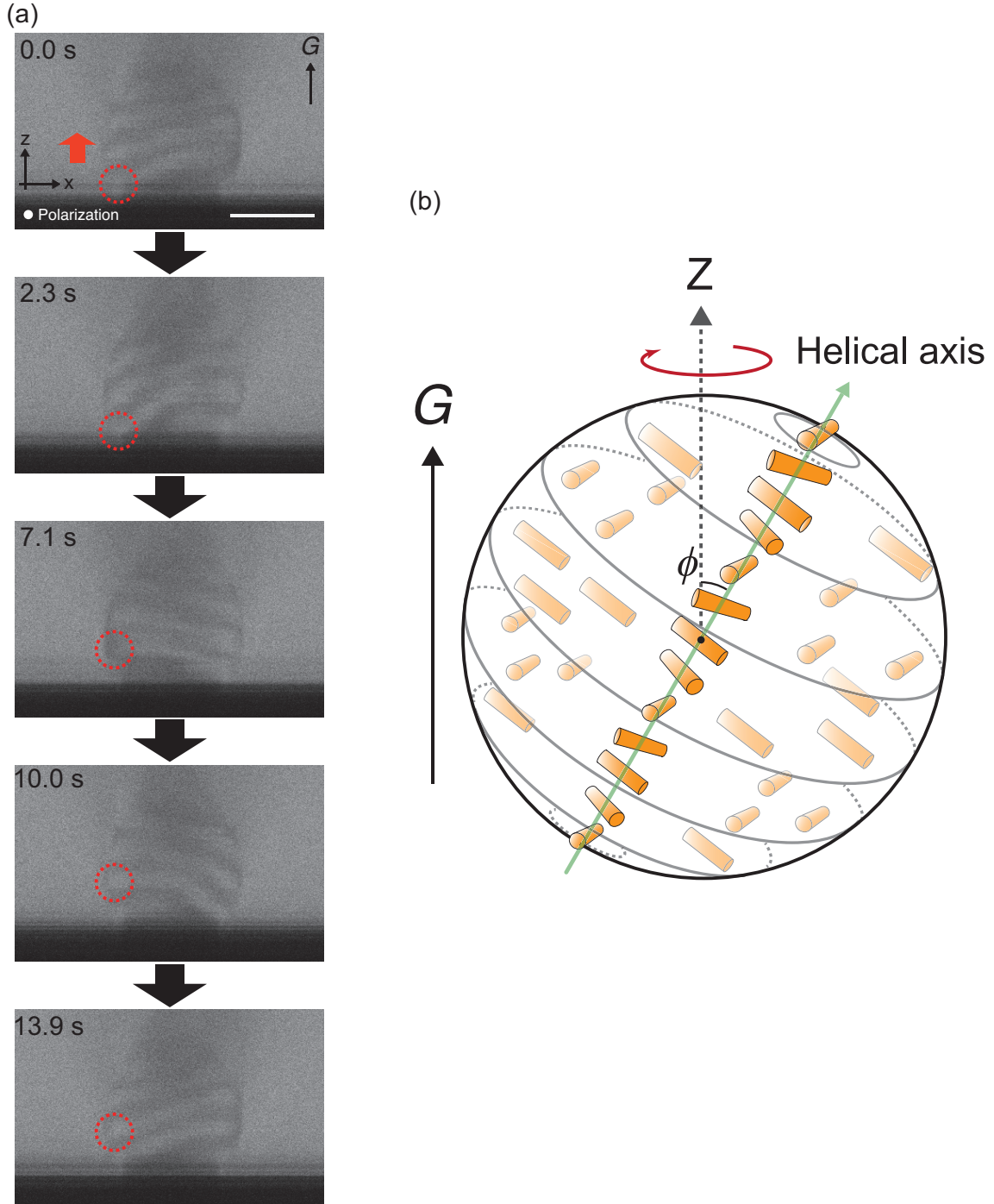
(a)

(b)

Figure 3.15: (a) Time evolution of the cross sectional FCPM images of a stripeless droplet. The dashed circle in each image indicates the edge of the same band, which propagate in the z direction. The scale bar is $10\,\mu$m. (b) Schematic picture of a rotating stripeless droplet. Adapted from Fig. 5 in [70].

3.7.1 Target droplet

We consider the balance between the temperature-gradient-induced (TGI) torque and the dissipative torque exerted on each droplet. In the target droplet, the helical axis is parallel to the temperature gradient. In this geometry, no hydrodynamic flow can be induced by the temperature gradient according to the ELT [10], which is consistent with the experimental result in [62]. Hence, we only need to consider the dynamics of n. Moreover, since the target droplets were observed under the weak surface anchoring condition (planar and sliding anchoring condition [59]), we consider that the surface torque on n due to the anchoring is negligible. Under these conditions, as we showed in 2.1.5, the dynamics of n in the steady state is simply given by [10]

$$\gamma_1 \frac{\partial n}{\partial t} = \nu n \times G e_z, \tag{3.1}$$

where γ_1, ν are the rotational viscosity and the Lehmann coefficient, respectively. The left-hand side of Eq. (3.1) is the dissipative term and the other side is the term derived from the thermo-mechanical coupling due to the chirality of CLC. Note that ν vanishes in achiral LCs. Applying $n\times$ to both sides of Eq. (3.1) and integrating over the volume of a spherical droplet with diameter D, we obtain respectively the TGI torque $\Gamma_{\text{target}}^{\text{TGI}}$ and the dissipative torque $\Gamma_{\text{target}}^{\text{diss}}$ exerted on the whole target droplet:

$$\begin{aligned} \Gamma_{\text{target}}^{\text{TGI}} &= \int_{\text{droplet}} \nu n \times (n \times G e_z) \, \text{dV} \\ &= -\nu_0 D^3 G e_z, \end{aligned} \tag{3.2}$$

$$\begin{aligned} \Gamma_{\text{target}}^{\text{diss}} &= \int_{\text{droplet}} \left(-\gamma_1 n \times \frac{\partial n}{\partial t} \right) \text{dV} \\ &= -\gamma_0 D^3 \omega e_z, \end{aligned} \tag{3.3}$$

where we introduced $\nu_0 = (\pi/6)\nu$ and $\gamma_0 = (\pi/6)\gamma_1$ for simplicity. The minus sign in Eq. (3.3) appears because the left-hand side of Eq. (3.3) is dissipative term. Since the sum of these two torques vanishes, we obtain the relation

$$-\frac{\omega}{G} = \frac{\nu_0}{\gamma_0} = \frac{\nu}{\gamma_1}. \tag{3.4}$$

Equation (3.4) indicates that the normalized rotational velocity $-\omega/G$ is constant and independent on the size of the droplets. This is confirmed in our experimental data for the target droplet as shown in Fig. 3.16. The fit yields $\nu_0/\gamma_0 = \nu/\gamma_1 = 7.0 \cdot 10^{-5}$ m/K $\cdot$ s.

3.7.2 Striped droplet

We next analyzed the striped droplet. As discussed in [62], the TGI torque is possibly cancelled by the elastic torque in the bulk of the droplet so that the striped droplet
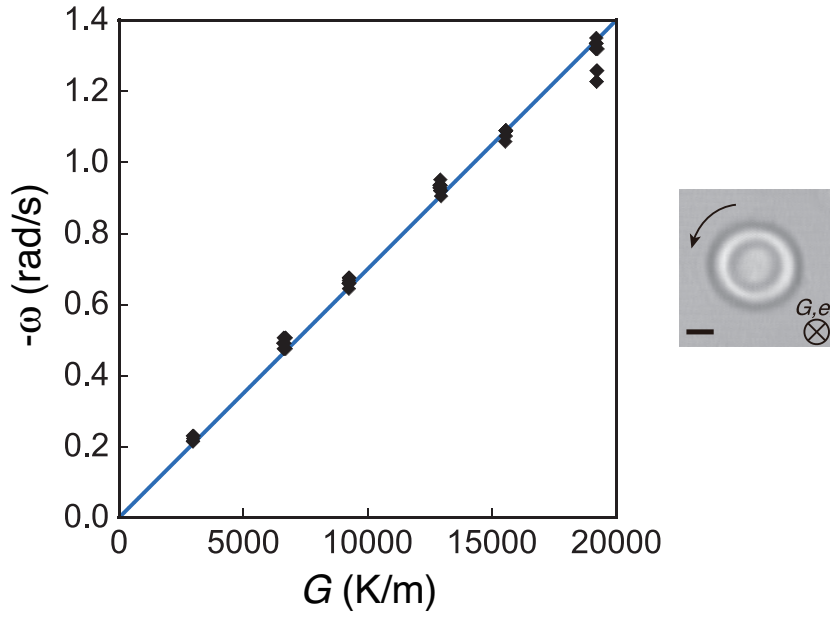
Figure 3.16: Rotational velocity $-\omega$ vs. temperature gradient G of the target droplet. The several points on the same temperature gradient correspond to the data for the droplets with different diameter. The solid blue line fits to the experimental data with Eq. (3.4). The figure is adapted from Fig. 6 in [70].
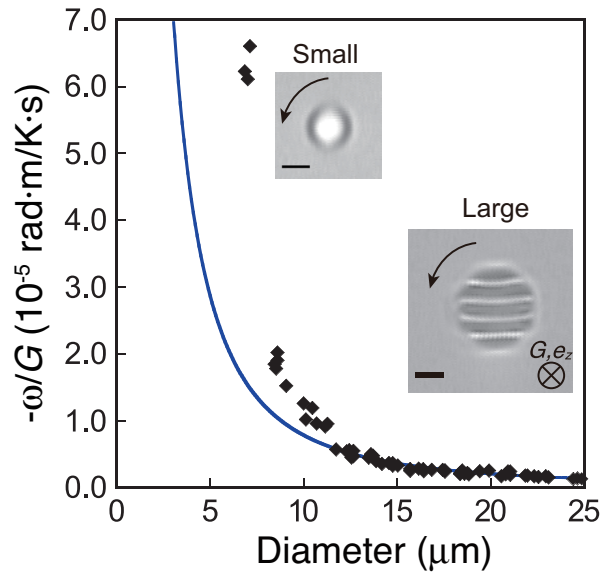
Figure 3.17: Rotational behavior of the striped droplet. The solid blue curve is a fit to the experimental data by Eq. (3.8). In the main text, we discuss the deviation between the theoretical curve and the experimental data. The figure is adapted from Fig. 7 in [70].

rotates like a rigid body. Therefore, we deduce that the TGI torque takes place only at the interface between the isotropic and cholesteric phase. Introducing the coefficient v_0^{surf} for the surface torque, the torque is given by

$$\Gamma_{\text{striped}}^{\text{TGI}} = -v_0^{\text{surf}} D^2 G \boldsymbol{e}_z. \tag{3.5}$$

In contrast to $\Gamma_{\text{striped}}^{\text{TGI}}$, the meanings of the dissipative torques are more unambiguous. We considered two kinds of the dissipative torques. First, since the striped droplet rotates in the viscous fluid as a rigid sphere, it is subjected to the dissipative torque in the following form [72]:

$$\Gamma_{\text{striped}}^{\text{diss,Iso}} = -\eta_0^{\text{Iso}} D^3 \omega \boldsymbol{e}_z. \tag{3.6}$$

Here we introduced the effective viscous coefficient η_0^{Iso} which is dependent on the viscosity of the surrounding isotropic phase. We next considered the frictional torque between the rotating droplet and the glass. Considering that the contact angle of droplets is uniquely determined by the surface tension following the Young equation [73], the diameter of the contact area should be proportional to that of the droplet. Therefore, introducing the effective friction coefficient η_0^{glass} between the droplet and the glass surface, the frictional torque is given by[1]:

$$\Gamma_{\text{striped}}^{\text{diss,glass}} = -\eta_0^{\text{glass}} D^4 \omega \boldsymbol{e}_z. \tag{3.7}$$

For the steady rotation, the sum of the torques in eqs. (3.5)-(3.7) vanishes, and hence one can obtain the relation between the rotational velocity and diameter as

$$-\frac{\omega}{G} = \frac{v_0^{\text{surf}} D^2}{\eta_0^{\text{glass}} D^4 + \eta_0^{\text{Iso}} D^3}. \tag{3.8}$$

Figure 3.17 shows the result of a fitting of the experimental data for the striped droplet with Eq. (3.8), which yields $v_0^{\text{surf}}/\eta_0^{\text{glass}} = 8.6 \cdot 10^{-16}$ m^3/K $\cdot$ s and $\eta_0^{\text{Iso}}/\eta_0^{\text{glass}} = 1.0 \cdot 10^{-6}$ m. The theoretical curve fits better with the larger droplets, while it clearly deviates in the region of small diameter D. In fact, we observed deformation of the striped pattern when the diameter is small as shown in the inset of Fig. 3.17. We consider that this deformation is one reason for the deviation.

3.7.3   Stripeless droplet

In the following, we extend the phenomenological equations (3.4) and (3.8) to describe the rotational behavior of the stripeless droplet. The helical axis of the stripeless droplets tilts with an intermediate angle ϕ between 0 and $\pi/2$. Therefore, both the torques exerted on the target droplet and those on the striped droplet should contribute to the stripeless

---

[1]Denoting the radius of the contact area and friction coefficient respectively as $R_c (\propto D)$ and η_c, D^4 in eq. (3.7) is derived by the integration $\Gamma_{\text{striped}}^{\text{diss,glass}} = \int_0^{R_c} (\eta_c r \omega) \cdot r \cdot 2\pi r \, dr \propto R_c^4 \propto D^4$.

droplet. Introducing a weight function of ϕ to each term in eqs. (3.4) and (3.8), we obtain the following extended equation for the stripeless droplet,

$$-\frac{\omega}{G} = \frac{v_0 v(\phi)D^3 + v_0^{\text{surf}} v^{\text{surf}}(\phi)D^2}{\gamma_0 \gamma(\phi)D^3 + \eta_0^{\text{glass}} \eta^{\text{glass}}(\phi)D^4 + \eta_0^{\text{Iso}} \eta^{\text{Iso}}(\phi)D^3}. \tag{3.9}$$

Here, Eq. (3.9) needs to converge to eqs. (3.4) and (3.8) respectively in the limit of $\phi = 0$ and $\pi/2$. Furthermore, taking into consideration that the weight functions should be invariant with respect to the conversion $\phi \leftrightarrow -\phi$ and $\phi \leftrightarrow \pi - \phi$, we approximate the weight functions as follows:

$$v(\phi) = \gamma(\phi) = \cos^2 \phi,$$
$$v^{\text{surf}}(\phi) = \eta^{\text{glass}}(\phi) = \eta^{\text{Iso}}(\phi) = \sin^2 \phi. \tag{3.10}$$

However, it turns out that Eq. (3.9), whenever ϕ is constant, cannot explain the rotational behavior of the stripeless droplet in Fig. 3.9, since Eq. (3.9) indicates that $-\omega/G$ is a non-increasing function of D. Given this result, we next focused on the possibility that ϕ is dependent on D and investigated the relation using FCPM. We measured ϕ from the FCPM cross-sectional images of rotating stripeless droplets (Fig. 3.13(c) dashed arrow). The result for different D is shown in the inset of Fig. 3.18. We find that ϕ is a decreasing function of D, $\phi(D) = 10.4 \cdot (D/[\mu\text{m}])^{-1.2}$ (a power-law fit, solid red curve in the inset of Fig. 3.18). Substituting Eq. (3.10) and this functional form of $\phi(D)$ into Eq. (3.9), the rotational behavior of the stripeless droplet fits well to Eq. (3.9) as shown in Fig. 3.18. The fit yielded $\eta_0^{\text{Iso}}/\gamma_0 = 0.6$. Note that, for the other parameters, we used the fitting parameters obtained in Figs. 3.16 and 3.17. We found that the rotational behavior of stripeless droplet is caused by the decreasing tilt angle with respect to the diameter, and that Eq. (3.9) explains the rotational behaviors of all the three types of CLC droplets at least at the level of the phenomenology described here.

3.8   Conclusion and remarks

We studied the Lehmann effect of CLC droplets focusing on the effect of the angle between the helical axis of the CLC droplet and temperature gradient. Using FCPM, we revealed that the different anchoring conditions enabled the observation of the three types of rotating droplets with the different tilt angle ϕ. Although Yoshioka et al. had already used FCPM to determine the surface structure of the striped droplets (Fig. 2.9), we reported here the structures of the target and the stripeless droplets for the first time. Then, the phenomenological equation (3.9) was proposed to explain the different rotational velocities of the droplets shown in Fig. 3.9. While Eq. (3.9) was consistent with the experimental data, we assumed the surface torque $\Gamma_{\text{striped}}^{\text{TGI}}$ in Eq. (3.5), whose origin is unrevealed for the moment.

To understand this surface torque which is necessary to interpret our experimental results, it is necessary to consider the boundary condition of the droplets more in detail.
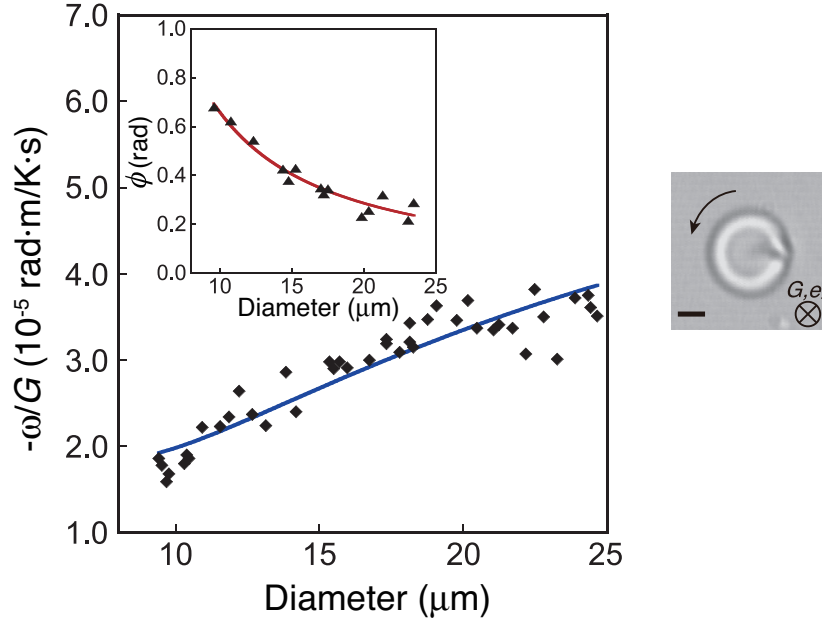
Figure 3.18: Rotational behavior of the stripeless droplet. The solid blue curve is a fit to the experimental data with Eq. (3.9). Inset: dependence of tilt angle ϕ on diameter D for the stripeless droplet. The solid red curve is a power-law fit to the experimental data. The left figure is adapted from Fig. 8 in [70].

The surface tension of the droplet possibly plays an important role for the Lehmann effect as well as for the Marangoni effect. However, the interface between the isotropic and cholesteric phase has been studied only in few papers [74, 75], and hence has not been understood sufficiently even for the equilibrium. Therefore, we have to investigate the surface effect carefully by means of both experiments and theory. Moreover, the deformed n field was reported to cause some additional thermo-mechanical effects [76, 77, 78]. Since the distortions of the striped patterns were observed in our homeotropic cells (Fig. 3.13(c)(d)), it would be important to explore the effect of the deformation on the rotational behaviors by improving the resolution of FCPM. Also, after our results were reported, Oswald et al. recently experimentally suggested, using the photobleaching method, that the hydrodynamic field does not exist even in the rotating striped droplet [79], which is incompatible with the report by Yoshioka et al. [62]. Actually, Oswald et al. followed bleached spots slightly outside the striped droplets, while Yoshioka et al. bleached inside the droplets. We find that it remains to establish the best method of measurement of hydrodynamic field.

Our approach to change the geometry of the droplets by anchoring conditions and the structural information of the droplets revealed by FCPM will lead to further understanding of the Lehmann effect, which is certainly a prominent non-equilibrium phenomenon we have to solve to understand the non-equilibrium dynamics of CLC.

3.9   Appendix A: Calculation of temperature gradient G

We derive an equation used to calculate the temperature gradient G. T_t and T_b denote the temperature of circulating water in the top and bottom temperature controlling chambers. T_2 and T_1 denote the temperature of top and bottom parts of LC. Also, the thermal conductivity of glass and LC were denoted by κ_g and κ_{LC}, respectively. The thickness of a glass and the LC layer are e and d, respectively. We define the temperature difference ΔT between waters at the top and the bottom, ΔT_{LC} between the top and bottom parts of LC and ΔT_{glass} induced in the glasses as a whole, as follows:

$$\Delta T = T_t - T_b, \tag{3.11}$$

$$\Delta T_{LC} = T_2 - T_1, \tag{3.12}$$

$$\Delta T_{glass} = \Delta T - \Delta T_{LC}. \tag{3.13}$$

Considering Fourier's law, which is $\boldsymbol{J_q} = -\kappa \operatorname{grad} T$,

$$\kappa_g \frac{\Delta T_{glass}}{4e} = \kappa_{LC} \frac{\Delta T_{LC}}{d}. \tag{3.14}$$

Consequently $G = \frac{\Delta T_{LC}}{d}$ is represented as follows:

$$G = \frac{\frac{\kappa_g}{\kappa_{LC}}}{1 + \frac{\kappa_g}{\kappa_{LC}} \cdot \frac{d}{4e}} \cdot \frac{\Delta T}{4e}. \tag{3.15}$$

3.10   Appendix B: Preparation of LC cell

3.10.1   Cleaning of glasses

┌─ Protocol ───

1. Ultrasonic cleaning in a neutral detergent (60min).

2. Ultrasonic cleaning in a diluted ($\times$10) neutral detergent (5 min $\times$ 3).

3. Ultrasonic cleaning in water (5 min $\times$ 3).

4. Ultrasonic cleaning in acetone (5 min $\times$ 3).

5. Ultrasonic cleaning in 2-propanol (5 min $\times$ 3).

6. Ultrasonic cleaning in water (5 min $\times$ 3).

7. Dry the substrate with nitrogen blower.

└───

3.10.2   Surface treatment of glass

┌─ Planar anchoring [59] ───

1. Prepare 2-butanone (Wako) solution of Epoxy hardener (5wt%, Structuralit 7).

2. Spin coat the solution (500rpm, 1 min), after filtering the solution with teflon filter (0.2 μm).

3. Anneal the substrate on the hotplate at 60°C for 1 hour.

└───

┌─ Homeotropic anchoring [71] ──

1. Immerse the glasses in the aqueous solution of Octadecyldimethyl(3-trimethoxysilylpropyl) ammonium chloride (0.5%, DMOAP, Fluorochem Ltd, see Fig. 3.19 and 3.20) for 20 min.

2. After linsing the substrate several times with $\sim$ 1 mL of water using a Pasteur pipette, dry the substrate using nitrogen blower.

3. Anneal the substrate on the hotplate at 110°C for 1 hour.

└───

3.10.3   Assembly of LC cells

We sandwiched a PET film spacer (25 μm) between two surface treated glasses (Fig. 3.21). The edges of the cell except the entrance were glued.

3.10.4   Encapsulation of LC

We encapsulated LC in the cell using capillary force in a vacuum chamber, while the LC was heated to reduce the viscosity of the LC. Finally, the cell was encapsulated completely using a glue.
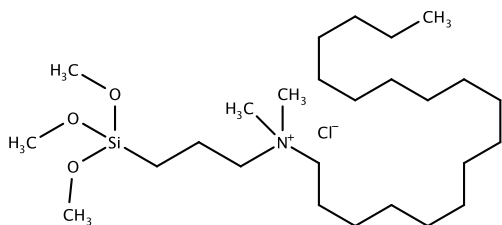
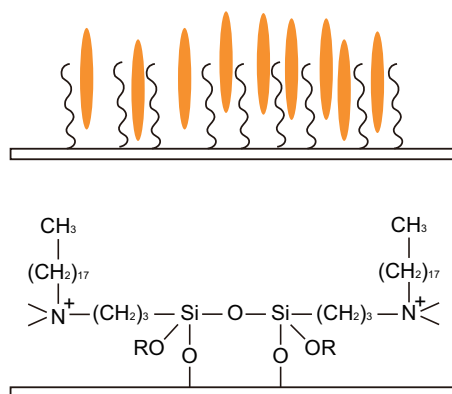Figure 3.19: Chemical structure of DMOAP (homeotropic anchoring).
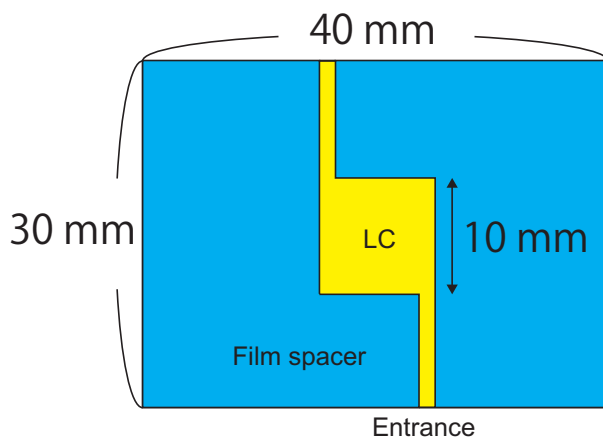
Figure 3.20: Homeotropic anchoring.

Figure 3.21: Structure of a LC cell.

Chapter 4

Experiment on helical self-propulsion of cholesteric liquid crystal droplets

In this chapter, we report our experimental discovery and investigation on the spontaneous helical motion of CLC droplets in a surfactant solution.

4.1   Introduction

The role of chirality in microswimmers has been receiving increasing attention in the field of biological physics [80, 27, 81, 82, 83]. Owing to the biomolecular chirality, chiral motions are remarkable in biological microswimmers; for instance, a sperm of a sea urchin controls its flagellum to steer in circular and helical paths [29, 28, 84]. Recently, to study the microswimmers' dynamics without difficulties in controlling biological systems, experimental setups of artificial swimmers have been established and their dynamics have been intensively investigated [31, 49]. As we introduced in Fig. 1.9, Kümmel et al. experimentally observed the circular motion of a chiral artificial swimmer in two dimensions (2D) using an L-shaped self-propelled particle [46]. However, there have been no studies reporting a chirality-induced helical motion of an artificial swimmer in 3D yet.

In this chapter, we present the first experimental realization of a chiral artificial microswimmer exhibiting the helical motion. We focused on self-propulsions of droplets in/on fluid [85, 86, 87], such as a moving alcohol droplet on water [88]. The underlying mechanism of the self-propulsion is the Marangoni flow induced by the gradient of the surface tension at the liquid-liquid interface [89]. Recently, Herminghaus et al. reported nematic liquid crystal (NLC) droplets can also swim in a surfactant solution [48, 90].

Meanwhile, as we investigated in Chapter 3, a cholesteric liquid crystal (CLC), which shows a helical director field due to the chirality of molecules, undergoes rotational motion when subjected to external fields such as a temperature gradient [19, 62, 21, 70]. This rotational motion is explained as a result of the coupling between

axial (rotational motion) and polar (external field) vectorial quantities only allowed in chiral systems [11]. Hence, a CLC droplet in a surfactant solution can swim in a chiral path owing to the chiral coupling between the Marangoni flow and rotational motion.

4.2 Marangoni-effect-driven self-propelled LC droplet

Here, we overview the Marangoni-effect-driven self-propelled LC droplets.

4.2.1 Marangoni effect

The Marangoni effect is known as a fluid flow induced by a surface tension gradient at interfaces between fluid/fluid or fluid/gas [91, 92]. A phenomenon called " tears of wine" is a well known example of phenomena induced by the Marangoni effect, which is still not fully understood and attracting interests [93, 94, 95, 96, 97]. After wine is poured into a wine glass, a droplet of wine climbs up at the meniscus from the bulk. One of the mechanisms, which is generally accepted, is depicted in Fig. 4.1. First, ethanol evaporates at the surface of wine. However, the supply rate of ethanol due to diffusion from the bulk is different between the periphery and above the bulk. At the meniscus, the supply rate is lower than that above the bulk, since the liquid film at meniscus has a larger surface area in relation to the small volume. Hence, concentration gradient of ethanol is lower at the periphery. The concentration gradient leads to the gradient of surface tension, where the surface tension is higher at the periphery. Finally, wine is dragged upwards at the periphery.
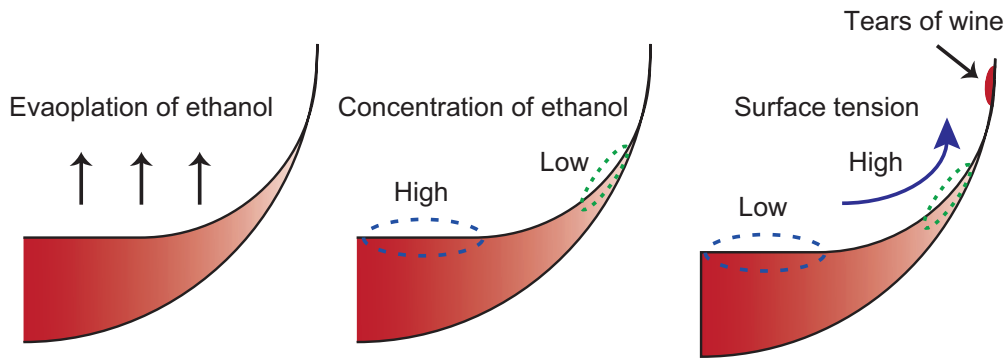

Figure 4.1: Tears of wine, which is an example of phenomena induced by the Marangoni effect.

In hydrodynamic equation, we have following boundary conditions at the interface

between two fluids [12, 89],

$$\sigma_{ij} = -P\delta_{ij} + \eta\left(\frac{\partial v_i}{\partial x_j} + \frac{\partial v_j}{\partial x_i}\right), \qquad (4.1)$$

$$(\boldsymbol{\sigma}^1 - \boldsymbol{\sigma}^2)\boldsymbol{n} = \left(\frac{1}{R_1} + \frac{1}{R_2}\right)\gamma\boldsymbol{n} \qquad \text{at the interface,} \qquad (4.2)$$

$$\nabla_s\gamma = \boldsymbol{P}_s(\boldsymbol{\sigma}^1 - \boldsymbol{\sigma}^2)\boldsymbol{n} \qquad \text{at the interface,} \qquad (4.3)$$

where $\boldsymbol{\sigma} = \sigma_{ij}$ is the stress tensor, γ is surface tension, R_1 and R_2 are the principal radii of curvature, $\boldsymbol{n}$ denotes surface normal, and $\boldsymbol{P}_s = 1 - \boldsymbol{nn}$ is the surface projector, $\nabla_s = \boldsymbol{P}_s\nabla$ is the surface gradient (Fig. 4.2). The subscripts denote the index of two fluids. According to Eq. (4.3), if a surface tension gradient exists, we have a jump of viscous stress in the tangential direction of the surface at the interface between two fluids. The surface tension γ is generally a function of chemical concentration, temperature, etc. Thus, concentration gradient and temperature gradient, etc. induce the fluid flow.
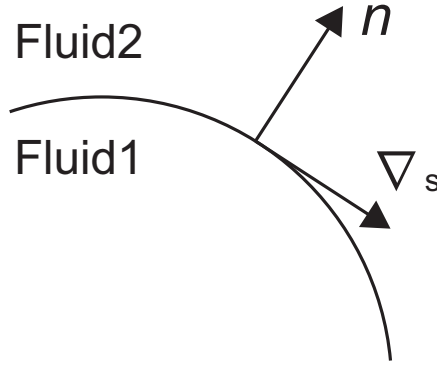
Figure 4.2: Gradient of surface tension at the fluid/fluid interface induces fluid flows.

4.2.2 Marangoni-effect-driven self-propelled NLC droplet proposed by Herminghaus et al.

Herminghaus et al. reported that the NLC droplets swim in a surfactant solution driven by the Marangoni effect [48]. Before this work, only isotropic fluid such as alcohol, water droplet had been used as the self-propelled droplet. Fig. 4.3 shows the experimental configuration where a NLC droplet which swims in a surfactant solution. As shown in Fig. 4.4 [48], the texture observed with crossed polarizers indicates that the droplet has a radial director field around the point defect and the surface anchoring of the droplet is homeotropic. Although the point defect locates at the center of the droplet in equilibrium, it deviated from the center toward the direction of the translational motion due to the Marangoni flow which occurs inside (Fig. 4.4). The observation is an evidence indicating the droplet moves due to the Marangoni effect.
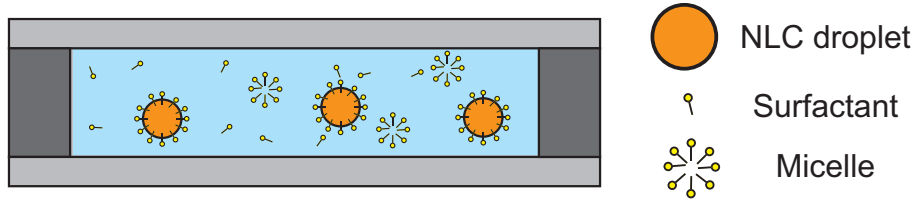
Figure 4.3: Experimental setup of the experiment on the NLC droplets swimming in a surfactant solution. The experimental system was proposed by Herminghaus et al. [48].
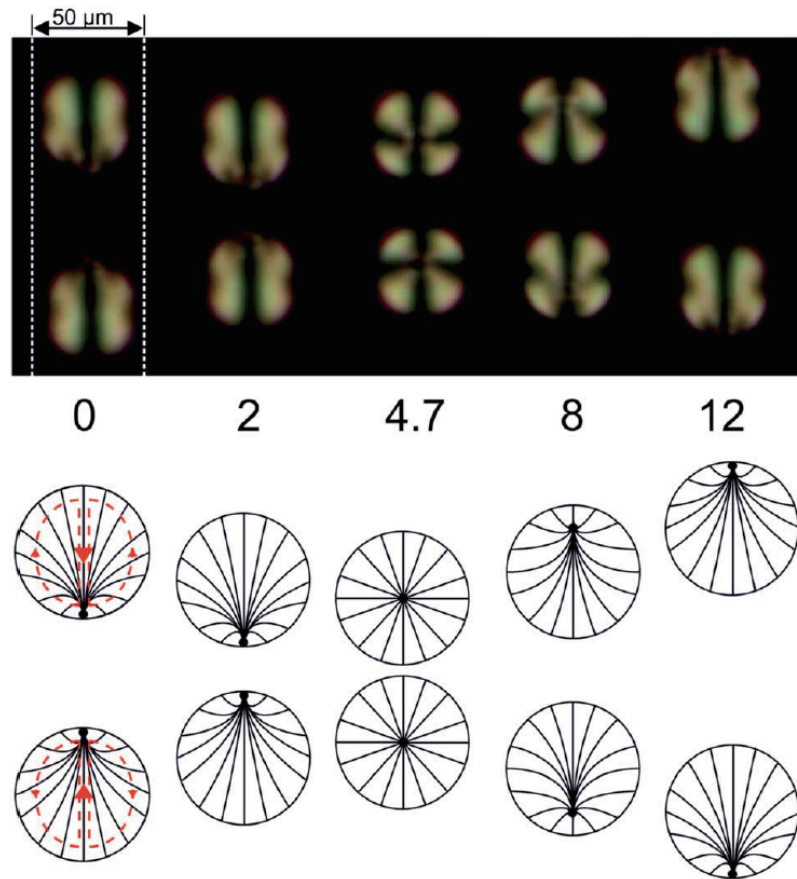
Figure 4.4: Swimming NLC droplets in surfactant solution observed with crossed polarizers [48]. The figure is adapted from Fig. 8 in [48] - Published by The Royal Society of Chemistry. The authors observed the collision dynamics of two NLC droplets confined in a microfluidic channel. The dashed lines in the image indicate the edges of the channel . In the bottom figures, they described the cross-sectional director field in the NLC droplets during the collision. In each figure, lines inside the droplet indicate the director field. They reported that the locations of point defects is displaced towards the direction of motion due to the Marangoni flow indicated by red dashed arrows.

Figure 4.5 shows what is happening when the droplet is swimming. To swim persistently, the surface tension should be lower at the front of the droplet. Hence, the surfactant concentration should be higher at the front. Since the homogeneous surfactant concentration distribution should be stable in equilibrium, emergence of such concentration gradient without any external field requires spontaneous symmetry breaking associated with some non-equilibrium process. Actually, in the case of swimming NLC droplet, *dissociation process of the NLC into the micelles in the surfactant solution* is considered to be the origin of the symmetry breaking and persistent swimming [48]. The detailed mechanism in the molecular level has not been revealed yet, and it still requires further experimental and theoretical investigations.
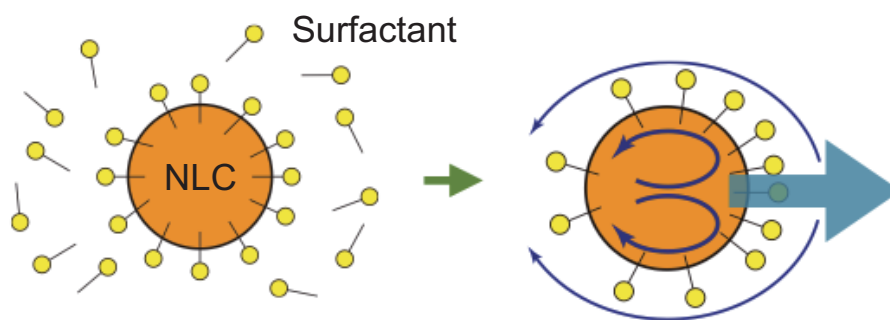
Figure 4.5: Surfactant concentration distribution on a swimming NLC droplet.

4.3 Material and method

4.3.1 Materials

In our experiments, a mixture of the NLC (4-cyano-4'-pentylbiphenyl, TCI) and 2wt% of a chiral dopant (R811, WuXi AppTec Co., Ltd), which works as a CLC, was dispersed in an aqueous surfactant solution (13wt%, tetradecyltrimethylammonium bromide [48], Wako) as described below. To eliminate the effect of the buoyancy on the swimming behavior of the CLC droplets, we adjusted the density of surfactant solutions using a mixture of D_2O and H_2O as a solvent [90]. We measured the density of surfactant solutions with different compositions of D_2O/H_2O using density meter (DMA4500, Anton Paar, accuracy: $5.0 \cdot 10^{-5}$ g/cm^3, see Appendix A). In our experiments, we used D_2O/H_2O with 25wt% D_2O, whose density (1.02233 g/cm^3) is well matched with that of CLC (1.02175 g/cm^3).

4.3.2 Production of droplets

As shown in Fig. 4.6, after pipetting a surfactant solution into a chamber made of a cover glass and a double-sided tape with a hole (diameter: $3 \sim 4$ mm, thickness: ~ 750 μm,

see Fig. 4.7), CLC droplets were injected into the solution using a microinjector (Femtojet, Eppendorf) with commercially available needles (Femtotips). Then, the chamber was encapsulated with an upper cover glass. The timelapse images of injection process are shown in Fig. 4.8. To investigate the 3D dynamics of the CLC droplets, we used spacers much thicker than the diameter $D \approx 20~\mu$m of CLC droplets we observed. The sizes of the CLC droplets were adjusted by controlling the injection pressure p_i and injection time t_i of Femtojet. While the appropriate parameters are different for each needle, Femtojet enables us to produce microdroplets with a submicron precision. Although the microfluidics has been developed for the production of microdroplets [98], it still requires special facilities and technique. In contrast, our new approach with Femtojet is so simple in addition to its high precision that it should become a powerful tool for the production of microdroplets.
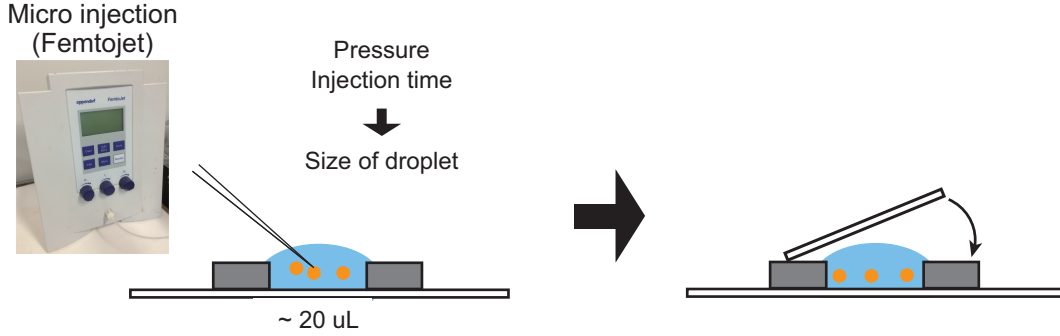
Figure 4.6: Preparation of a sample. We encapsulated the cell with a upper cover glass after the injection of droplets.

4.3.3 Microscopy

The dynamics of CLC droplets in the surfactant solution were observed with an inverted optical microscope without any polarizers unless otherwise noted (DMI6000B, Leica). The time-lapse images were acquired using a camera (HXG40, Baumer, 10 frames/sec). While we were manually focusing on each swimming CLC droplet during the acquisition, XY coordinates of the XY stage (TANGO Desktop, Märzhäuser Wetzlar, precision: $\sim 1~\mu$m) and Z coordinate of the motorized Z drive (Precision: $\Delta z = 0.7~\mu$m) of objective lens ($\times 4$ or $\times 20$, Leica) were recorded through Labview programming. Then, we reconstructed the 3D trajectory of the droplet from the recorded XYZ coordinates and the position of the center of mass of the droplet in each image. Here, after the images were binarized, we detected the center of mass of the droplet (Appendix B). We conducted our experiments at 25°C.
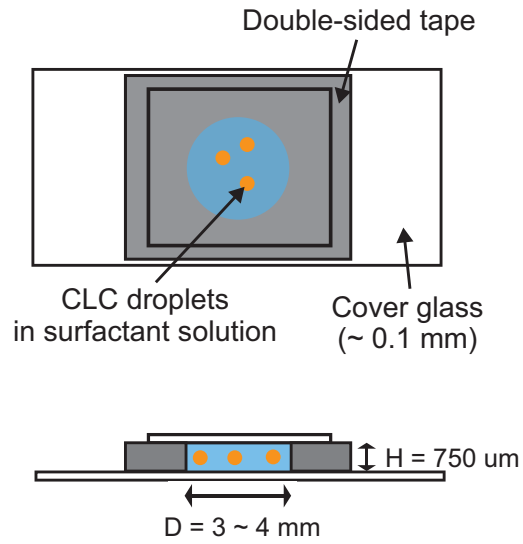
Figure 4.7: Chamber for the observation of 3D dynamics of CLC droplets.
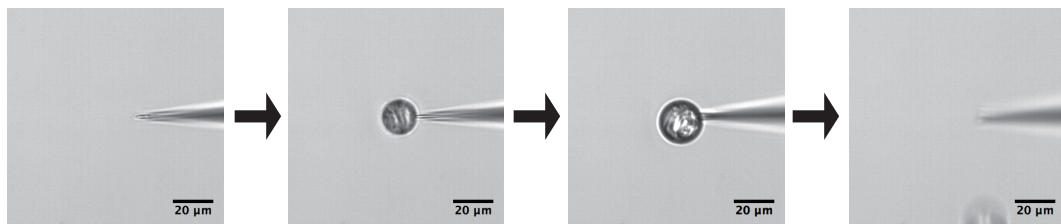
Figure 4.8: Injection of a droplet. Commercially available "Femtotip" was used as a needle for the injection (P = 1950 hpa, T_i = 1 s, D = 20.4 μm). The scale bar is 20 μm.

4.4   Wide-view observation of swimming CLC droplets

Figure 4.9 shows the 2D projected trajectories of CLC droplets (initial diameter: $D_0 = 19.3 \sim 20.2\ \mu$m) observed through the low power of the microscope ($\times 4$) by fixing the position of XY stage and Z drive. The focal plane of the objective lens was set at the upper cover glass. We injected the droplets ($N = 7$) sequentially within 30 s. The trajectories ~ 2 min after the injection of the first droplet were drawn in Fig. 4.9. The centers of mass of the droplets were tracked until the droplets stop swimming or escape outside the field of view. As a result, we observed zig-zag motions in 2D images for all the droplets which did not escape outside.

4.5   3D tracking of a swimming CLC droplet

4.5.1   3D trajectory of a CLC droplet

Figures 4.10(a) and (b) show the 2D and 3D trajectories of a single CLC droplet. Here, we manually focused on the swimming CLC droplet through the high power of the microscope ($\times 20$, depth of focal: $\sim 1.4\ \mu$m) during the observation. We injected 3 droplets ($D_0 = 20.2 \sim 20.6\ \mu$m) within 20 s and tracked one of them. Since our droplet swam due to the Marangoni flow induced by the dissolution of LC into surfactant solution [48], the size of the droplet decreased during the locomotion. Figure 4.11 (a) shows the time evolution of diameter of the droplet, where the origin of time is set to the time when the first droplet was injected. We found that the diameter decreased linearly in time ($1.2\ \mu$m/min). Assuming the constant dissolution rate per unit area at the surface of the droplet, we can readily derive such linear damping of the diameter. If we define the volume, surface area of a droplet and the constant dissolution rate per unit area as $V(t), S(t)$ and k, the time evolution equation for $V(t)$ is given by,

$$\dot{V}(t) = -kS(t). \tag{4.4}$$

Using the relations $V(t) = (\pi/6)D(t)^3$ and $S(t) = 4\pi(D(t)/2)^2$ where $D(t)$ is the diameter of the droplet, we obtain,

$$D(t) = D_0 - 2kt, \tag{4.5}$$

where D_0 is the initial diameter. In Fig. 4.11 (a), k is calculated as $\sim 0.6\ \mu$m/min.

Also, the time evolution of z-coordinate, absolute value and xyz components of velocity of the droplet are shown in Fig. 4.11 (b)-(f). Here, we reduced noise in the recorded coordinates with the cutoff frequency $f_c = 0.5$ Hz before calculating the velocity. We noted that the droplets had a tendency to move upward at the beginning and frequently arrive at the upper glass during the locomotion as shown in Fig. 4.11(b), even though the effect of the buoyancy was carefully suppressed using D_2O. The bias would be due to the thermal convection which is notoriously inevitable in such thick cells as ours.
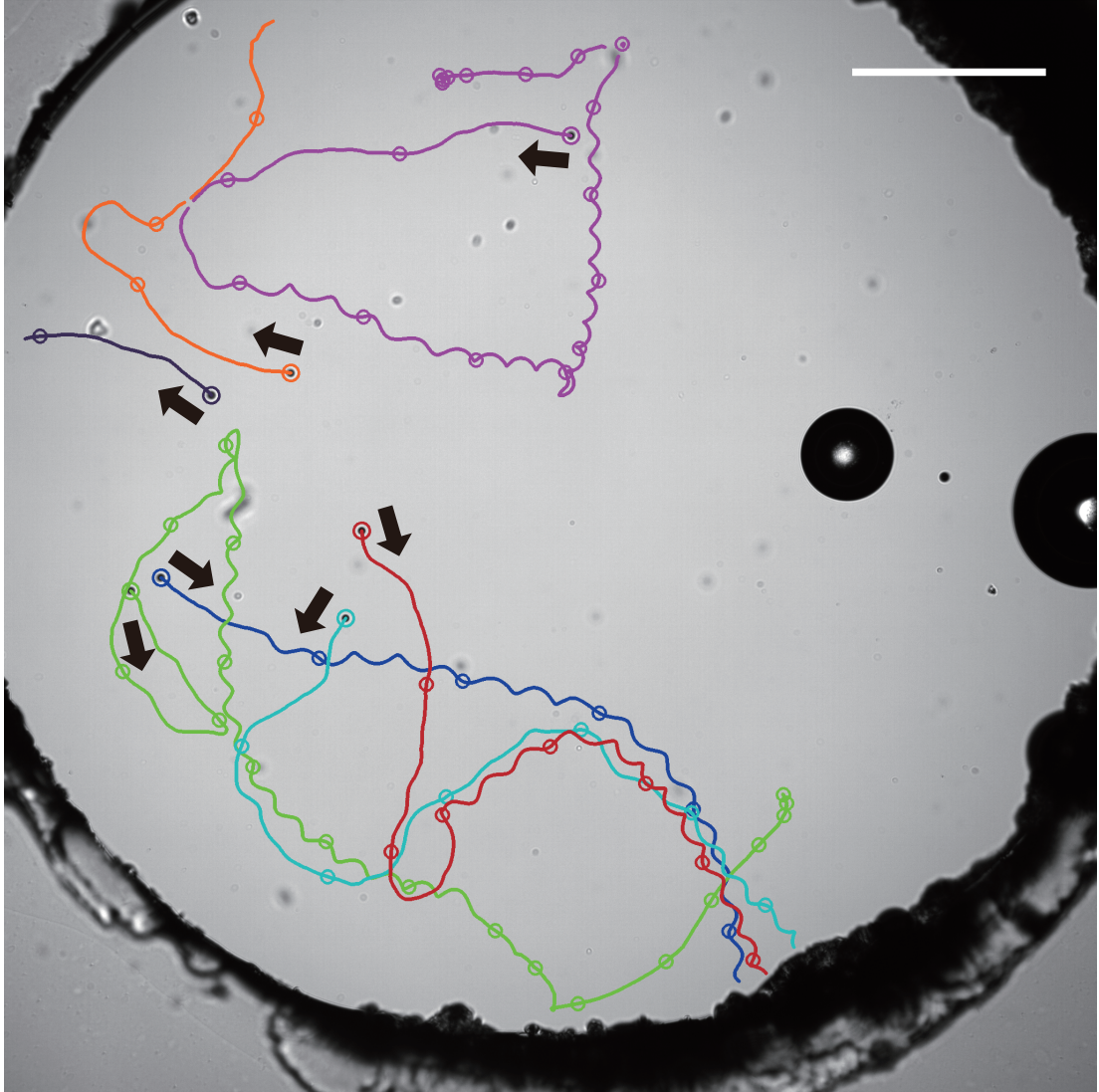
Figure 4.9: 2D projected trajectories of the CLC droplets injected during a short period (30 s). We drew the trajectories 2 min after the first droplet was injected. The droplets swam in the direction of arrows. The circles on the trajectories are drawn every 30 s. The large dark circles are air bubbles which entered the chamber during the encapsulation. The scale bar is 500 μm.
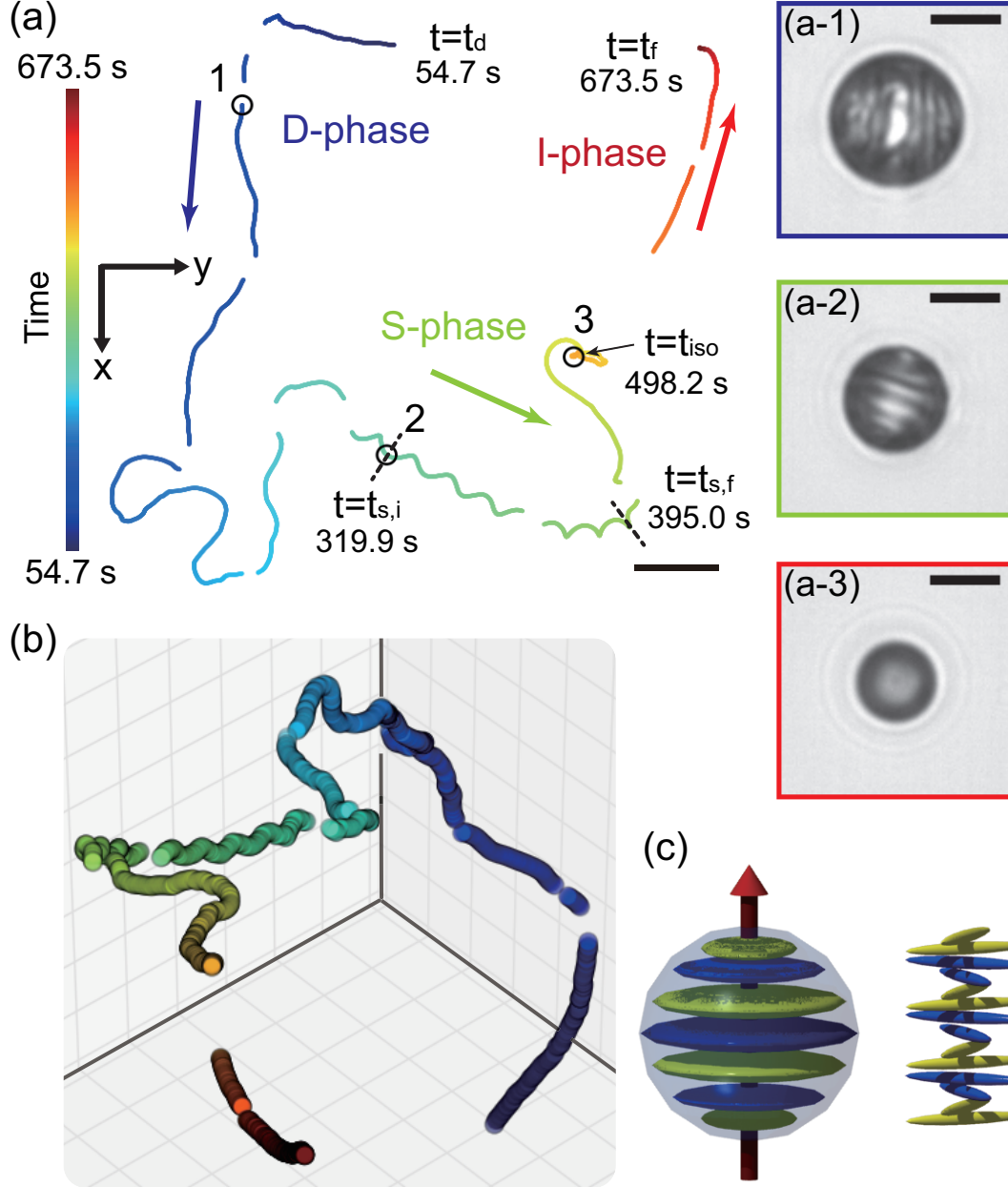
Figure 4.10: (a)(b) The 2D and 3D trajectories of a CLC droplet. The gradient of color and the arrows represent the time evolution. The gaps in the trajectory are due to the lack of data during moving the XY stage. (a-1)-(a-3) The textures of the droplets observed at the three points marked in (a), respectively. (c) Schematic image of a droplet with uniform helical director field, corresponding to (a-2). The red arrow indicates the helical axis of CLC. The scale bars are 200 μm in (a) and 10 μm in (b)(c), respectively.
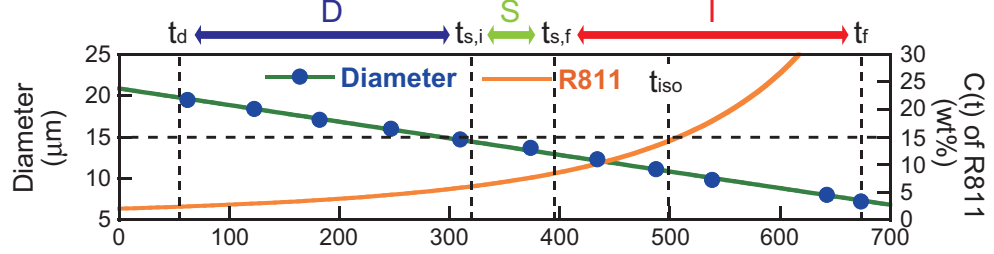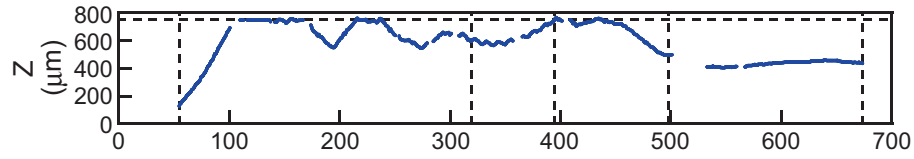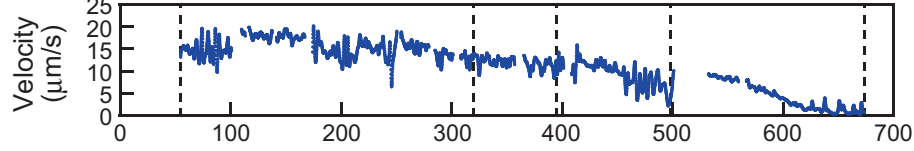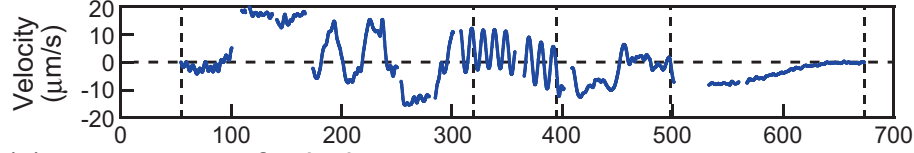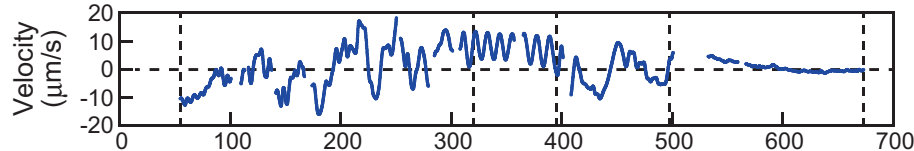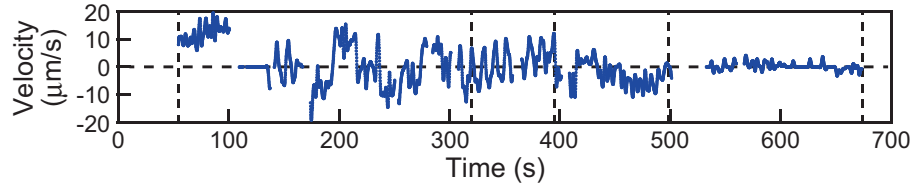
Figure 4.11: Time-evolution of (a) diameter and $c(t)$, (b) height (z coordinate), (c) absolute velocity, (d)(e)(f) xyz components of the velocity of the droplet corresponding to Fig. 4.10. The data in (a) is fitted with a green line. The vertical lines indicate $t = t_d, t_{s,i}, t_{s,f}, t_{iso}, t_f$, respectively. In (a), the orange curve indicates the concentration $c(t)$ of R811 inside the droplet calculated from the diameter. In (b), the z coordinate of the bottom glass is set to 0 μm. The horizontal dashed line in (b) indicates the height of the upper glass ($z = 755$ μm).

4.5.2   Texture and dynamics of a CLC droplet

In the single trajectory, the CLC droplet underwent three phases exhibiting different textures and motions.

In the first phase "D-phase (Defomation-phase)" from $t = t_d$ to $t = t_{s,i}$ (Fig. 4.10(a)), the droplet swam meandering with the deformed director field stirred by the Marangoni flow (Fig. 4.10(a-1)). As we will see later, when the director field is not stirred by the Marangoni flow, the CLC droplet does not exhibit such meandering behavior but rather deterministic behavior. Hence, the meandering behavior should be due to the complicated spatiotemporal modulation of the director field.

In the "S-phase (Striped-phase)" from $t = t_{s,i}$ to $t = t_{s,f}$, the droplet exhibited a striped pattern (Fig. 4.10(a-2)) which means the homogeneous helical director field as sketched in Fig. 4.10(c). Here, we defined $t_{s,i}$ and $t_{s,f}$, when we clearly observed a homogeneous striped pattern for the first and last times, respectively. In the S-phase, we observed a 2D zig-zag motion, which is a helical motion in 3D as we will show below.

In the final phase "I-phase (Isotropic-phase)" from $t = t_{s,f}$ to $t = t_f$, the striped pattern of the CLC droplet gradually deformed and then the droplet got isotropic completely at $t = t_{iso}$ (Fig. 4.10(a-3)). We defined t_{iso} when the deformation of the director field disappeared and the texture of the droplet got isotropic under the microscope without polarizers. During the period just after $t = t_{iso}$ in which the trajectory of the droplet is not shown in Fig. 4.10, we confirmed the isotropy of the CLC using crossed polarizers. The image observed using crossed polarizers is shown in Fig. 4.12. The ballistic motion of the isotropic CLC droplet observed after $t = t_{iso}$ is consistent with that of the isotropic NLC droplet [48].
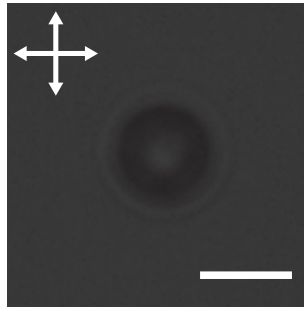
Figure 4.12: The image of the CLC droplet in I-phase observed with crossed polarizers. The image was captured at $t = 528.8$ s in the trajectory in Fig. 4.10(a), just after the image in Fig. 4.10(a-3) was captured. The white double-headed arrows show the directions of the polarizations of two polarizers. The scale bar is 10 μm.

4.6 Why do the 3 phases exist in a life of the CLC droplet?

Why do the 3 phases exist in a life of the CLC droplet? In this section, we interpret each transition from D-phase to S-phase, from S-phase to I-phase.

4.6.1 D-phase to S-phase

We consider that the transition from the D-phase to the S-phase is understood by the Ericksen number $Er = \eta v L / K$, a non-dimensional number defined by the ratio of the viscous to elastic force. Here, v, η, L, K are the characteristic velocity, viscosity, length and elastic constant of LC, respectively. Defining the Ericksen number for a CLC droplet, the characteristic velocity and length are the velocity v and the diameter D of a CLC droplet. In our experiments, the size and the velocity of the droplet decreased as shown in Fig. 4.11(a)(c). Therefore, assuming constant values for K and η, Er decreases as the CLC droplet shrinks. As a result, in the S-phase, the deformation of the director field due to the Marangoni flow is suppressed and the CLC droplet exhibits a homogeneous helical director field without deformation. Using the physical properties $\eta \sim 0.7\,\mathrm{Pa \cdot s}$ [99] and $K \sim 5 \cdot 10^{-12}$ N [23], which are the average values for 5CB, and typical experimental parameters $D \sim 20\,\mu\mathrm{m}, v \sim 15\,\mu\mathrm{m/s}$, we obtain Er ~ 0.5, which is consistent with our discussion above, since the effect of viscosity and that of elasticity balance when Er $= O(1)$.

4.6.2 S-phase to I-phase

Regarding the transition from the S-phase to the I-phase, the effect of increasing chirality during the locomotion should be important. We confirmed the insolubility of chiral dopant in the surfactant solution by putting a powder of R811 in the solution for 10 min. Due to the insolubility of R811, the concentration of R811 should increase as the droplet shrinks. Since the cholesteric-isotropic transition temperature T_{iso} decreases as the concentration of R811 increases as shown in Fig. 4.13, T_{iso} of the CLC droplet should decrease in the shrinking process. In Fig. 4.11(a), we estimated the concentration $c(t)$ of R811 in the CLC droplet. Here, we applied a relation $c(t) = c_0 D_0^3 / D(t)^3$, where c_0, D_0 and $D(t)$ denote the initial concentration of R811, the initial diameter and the diameter at time t, respectively. We calculated $c(t_{\mathrm{iso}}) = 14.2\mathrm{wt\%}$ using the linear fit to the experimental data of $D(t)$. Since $T_{\mathrm{iso}} = 25.0°\mathrm{C}$ when the concentration of R811 is 15wt%($\sim c(t_{\mathrm{iso}})$) (Fig. 4.13), we consider that the CLC droplet got isotropic because T_{iso} of the CLC droplet approached our experimental temperature 25°C.
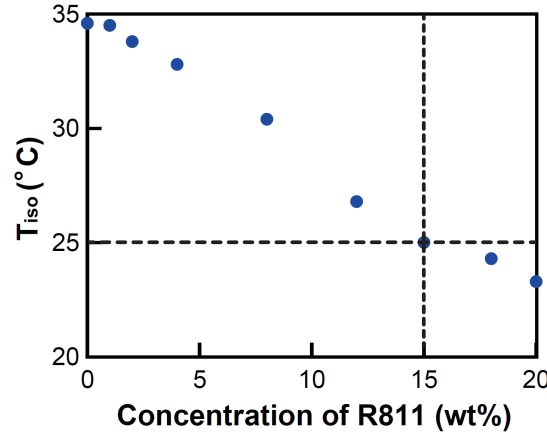
Figure 4.13: Isotropic transition temperature of CLC at various concentration of R811. The vertical and horizontal dashed lines indicate 15wt% and 25°C, respectively.

4.7   Helical motion in S-phase

Figures 4.14(a) and (b) show a part of the 2D and 3D trajectory during the S-phase in Fig. 4.10(a). The corresponding time-evolution of z coordinate of the CLC droplet is also shown in Fig. 4.14(c). We found that the CLC droplet with homogeneous helical director field swam in a left-handed helical path. Here, a helix is left-handed, if the rotational direction is anti-clockwise. Importantly, all the CLC droplets we tracked showed left-handed helical paths ($N = 4, D_0 = 20.0 \sim 20.8 \, \mu$m). The radius r, pitch P, period T, velocity v of the helical motion are shown in Table 4.1, respectively ($N = 4$). We calculated these parameters from the 2 periods of the helical motion when the diameters were $14.5 \sim 14.8 \, \mu$m.

Dopant	Handedness	r (μm)	P (μm)	T (s)	v (μm/s)
R811	Left-handed	14.5 ± 4.1	108.5 ± 10.6	10.7 ± 0.5	13.0 ± 2.0
S811	Right-handed	13.9 ± 2.7	108.2 ± 5.2	10.5 ± 0.3	12.7 ± 2.3

Table 4.1: The helix parameters of the helical motion of the CLC droplets doped with R811 and S811.

To confirm that the helicity of the helical path is determined by the chirality of CLC, we tracked the swimming CLC droplets doped with a chiral dopant S811 (2wt%), which is the enantiomer of R811. As shown in Fig. 4.15, the S811-doped droplets swam in right-handed helical paths ($N = 4, D_0 = 19.7 \sim 21.1 \, \mu$m), while the helix parameters were similar to those of the R811-doped droplets (Table 4.1).

In contrast, we observed only ballistic motion for NLC droplets (only 5CB) when the diameters are below $20 \, \mu$m. In Fig. 4.16(a), we show the 2D projected trajectories of the

(a)

319.9 s   Time   357.2 s

(b)

(c)
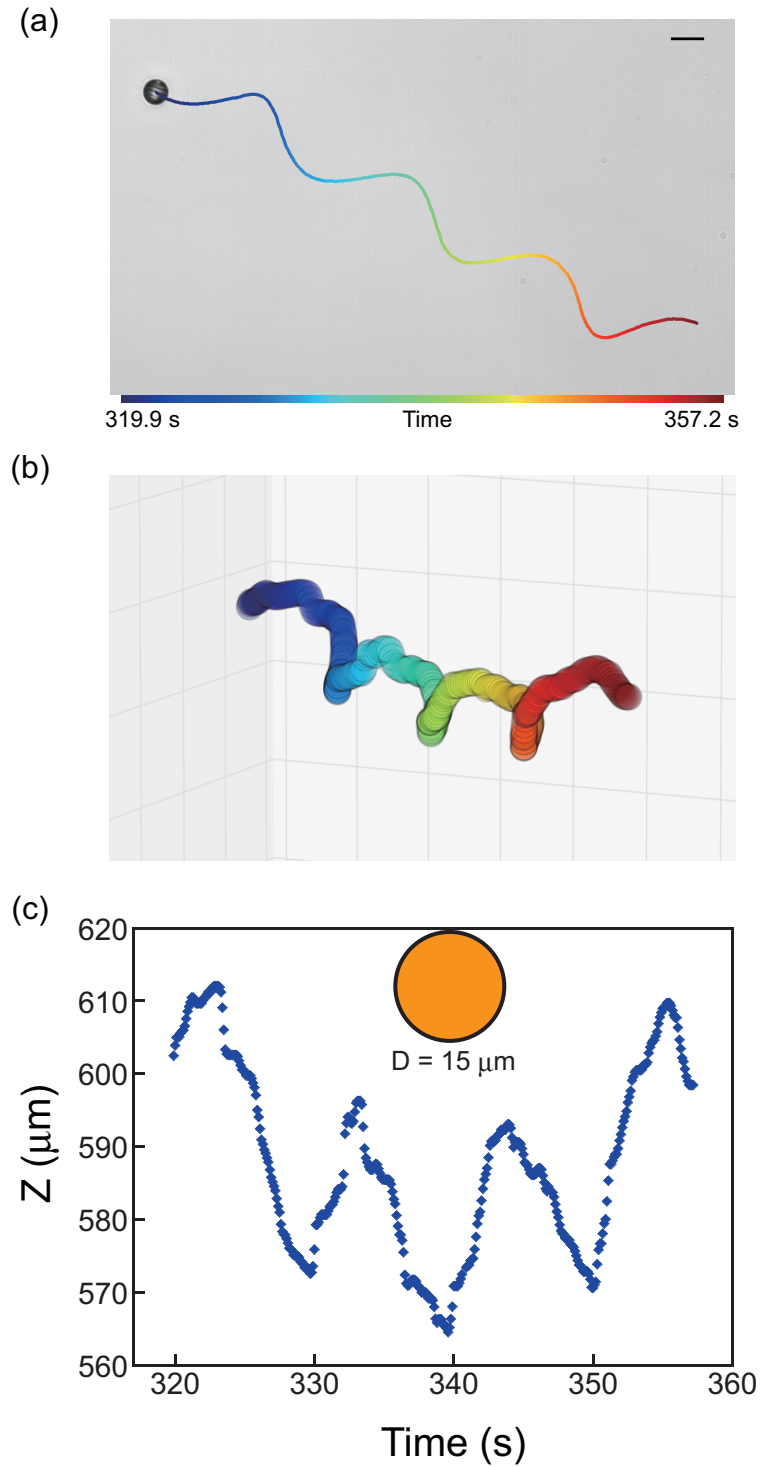
Figure 4.14: (a) 2D and (b) 3D trajectory of the R811-doped CLC droplet during the S-phase in Fig. 4.10. (c) Time evolution of the z coordinate of the droplet. The scale bar in (a) is $20\,\mu$m. An orange circle is depicted for the reference of the diameter $\sim 15\,\mu$m of the CLC droplet.
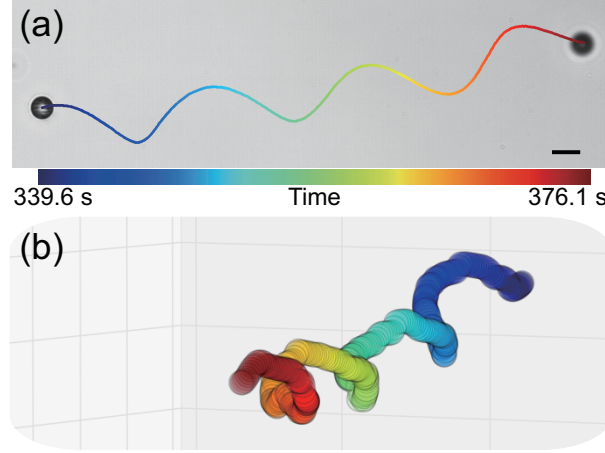
Figure 4.15: (a) 2D and (b) 3D trajectory of a S811-doped CLC droplet. The scale bar in (a) is 20 μm.

NLC droplets ($D_0 = 19.2 \sim 19.6 \, \mu$m). Note that the experimental conditions are same as those in the case of the CLC droplets. As previously reported [48, 90], we found that the radial director field of the NLC droplet was deformed due to the Marangoni flow inside the droplet, and the point defect in the droplet, which should be located at the center of the droplet in equilibrium, changed its position toward the direction of the translational motion of the droplet as shown in Fig. 4.16(b)-(d).

According to these results, we conclude that the helical motion of the CLC droplets is induced by the chirality of CLC. Note that Krüger et al. recently reported that the helical motions[1] of the NLC droplets appear when the diameter was $\sim 50 \, \mu$m much larger than that of our droplets [90]. Hence, we find that the NLC droplets show qualitatively different behaviors depending on the droplet size. It remains to elucidate the mechanism of the emergence of such property of the NLC droplets.

4.8 Direction of helical axis of a swimming CLC droplet

Furthermore, we found a notable feature that the helical axis of the droplet is always directed toward outside from the helical axis of the helical path as the arrows in Fig. 4.17(a). To represent this feature, we define $\theta_1 = \arccos\left(\dot{\boldsymbol{v}} \cdot \boldsymbol{a} / |\dot{\boldsymbol{v}}|\right)$ (See Fig. 4.17(b)). Here, the time derivative of velocity $\dot{\boldsymbol{v}}$ is perpendicular to the helical axis of a helical path (see also Fig. 5.12 in Chapter 5). Hence, when the helical axis $\boldsymbol{a}$ of the CLC droplet is directed outside as observed in Fig. 4.17(a), $\theta_1 > \pi/2$. The feature was robustly observed for all the droplets doped with either R811 or S811. Hence, we consider that the helical motion is correlated with the helical director field.

---

[1]In [90], left- and right-handed helical paths appear with equal probability, since the NLC is achiral.
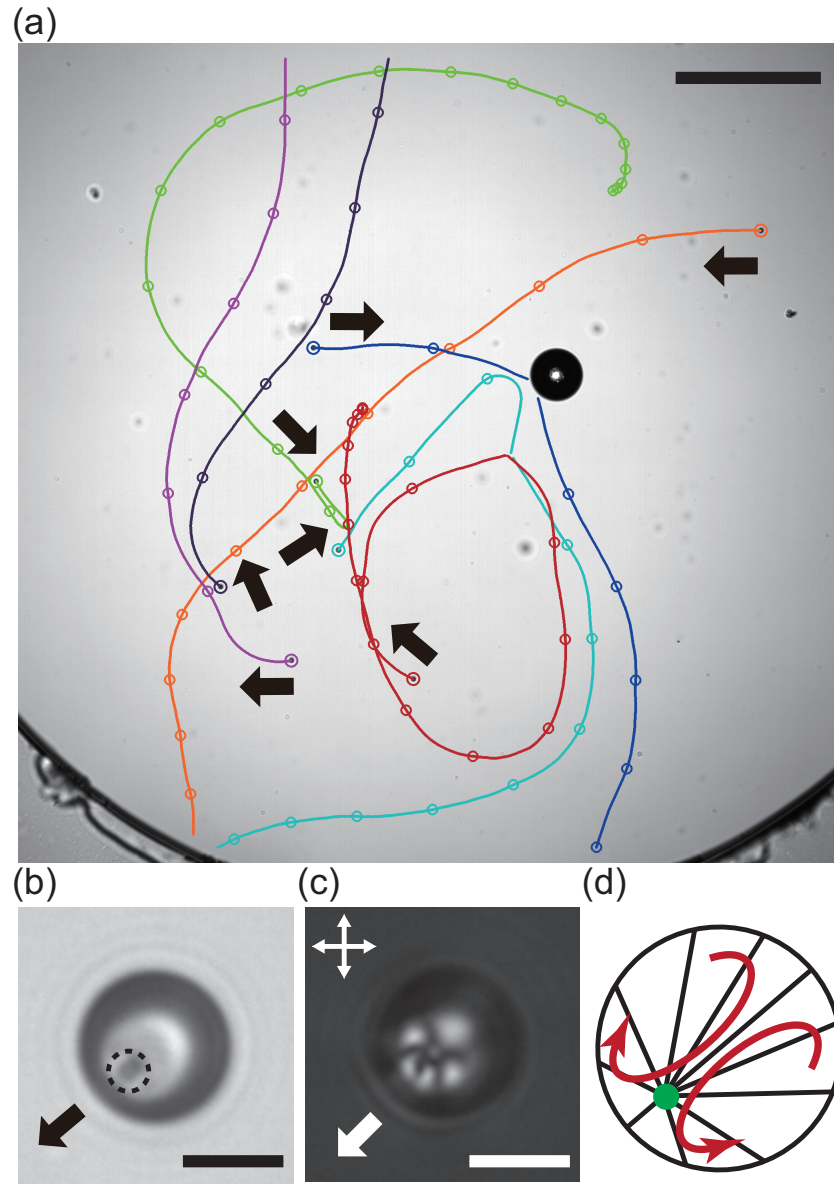
Figure 4.16: (a) 2D projected trajectories of the NLC droplets ($N = 7$, injected within 30 s) observed through the low power of microscope (×4). We drew the trajectories 3 min after the first droplet was injected. The droplets swam in the direction of arrows. The circles on the trajectories were drawn every 30 s. (b)(c) Texture of a NLC droplet during the swimming observed without and with polarizers (objective, ×20). The arrows represent the direction of motion. The dashed circle in (b) indicates the position of the point defect inside the droplet. Double-headed arrows in (c) indicate the direction of 2 crossed polarizers. (d) A schematic cross-sectional image of the director field inside the NLC droplet. The direction of the director field and the point defect are drawn as lines and a point, respectively. The red curved arrows represent the Marangoni flow. The scale bars are 500 μm in (a) and 10 μm in (b)(c), respectively.
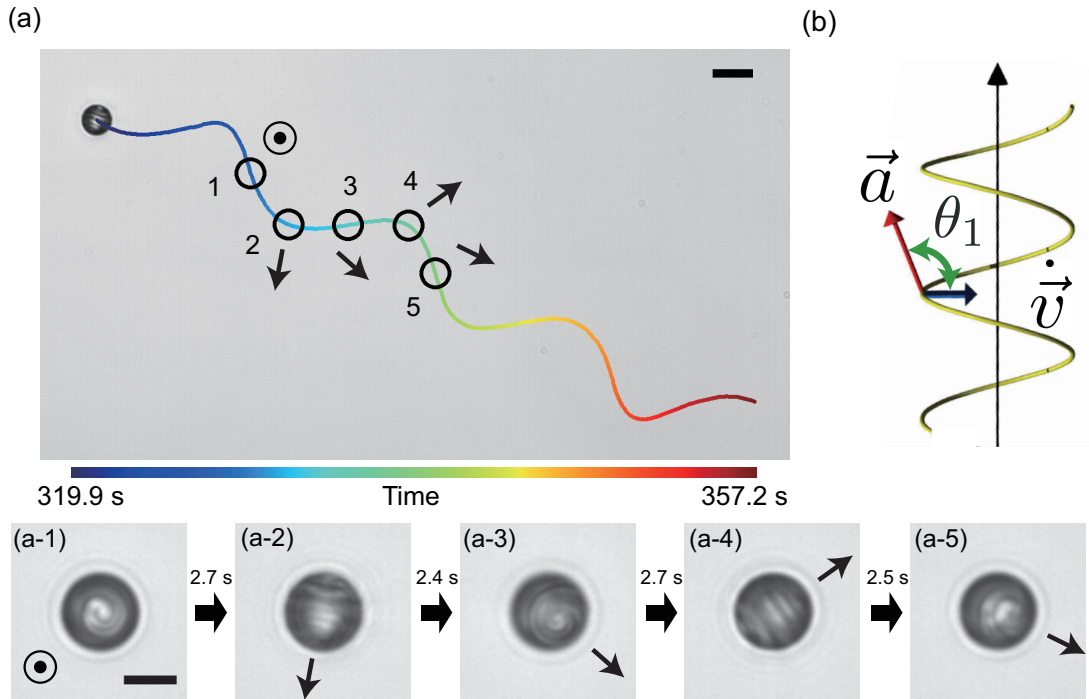
Figure 4.17: (a) 2D trajectory of the R811-doped CLC droplet shown in Fig. 4.14. The texture of the CLC droplet at the point $1 \sim 5$ in (a) correspond to (a-1) to (a-5). The arrows in (a), (a-1)~(a-5) indicate the direction of the helical axis of CLC droplets. (b) The schematic image showing the angle θ_1 defined in the main text. The scale bars in (a) and (a-1) are 20 μm and 10 μm, respectively.

4.9 Discussion

In Fig. 4.18, we depict the mechanism of the helical self-propulsion in the S-phase. In the case of the self-propelled NLC droplet, the Marangoni flow in the translational direction occurs inside the droplet as shown in Fig. 4.16 and previous reports [48, 90]. Thus, the Marangoni flow should occur also in the CLC droplet and determine the direction of the self-propelled motion. We consider that the helical motion can be driven by the chiral coupling between the Marangoni flow and the rotational motion through the helical director field of the CLC droplet. Such chiral coupling is probably relevant to the Lehmann effect, which is the cross coupling between rotational motion of the CLC and external thermodynamic force [19, 62, 21, 70]. We also consider that the helical motion appeared only in the S-phase, since the chiral coupling was enhanced due to the homogeneity of the helical director field.
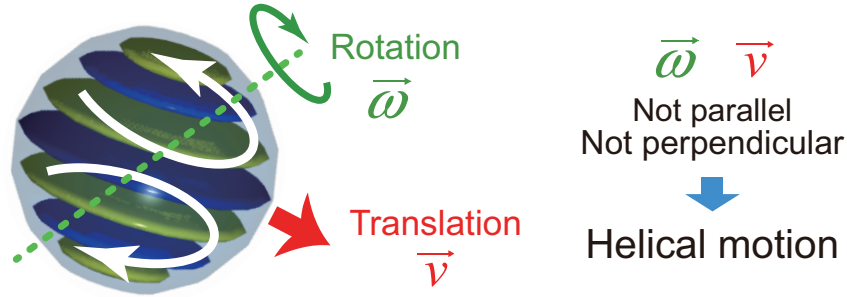
Figure 4.18: Schematic image of the mechanism of helical self-propulsion. The white curved arrows in the CLC droplet and red arrow represent the Marangoni flow and the translational motion, respectively. The green dotted line and curved arrow represent the rotational axis and the rotation, respectively.

4.10 Conclusion and remarks

To summarize, we have experimentally reported the chirality-induced helical motion of the artificial self-propelled microswimmer for the first time. Furthermore, we found that the CLC droplets change their textures during the locomotion, and the textures are correlated with the motion; D-phase, S-phase and I-phase. We showed that the transitions between these different phases are due to the balance between viscous and elastic force for that from D-phase to S-phase, and increasing chirality for that from S-phase to I-phase, respectively. In the D-phase, the CLC droplets showed the time-dependent deformation of the director field. In such cases, understanding the dynamics of the droplet is so difficult, and beyond our scope. However, in the future study, it will be interesting to quantify the deformation of the director field and investigate the correlation between the motion and the deformation.

Generally, helical motion appears only when the direction of velocity vector v and rotation vector ω of a CLC droplet are neither parallel nor perpendicular. To completely elucidate why such condition is satisfied in our experiments, understanding on the hydrodynamics inside/outside the droplet is required, perhaps achievable using fluid flow visualization techniques (Fig. 2.8, [62]) which do not disturb the director field of CLC. In the next chapter, we propose a phenomenological model which realize the chirality-induced helical motion of the CLC droplet, and obtain insights on the spontaneous emergence of the helical motion.

4.11 Appendix A: Density measurement of surfactant solution and cholesteric liquid crystal

Density of TTAB solution at various mixing ratio of D_2O and H_2O by weight and cholesteric liquid crystal doped with 2wt% R811 are shown in Fig. 4.19. We also show the data for lower surfactant concentration than 13wt%, which is the condition we applied in chapter 4, as references.
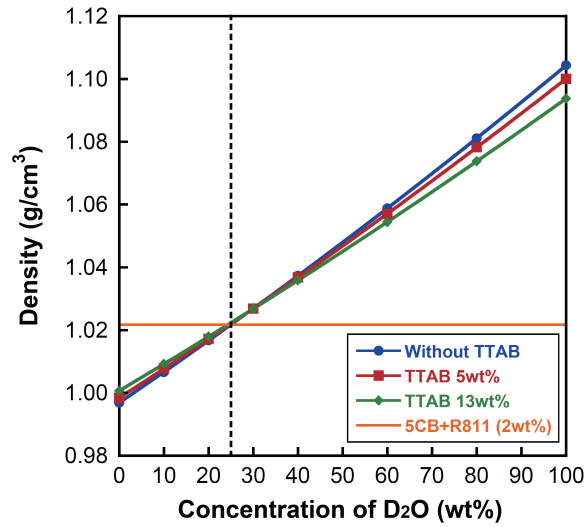
Figure 4.19: Density of TTAB solution and 5CB doped with 2wt% R811. The quadratic curves are fits to data. The dashed line indicates 25wt%, which is the condition we applied to eliminate the effect of buoyancy on the swimming behavior of CLC droplets.

4.12   Appendix B: Tracking algorithm

We made a python program to track a CLC droplet. The algorithm is as follows. While
the detail condition for the image analysis is different for each movie we captured, the
basic algorithms applied were common.

1. After enhancing the contrast of the original image by normalizing the intensity
   values over the range [0, 255] available for 8-bit images (Fig. 4.20(b)), blur
   the image to reduce the non-uniformity of the intensity due to the striped
   pattern (Fig. 4.20(c)).   For the blurring, median filter was performed with
   scipy.filters.median_filter.

2. Binarize using the function cv2.threshold from openCV library (Fig. 4.20(d)).

3. Fill   holes   in   a   binarized   image   of   a   droplet   using
   numpy.ndimage.binary_fill_holes (Fig. 4.20(e)).

4. Finally, detect the center of mass of the binarized image of the droplet
   (Fig. 4.20(e)). The center of mass of the original image is shown in Fig. 4.20(f).
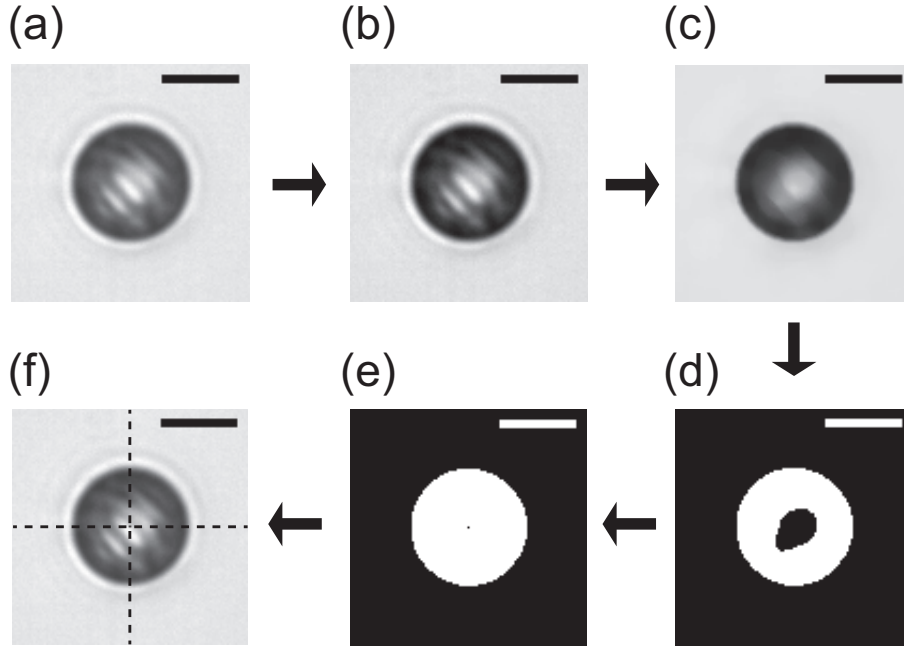
Figure 4.20: (a) An original image of a CLC droplet. (b) Enhancing the contrast. (c)
Blurring with median filter. (d) Binarization. (e) Filling hole. The black pixel at the
center shows the center of mass. (f) The intersection of two dashed lines shows the
center of mass in the original image. The scale bars are all 10 μm

Chapter 5

Model of chirality-induced helical self-propulsion of cholesteric liquid crystal droplets

In this chapter, we propose our theoretical model of the self-propelled helical motion of CLC droplets.

5.1 Introduction

Before we go on to our model of self-propelled motion of CLC droplets, we overview theoretical studies on the self-propelled isotropic droplets driven by the Marangoni effect. Since our CLC droplets swim in the world of micrometer scale, Reynolds number Re, a non-dimensional number characterizing the ratio of inertia to viscosity, is much smaller than 1 [32, 100]. Here, Reynolds number is defined as follows,

$$\text{Re} = \frac{\rho U L}{\eta},\tag{5.1}$$

where ρ is density, U, L is characteristic velocity and length, and η is viscosity. In low-Reynolds number world, the effect of inertia is unimportant, and hence the hydrodynamics is described by the Stokes equation, where inertial terms are dropped out from the Navier-Stokes equation. The Stokes equation is given as [12, 100],

$$-\nabla p + \eta \nabla^2 \boldsymbol{u} = 0,\tag{5.2}$$

where p is pressure, $\boldsymbol{u}$ is velocity field. Importantly, since the Stokes equation is a linear equation, we have analytical solutions [100]. Although there are examples of self-propelled droplets in high-Reynolds world which should be described by the Navier-Stokes equations [101, 88], here, we introduce self-propelled droplets in low-Reynolds world.

Consider a 2D situation where an isotropic oil droplet is immersed in a surfactant solution as shown in Fig. 5.1. As we showed in Chapter 4, we need to consider some non-equilibrium process such as dissolution, evaporation and chemical reactions for a droplet to swim spontaneously. Although each previous study considered various mechanisms [86, 48, 102, 103], here we consider a mechanism of self-propulsion considered in [103], where the surfactant is reactive and decompose at the interface at a constant rate. However, although detail calculations are different in each study, the concept and governing equations are similar. In such situation, we need to introduce hydrodynamic equations inside/outside the droplet, reaction diffusion equation for the surfactant, and boundary conditions for the interface, as follows:

$$-\nabla p + \eta \nabla^2 \boldsymbol{u} = 0, \quad \nabla \cdot \boldsymbol{u} = 0, \quad \text{(outside the droplet)}, \tag{5.3}$$

$$-\nabla \hat{p} + \eta \nabla^2 \hat{\boldsymbol{u}} = 0, \quad \nabla \cdot \hat{\boldsymbol{u}} = 0, \quad \text{(inside the droplet)}, \tag{5.4}$$

$$\frac{\partial c}{\partial t} + \boldsymbol{u} \cdot \nabla c = D_o \nabla^2 c - \kappa(c - c_\infty), \tag{5.5}$$

$$\hat{\sigma}_{r\theta}|_{r=R} = \sigma_{r\theta} + \frac{1}{R}\frac{\partial \gamma}{\partial \theta}, \tag{5.6}$$

$$\frac{\partial \Gamma}{\partial t} + v_\theta(R)\nabla_s\Gamma = D_s\nabla_s^2\Gamma - \kappa\Gamma + \left[D_o\frac{\partial c}{\partial r} - D_i\frac{\partial c}{\partial r}\right]_{r=R}, \tag{5.7}$$

$$\Gamma(\theta) = \gamma_0 + \gamma_c\Gamma(\theta), \tag{5.8}$$

$$\alpha\Gamma(\theta) = c(R, \theta). \tag{5.9}$$

Equations (5.3) and (5.4) are the Stokes equations and conditions for incompressibility for outer and inner fluids, respectively. The velocity fields and pressures are denoted as $\boldsymbol{u}, \hat{\boldsymbol{u}}, p, \hat{p}$ for inner and outer fluids. The field variables for the inner fluid are denoted with hat. Equation (5.5) is a reaction diffusion equation of surfactant in the outer fluid, where c denotes concentration of surfactant in outer fluid, D denotes diffusion constant. This model considers the supply of the surfactant to maintain a constant concentration c_∞ far from the interface, where the time scale is κ.

The model also requires boundary conditions at the interface. Here, the model assumes that the shape of the droplet remains circle with radius R. First, Eq. (5.6) is necessary to represent the stress jump at the interface. $\sigma, \hat{\sigma}$ denote the stress tensors at the interface, and γ denotes the surface tension at the interface, R is the radius of the droplet. Equation (5.7) is a reaction diffusion equation of surfactant at the interface, where Γ is the surfactant concentration at the interface, $v_\theta(R)$ denotes the velocity at the interface, D_s, D_o, D_i denotes the diffusion constants at the interface, in the outer fluid and the inner fluid, and κ is a decomposition rate. ∇_s represents a surface gradient. Furthermore, the model assumes a linear relationship Eq. (5.8) between the surfactant concentration $\Gamma(\theta)$ at the interface and the surface tension γ. Here, γ_0 denotes the surface tension without the surfactant and the coefficient γ_c is negative assuming that the surfactant reduces the surface tension. The last equation (5.9) represents the absorption of the surfactant at the interface from the bulk. The model assumes the adsorption-desorption equilibrium.

Chemical reaction
ex) Decompsotion of surfactant
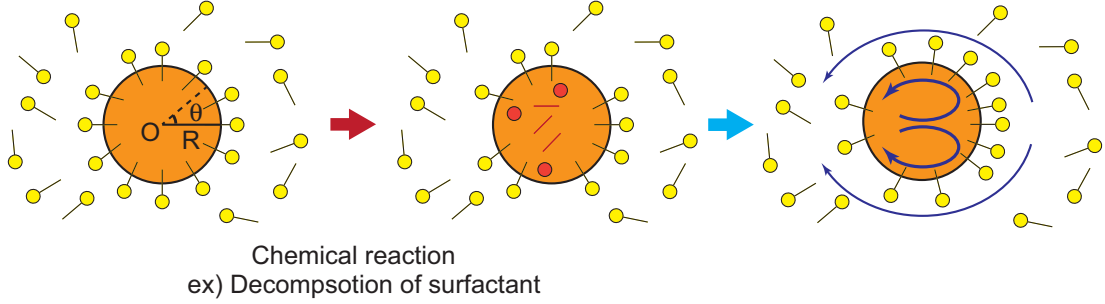
Figure 5.1: Schematic of the situation in [103]. The model assumes that the surfactant is reactive and decomposes at the interface. Spontaneous emergence of the surfactant concentration gradient at the interface induces the Marangoni flow, and the droplet starts swimming spontaneously.

These equations or the analogous were solved numerically and analytically with help of perturbation theory [102, 103]. It is commonly reported that the self-propelled motion of droplets emerges depending on the parameters.

Despite these development in theoretical studies, in the case of LC droplets as our experiment, the analytical and even numerical approach are challenging since the hydrodynamic equations of LC are highly nonlinear. Here, in the dissertation, we construct our theoretical model phenomenologically by symmetry argument.

5.2 Phenomenological models of a self-propelled object

We introduce phenomenological models of self-propelled objects originally proposed by Ohta and Ohkuma [52]. Importantly, since these models are constructed only by symmetry argument, the models are not restricted to the self-propelled droplets and hence quite general. Furthermore, the models are analytically tractable.

5.2.1 Ohta-Ohkuma model [52]

Ohta-Ohkuma model was proposed to universally describe the dynamics of deformable self-propelled objects; self-propelled domains in excitable reaction diffusion systems [104] and self-propelled living cells such as keratocyte [105]. For the latter case, they focused on the fact that cells move with their body deformed and the motion is correlated with the deformation. For instance, a keratocyte tends to move toward the short-axis of its elongated body. In their model, the dynamics of such deformable objects was described by a set of simple equations constructed by symmetry argument. As schematically depicted in Fig. 5.2, they represented the shape of a object with a traceless second rank tensor S_{ij} defined as $S_{ij} = S(n_i n_j - \frac{1}{d}\delta_{ij})$, where $\boldsymbol{n}$ is a long axis of the object, S indicates the degree of the deformation from a circle in 2D and a sphere in 3D, and d is a spatial dimension. The model was originally constructed in 2D,

and extended to 3D model by Hiraiwa et al. [106]. Note that the traceless tensor was
introduced to represent the conservation of the volume of the object. The velocity of
the center of mass of the object was denoted as v. Keeping relevant terms, we obtain
a set of time-evolution equations describing the dynamics of v and S_{ij} by symmetry
argument as follows:

$$\frac{dv_i}{dt} = \gamma v_i - |v^2|v_i - a_1 S_{ij} v_j, \tag{5.10}$$

$$\frac{dS_{ij}}{dt} = -\kappa S_{ij} + b_1(v_i v_j - \frac{1}{d}|v^2|\delta_{ij}). \tag{5.11}$$

In Eq. (5.10), if $\gamma > 0$, the first two terms in the right-hand side correspond to a
wine-bottle potential (Fig. 5.3) which allow the object to move spontaneously with a
finite value of velocity. We describe such condition with a term "Active". Otherwise,
the motion of the object damped to stop, which is described by a term "Passive".

Here, we explain these terms essential for self-propulsion of objects in a simpler
example. Let us consider an isotropic self-propelled object which moves in 1D space
due to spontaneous symmetry breaking. In such a case, we can write the equation of
motion of the object as follows:

$$\frac{dv}{dt} = \gamma v - v^3, \tag{5.12}$$

where v is the velocity of the object in 1D. If $\gamma < 0$, the equation has an only trivial
solution $v = 0$ in the steady state. In contrast, if $\gamma > 0$, the solution $v = 0$ becomes
unstable and $v = \pm \sqrt{\gamma}$ are the stable solutions. Hence, while the self-propelled object
does not move in $\gamma < 0$, it moves with the steady velocity $v = \pm \sqrt{\gamma}$ in $\gamma > 0$. Note that
this equation is the normal form of pitchfork bifurcation in dynamical system [107].

The last term in the right-hand side of Eq. (5.10) represents the anisotropy of the
motion of the elongated objects. The sign of a_1 determines which direction is the easy
axis of the objects, long axis or short axis. Equation (5.11) is a time-evolution equation
of the deformation of the object. In the first term, κ was set to positive considering
the shape of the object should damp to a circle in 2D and a sphere in 3D due to the
interfacial tension in the case of self-propelled droplets and cells. However, the sign of
κ is not necessarily positive in general. The latter terms were introduced to describe the
coupling between the translational motion and the shape deformation.

In spite of the simple form of the model, the self-propelled object shows various
types of motion depending on the parameters; *translation, circular motion in 2D,
helical motion in 3D*. Note that bifurcations were associated with the transitions between
different types of motions.

Importantly, Hiraiwa et al. extended the Ohta-Ohkuma model to a 3D model [106].
The authors reported that the model exhibits a helical motion. However, *since the model
has the spatial reflection symmetry, the left-handed and right-handed helical motion
appear in the same ratio* 50 : 50.

$$Q_{ij} = S(n_i n_j - \frac{1}{d}\delta_{ij})$$
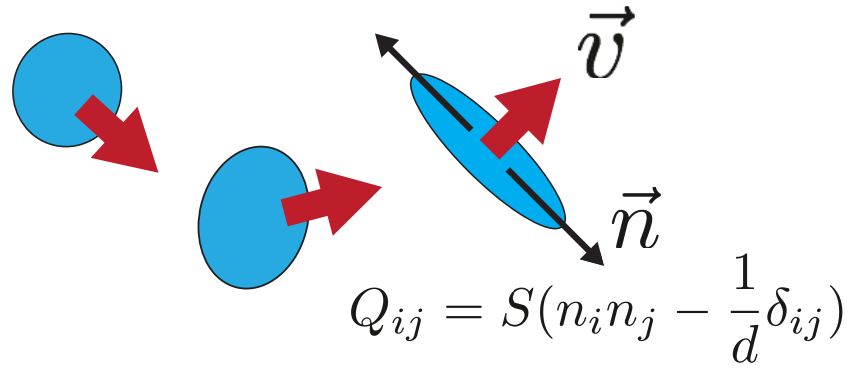
Figure 5.2: Schematic of the concept of Ohta-Ohkuma model [52].

$$\gamma < 0 \qquad \gamma > 0$$

Passive   Active
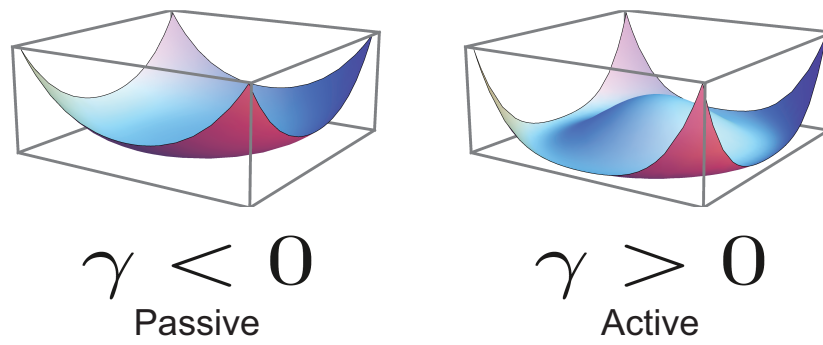
Figure 5.3: Schematic of the wine-bottle potential.

5.2.2 Tarama-Ohta model [108]

After the Ohta-Ohkuma model was proposed, the degrees of freedom of angular velocity ω, where they define $\Omega_{ij} = \epsilon_{ijk}\omega_k$, were added to the equations of motions by Tarama and Ohta in 2D [109] and 3D [108] (Fig. 5.4). Here, we introduce the model in 3D [108] as follows:

$$\frac{dv_i}{dt} = \gamma v_i - |v^2|v_i - a_1 S_{ij} v_j - a_2 \Omega_{ij} v_j, \tag{5.13}$$

$$\frac{dS_{ij}}{dt} = -\kappa S_{ij} + b_1(v_i v_j - \frac{1}{d}|v^2|\delta_{ij}) + b_2(S_{ik}\Omega_{kj} - \Omega_{ik}S_{kj})$$

$$+ b_3\{\Omega_{ik}S_{kl}\Omega_{lj} - \frac{1}{d}(\Omega_{mk}S_{kl}\Omega_{lm})\delta_{ij}\}, \tag{5.14}$$

$$\frac{d\Omega_{ij}}{dt} = -\frac{\delta G}{\delta \Omega_{ij}} + c_1(S_{ik}\Omega_{kj} + \Omega_{ik}S_{kj}) + c_2 S_{ik}\Omega_{kl}S_{lj}, \tag{5.15}$$

$$\text{where} \quad G \equiv \frac{\zeta}{2}\mathrm{tr}\Omega_{ij}^2 + \frac{1}{4}\mathrm{tr}\Omega_{ij}^4. \tag{5.16}$$

The physical meanings of each term are explained in [108]. Note that a term representing the self-rotational motion was introduced in addition to the self-propulsion in the translational direction represented by the first two terms in the right-hand side of Eq. (5.13). The first term in Eq. (5.15), that is $-\frac{\delta G}{\delta \Omega_{ij}} = (\zeta - \omega^2)\Omega_{ij}$, represents such self-rotational motion. Such self-rotational motion which spontaneously occurs is experimentally reported in [101], where a water droplet on the silicon oil rotates spontaneously when vibrated vertically.
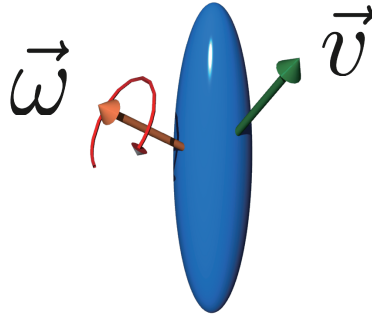
Figure 5.4: Schematic of the Tarama-Ohta model [108].

Again, importantly, the Tarama-Ohta model in 3D also exhibits a helical motion as well as the Ohta-Ohkuma model in 3D. However, since the model has the spatial reflection symmetry, the left-handed and right-handed helical motion appear in the same ratio 50 : 50.

5.2.3   Higher-order shape deformations

In the two phenomenological models above, the models employed second rank tensor S_{ij} to represent the shape of the self-propelled objects. However, the objects such as cells generally deform into more complicated shapes. In such cases, we can represent the shape of the objects with higher-order tensors such as $U_{ijk}, T_{ijkl}...$ and keep relevant terms out of such higher order terms [110, 111]. Importantly, although we saw examples where these tensors explicitly represent the shape of the objects, *the tensors can also represent the internal symmetry as we do in our model in the following sections.* In that sense, these phenomenological approach provides us highly general way to describe the dynamics of the self-propelled objects.

5.2.4   Derivation of the phenomenological models from hydrodynamic equations

Importantly, such phenomenological models of a self-propelled object were recently derived in the case of the self-propulsion of the isotropic self-propelled droplet driven by the Marangoni flow by removing the degrees of freedom of the concentration field using perturbation theory [102, 103]. For instance, in the case as sketched in Fig. 5.1 [103], the following equation of motion of the self-propelled droplet in 2D was reduced from the hydrodynamic equations of an isotropic droplet and the surrounding fluid,

$$\frac{dv_i}{dt} = \gamma v_i - v_j v_j v_i, \tag{5.17}$$

where the notion of coefficients are different from [103]. Assuming that the time-evolution of the coarse-grained variables v, S_{ij}, Ω_{ij} etc. are described by the analytic functions, the reduced model is just an expansion of such functions. Hence, even if such models cannot be necessarily derived from the detailed model such as hydrodynamic equations for a self-propelled droplet or dynamics of ingredient of a cell, such reduced model should play important roles to model and predict novel phenomena theoretically.

5.3   Models of helical motion

Here, we briefly introduce several models of helical motion of a single object previously reported.

1. Models which are *a priori* designed to exhibit helical motion [80, 112, 81].

2. Hydrodynamic modeling of helical motion of microorganisms such as sperms [28].

3. Models of helical motion under external fields [113].

4. Achiral models of helical motion which emerges due to the spontaneous symmetry breaking [106, 108].

5. Chiral models of helical motion which emerges owing to the self-propulsion and the chirality (A model of helical motion of *Listeria monocytogenes*) [114].

The first models are trivial models where the helical motion is designed *a priori* [80, 112, 81]. In these models, the motion of an object is often described using the Frenet-Serret frame, which can describe the arbitrary continuous and differentiable curve in 3D. The detail in the Frenet-Serret frame is explained in Appendix A. In such models, dynamics of the objects are described by,

$$\dot{r} = vt, \tag{5.18}$$
$$\dot{t} = v\kappa n, \tag{5.19}$$
$$\dot{n} = -v\kappa t + v\tau b, \tag{5.20}$$
$$\dot{b} = -v\tau n, \tag{5.21}$$

where the position and the absolute velocity of the object are denoted as r and v. Also, the tangent vector t, normal vector n and binormal vector b are defined as $t = \dot{r}/v$, $n = \dot{t}/|\dot{t}|$, $b = t \times n$ (Fig. 5.5, see also Appendix A for the detail). In such models, since both curvature and torsion of the helical trajectory represented by κ and τ are set *a priori*, helical motion appears trivially.
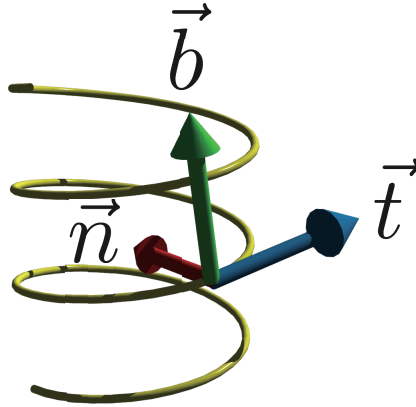
Figure 5.5: Unit vectors n, t and b defined on the Frenet-Serret frame. The yellow curve represents a helical trajectory.

In the second models, the shape and motion of microorganisms which exhibit helical motion are modeled in detail using hydrodynamic theory. For instance, in [80], the body of a sperm is modeled as a rigid body and designed to deform in low-Reynolds number fluid. In the numerical simulation of hydrodynamics, chiral motion of the body made the sperm swim in a helical path as observed in nature.

In the third models, the object does not move spontaneously but owing to some external field such as electromagnetic field and gravity [113]. A famous example is an electron which moves in helical path under magnetic field and electric field.

The fourth models are models we saw in Sec. 5.2, which are phenomenological models of deformable self-propelled particles in 3D [106, 108]. Since these models are achiral models, helical motion can spontaneously appear associated with bifurcations due to the coupling between motion and deformation of the object. The Ohta-Ohkuma model and the Tarama-Ohta model in 3D exhibit a helical motion. However, since the models have the spatial reflection symmetry, the left-handed and right-handed helical motion appear in the same ratio 50 : 50.

The fifth model was recently proposed in [114] to explain the helical motion of *Listeria monocytogenes*, which is a bacteria exhibiting right-handed helical motions in a cytoskeletal (actin) medium [115]. *Listeria* polymerizes actin monomers into actin filaments at the surface of the body, and moves around being pushed by the elastic force of the polymerized actin filaments. In fact, *Listeria* exhibits helical motions owing to the actin-based self-propulsion and the chirality. In [114], the authors simplified the situation, and considered a micron-sized spherical bead uniformly coated with actin polymerization protein dispersed in actin-rich medium. They constructed the time-evolution equations (partial differential equations) of the actin filament density and force per filament at the surface of the bead, and calculated the velocity and angular velocity of the bead from the force and torque generated by the actin filaments. By phenomenologically introducing the chiral terms with pseudo scalar coefficients in the time-evolution equations of the actin filament density and force per filament, they showed that their model realizes the helical motion whose handedness is determined by the sign of the pseudo scalar coefficients.

In our experiments on the helical self-propulsion of a CLC droplet (Chapter 4), we found that

- the CLC droplets start swimming due to the spontaneous symmetry breaking,

- the handedness of the helical motion is determined by the chirality of the CLC droplet (Fig. 4.14 and 4.15),

- the CLC droplets exhibit helical motions when the droplets have the uniform helical director field without deformation (Fig. 4.10).

When we model the swimming CLC droplet, the model should be consistent with these experimental results.

In the following sections, we model the swimming CLC droplet using the phenomenological approach as developed by Ohta and Ohkuma [52]. *Such phenomenological approach has the advantage of analytical tractability. Furthermore, since the model is constructed by symmetry argument and irrespective of details of system, it allows us to treat phenomena with the same symmetry in the same framework.*

5.4   Our model of a CLC droplet

In our experiments described in Chapter 4, we found that the CLC droplets exhibit
the helical motion only when the droplets have the homogeneous helical director field
without deformation. Hence, we construct a model of the CLC droplets with such
homogeneous helical director field.

5.4.1   Model equations

Based on the concept of the phenomenological models as we saw above, we constructed
a theoretical model describing the helical self-propulsion of a CLC droplet. We describe
the dynamics of a CLC droplet by a coupled Eqs. (5.23)-(5.25) in terms of a velocity v,
an angular velocity ω and a second rank traceless symmetric tensor Q_{ij} representing the
helical axis inside the droplet. To describe the global symmetry of a whole CLC droplet
with a helical director field, we define the second rank tensor as follows:

$$Q_{ij} = \frac{S}{2}(3a_i a_j - \delta_{ij}) + \frac{P}{2}(b_i b_j - c_i c_j), \tag{5.22}$$

where a, b and c are unit vectors. The primary axis a represents the direction of the
helical axis of the director field (Fig. 5.6(a)). We did not directly use the vector a
but the second rank tensor Q_{ij} to represent the helical axis of the droplet, because a
and $-a$ are equivalent in the case of homogenesous helical director field. Note that
the CLC molecules themselves align perpendicularly to a. Hence, the meaning of Q_{ij}
in our model is different from that of the tensor order parameter defined in the NLC,
which we introduced in Sec. 2.1 [10, 58]. We may also consider a biaxial parameter
P and the secondary axes b and c, where $a \perp b$ and $b \perp c$, since, if we look at the
plane crossing the center of the droplet and perpendicular to a, CLC molecules align
in a certain preferred direction. S and P represent the degree of anisotropy of the CLC
droplet. Here, we investigate the qualitative behavior of our model by setting $S = 1$ and
changing the value of P.

Using the definition of the structure Q_{ij} of a CLC droplet, we constructed the
following time-evolution equations by considering the possible terms in a chiral system,
which we underline below, and keeping some relevant terms:

$$\begin{aligned}
\frac{dv_i}{dt} &= \gamma v_i - v_j v_j v_i + a_1 Q_{ij} v_j + a_2 \epsilon_{ijk} \omega_j v_k \\
&\quad + \underline{\mu^{\text{iso}} \omega_i + \mu Q_{ij} \omega_j}, \tag{5.23} \\
\frac{d\omega_i}{dt} &= \zeta \omega_i - \omega_j \omega_j \omega_i + c_1 Q_{ij} \omega_j + c_2 \epsilon_{ijk} Q_{jl} v_l v_k \\
&\quad + \underline{\nu^{\text{iso}} v_i + \nu Q_{ij} v_j}, \tag{5.24} \\
\frac{dQ_{ij}}{dt} &= \epsilon_{kjl} Q_{ik} \omega_l - \epsilon_{ikl} \omega_l Q_{kj}. \tag{5.25}
\end{aligned}$$
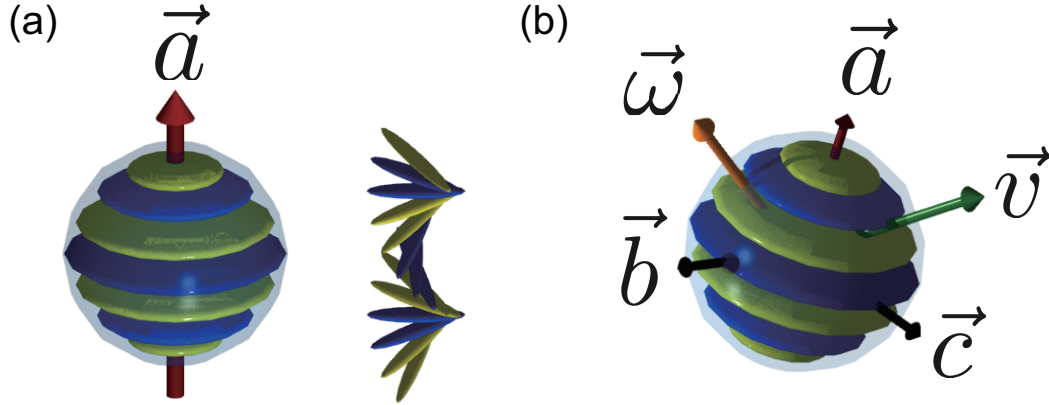
Figure 5.6: Schematic of the definition of (a) helical axis $\boldsymbol{a}$ and (b) dynamical variables in our model.

We follow the Einstein summation convention and ϵ_{ijk} is a Levi-Civita symbol. Note that, the coefficients, $\gamma, \zeta, a_1, a_2, c_1, c_2$, are scalars allowed even in achiral systems, while $\mu^{\text{iso}}, \mu, \nu^{\text{iso}}, \nu$ are *pseudo scalars allowed only in chiral systems.*

5.4.2   Achiral terms with scalar coefficients

The meaning of each term with scalar coefficients in Eqs. (5.23)-(5.25) is as follows: The first and second terms of the right-hand side of Eqs. (5.23) and (5.24) represent the self-propulsion in the translational and rotational motion as a result of the spontaneous symmetry breaking, respectively. If γ or ζ are positive, the droplet has an injection of the energy, resulting in the self-propelled dynamics [52, 108]; otherwise, the terms mean a damping force and torque. We consider that $\gamma > 0, \zeta < 0$ in our experiments, since the dynamics of the droplet is triggered by the gradient of the surface tension, which results in the Marangoni flow and then translational self-propulsion. In general, the rotational self-propulsion may exist in some systems. For instance, a water droplet on the silicon oil rotates spontaneously when vibrated vertically [101]. In such a case, ζ should be positive.

The terms with the coefficients a_1 and c_1 represent the anisotropy of self-propulsion or damping. The signs of the coefficients determine the easy axis of the translation or rotation. If the coefficients are positive, $\boldsymbol{a}$ is the easy axis. Otherwise, while any direction perpendicular to $\boldsymbol{a}$ is the preferred direction in uniaxial case, an eigenvector corresponding to the minimum eigenvalue of Q_{ij} is the preferred direction in biaxial case.

The terms with a_2 and c_2 are the lowest order terms describing the achiral coupling between $\boldsymbol{v}$ and $\boldsymbol{\omega}$ in each time-evolution equation. The term with a_2 means the turning of the translational direction due to the rotation. The term is written as $a_2 \boldsymbol{\omega} \times \boldsymbol{v}$ in the vectorial representation. a_2 should approach 1 from 0, as the coupling between $\boldsymbol{v}$ and $\boldsymbol{\omega}$

gets stronger. We discuss the term with c_2 in detail later.

Finally, Eq. (5.25) represents that the vectors $\boldsymbol{a}, \boldsymbol{b}$ and $\boldsymbol{c}$ associated with the CLC droplet change the direction with the angular velocity $\boldsymbol{\omega}$. The helical director field of the CLC droplet did not deform during helical motion in our experiments. Hence, the eigenvalues of Q_{ij} is fixed in our model, in contrast to the model with deformation we introduced in Sec. 5.2.

5.4.3 Chiral terms with pseudo scalar coefficients

The most essential part of our model is the coupling terms with pseudo scalar coefficients $\mu^{\mathrm{iso}}, \mu, \nu^{\mathrm{iso}}, \nu$, which represent the chiral coupling between the translation induced by the Marangoni flow and the rotation through the helical director field of the CLC droplet. Since these terms are the off-diagonal couplings in the linear non-equilibrium thermodynamics [11], we expect the reciprocal relation and hence assume that $\mu^{\mathrm{iso}} = \nu^{\mathrm{iso}}$ and $\mu = \nu$.

For clarity, we explicitly write down the terms $\nu^{\mathrm{iso}} v_i + \nu Q_{ij} v_j$ in the time-evolution Eq. (5.24) for ω_i for the uniaxial case ($P = 0$) for simplicity. Here, we define $\Gamma_i = \nu^{\mathrm{iso}} v_i + \nu Q_{ij} v_j$. Consider the situation, where $\boldsymbol{v}$ is parallel to z-axis as shown in Fig. 5.7(b). Also, assuming the helical axis $\boldsymbol{a} = (0, \sin\theta, \cos\theta)$, we obtain,

$$\Gamma = \frac{3\nu v}{2}(0, \sin\theta\cos\theta, \cos^2\theta + \frac{2\alpha}{3}), \tag{5.26}$$

where v is the absolute value of $|\boldsymbol{v}|$, and α is introduced to satisfy $\nu^{\mathrm{iso}} = (\frac{1}{2} + \alpha)\nu$ for convenience. We show the θ dependence of the y- and z-components of $\boldsymbol{\Gamma_0} \equiv (0, \sin\theta\cos\theta, \cos^2\theta + \frac{2\alpha}{3})$ for different α in Fig. 5.7(a). Figure 5.7(a) shows that

1. when $\alpha \geq 0$, $\Gamma_z > 0$ for any θ. Hence, the direction of the rotational motion around the direction of $\boldsymbol{v}$ is independent on θ. Furthermore, the rotational velocity is higher when the helical axis $\boldsymbol{a}$ is parallel to $\boldsymbol{v}$ than when the axis is perpendicular to $\boldsymbol{v}$.

2. when $0 \geq \alpha \geq -1.5$, the sign of Γ_z is changed at some value θ. Hence, the direction of the rotational motion around the direction of $\boldsymbol{v}$ is inversed at some value of θ.

3. when $-1.5 \geq \alpha$, $\Gamma_z < 0$ for any θ. In contrast to the case 1, the rotational velocity is higher when the helical axis $\boldsymbol{a}$ is perpendicular to $\boldsymbol{v}$ than when the axis is parallel to $\boldsymbol{v}$.

All the cases are permitted due to the symmetry argument, and each case should be selected dependent on the details of the systems. Although we do not know how the CLC droplets response to the Marangoni flow for the moment, we consider that the case 1 is reasonable, since the CLC droplets response to the temperature gradient in such ways as we saw in Chapter 3, where the rotational velocity of the CLC droplet was larger

when the temperature gradient is parallel to the helical axis than when it is perpendicular to the helical axis. Hence, we set $\alpha > 0$ in this chapter. Further experimental and theoretical investigations on the behaviors of CLC under the Marangoni flow are required to clarify this assumption by the analogy to the experimental results in the Lehmann effect.
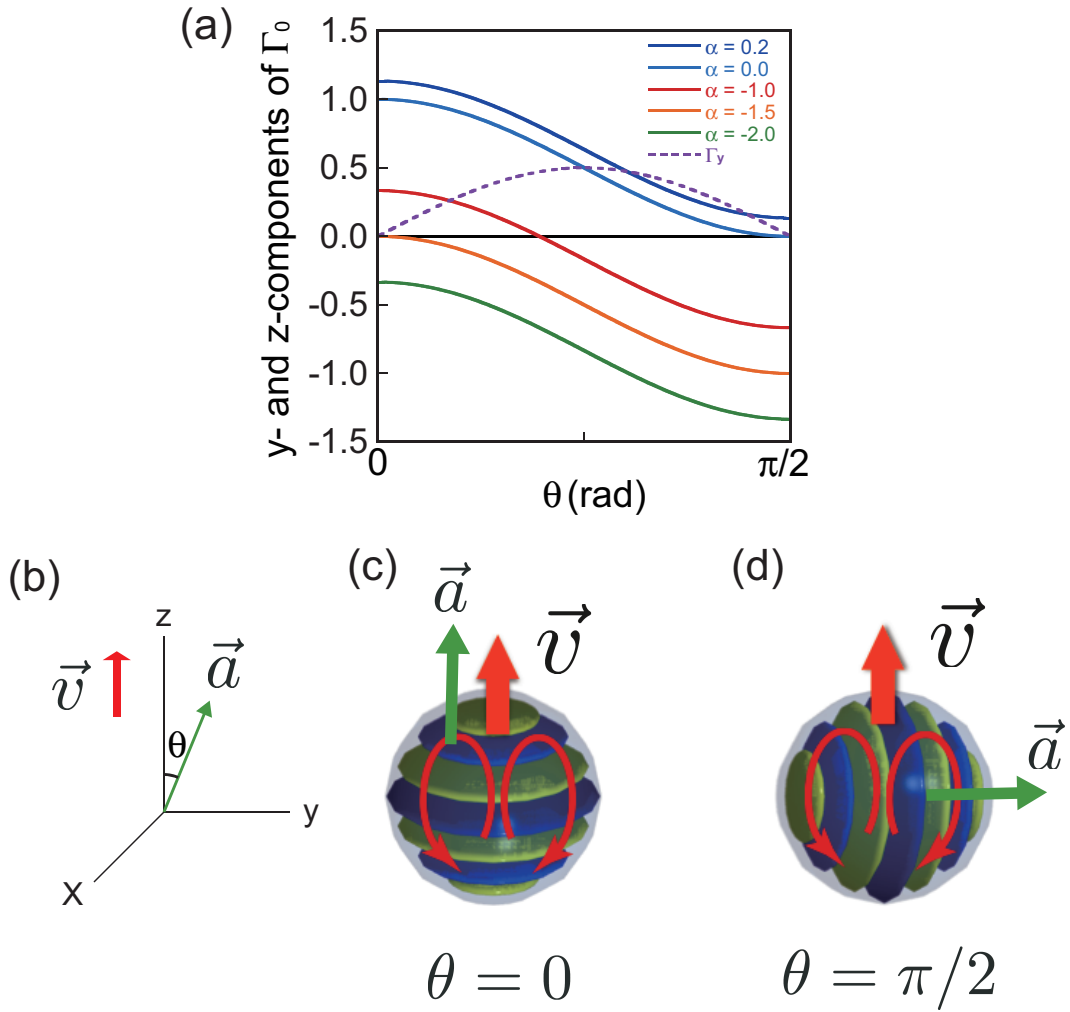
Figure 5.7: (a) θ dependence on the x- and y-components of Γ defined in Eq. (5.26). The solid lines indicate Γ_z for different α, and the dotted line indicates Γ_y. (b) Coordinates and the definition of θ are shown schematically. (c)(d) Schematic of configurations of the droplet corresponding to $\theta = 0$ and $\theta = \pi/2$, respectively.

5.5   Behavior of our model

5.5.1   Setup

Numerical simulations were performed based on Eqs. (5.23)-(5.25) by the 4th-order Runge-Kutta method ($\Delta t = 1.0 \times 10^{-4}$). We investigate the dynamics by changing the strength of the self-propulsion γ, the chiral couplings $\mu^{\text{iso}}, \mu, \nu^{\text{iso}}, \nu$ and c_2. For simplicity, we control the strength of chiral couplings with a pseudo scalar parameter μ by setting $\mu = \nu, \mu^{\text{iso}} = \nu^{\text{iso}} = 0.7\mu$ (that is, $\alpha = 0.2$). The other parameters are fixed as $a_1 = -1, a_2 = 0.9, \zeta = -3, c_1 = 0$. Here, a_1 is set negative for the following reason. It is reported that the effective viscosity in the direction of the helical axis is comparably higher than that perpendicular to the helical axis [14] (See Fig. 5.8). Hence, the Marangoni flow, which induces the translation, is likely to occur perpendicularly to the helical axis to minimize the dissipation. a_2 is set to be smaller than 1, since the surfactant concentration field around the droplet, which is the origin of the translation v, should not fully follow the rotation ω. In addition, we consider isotropic damping of rotational motion ($\zeta < 0, c_1 = 0$), since the droplet is spherical. Furthermore, we examine the effect of the biaxiality by setting either $P = 0$ or $P = 0.1$.

High viscosity   Low viscosity
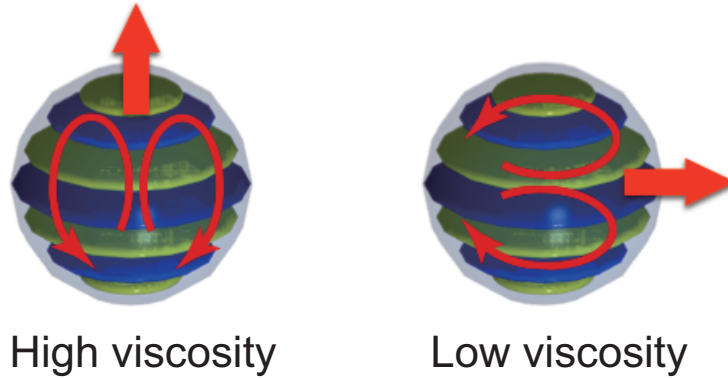
Figure 5.8: Anistropy of viscosity in a CLC droplet. The viscosity is higher in the direction parallel to the helical axis than in that perpendicular to it.

5.5.2   Phase diagram

Figure 5.9 shows the phase diagrams as results of numerical simulations and linear stability analysis of Eqs. (5.23)-(5.25) in both the uniaxial and biaxial case ($c_2 = 0.4$). We numerically obtained five phases: No motion (N), Straight motion (ST), Spinning Straight motion (SS) along Secondary axis (SSS) and Primary axis (SSP), and Helical motion (H). In N phase, the droplet is motionless. In ST phase, the droplet moves perpendicularly to a without any rotation, which is observed in the limit of $\mu = 0$. SS is a phase where the droplet moves with $v \parallel \omega$. SS can be classified into two phases, SSS and SSP, where v is perpendicular and parallel to a, respectively (See Fig. 5.10).

Since SSS and SSP are predicted for the first time in our model, we hope that the two phases are experimentally realized. When neither $v \parallel \omega$ nor $v \perp \omega$, we classify the motion into H phase. In H phase, the helix was right-handed, when $\mu > 0$. Importantly, changing the sign of μ, namely, inversion of the chirality, provided a mirror image of the dynamics, consistent with our experiments.
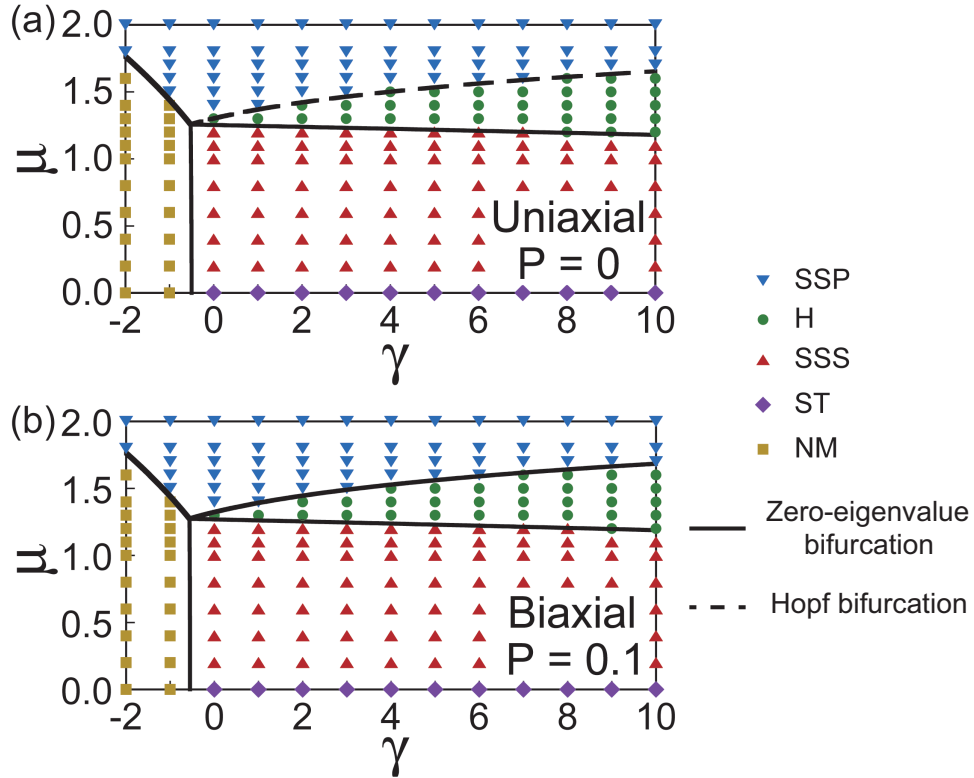
Figure 5.9: (a)(b) Phase diagrams in the uniaxial ($P = 0$) and biaxial case ($P = 0.1$), respectively (square: NM, upward triangle: SSS, downward triangle: SSP, diamond: ST and circle: H). The lines indicate linear stability limits of NM, SSS and SSP (Solid line: zero-eigenvalue bifurcation, dashed line: Hopf bifurcation).

In Fig. 5.9(a)(b), the lines indicate the linear stability limit of NM, SSS and SSP phases, consistent with the numerical results. We show the detail in the bifurcation analysis in Appendix C. In the uniaxial case $P = 0$, zero-eigenvalue bifurcations[1] occur at the N–SSS, N–SSP and SSS–H boundaries, whereas the Hopf bifurcation occurs at the SSP–H boundary. The Hopf bifurcation at the SSP–H boundary in the uniaxial case is probably related to the rotational symmetry around $a \parallel v \parallel \omega$ in SSP. In contrast, this rotational symmetry is broken in the biaxial case.

---

[1]Following [107], zero-eigenvalue bifurcation means a bifurcation in which a real eigenvalue passes through $\lambda = 0$. Here, λ represents the eigenvalue.
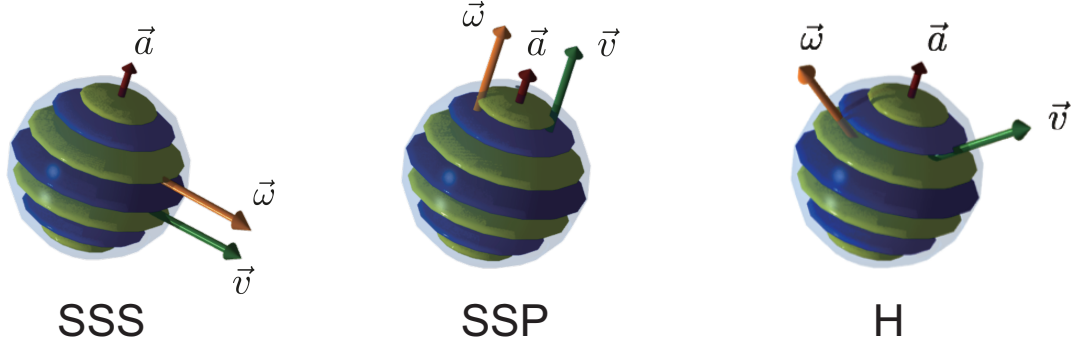
Figure 5.10: Schematic images of SSS, SSP and H, respectively. Each arrow represents a, v and ω.

5.5.3 Dynamics

In our model, whether the droplet is uniaxial or biaxial also plays a key role in the dynamics of helical motion. Fig. 5.11 shows the time-evolution of several essential variables in helical trajectories for uniaxial and biaxial cases, which identify the helical motion. In both uniaxial case $P = 0$ and biaxial case $P = 0.1$, we numerically found that the helical path is the perfect helix, that is, the curvature κ and torsion τ of the path are time-independent in the steady state as shown in Fig. 5.11(a) for a uniaxial case and (e) for a biaxial case, respectively. Here, the curvature κ and torsion τ of the trajectories were calculated following the definition in Appendix A. $|v|$ and $|\omega|$ are also time-independent (Fig. 5.11(b)(c)(f)(g)).

In contrast, the detail of rotational motion is different in both cases. We define the angular velocity Ω of the helical motion, which is parallel to the helical axis of the path as shown in Fig. 5.12. Furthermore, in order to identify the spatial relationship between the direction of the helical axis Ω of the trajectory and the helical axis a of the droplet, we introduce the angle θ_1 and θ_2, which are defined as $\theta_1 = \arccos\left(\dot{v} \cdot a / |\dot{v}|\right)$ and $\theta_2 = \arccos\left(-\ddot{v} \cdot a / |\ddot{v}|\right)$. θ_1 and θ_2 are depicted schematically in Fig. 5.12(b) and (c), respectively. Fig. 5.11(g) and (g-2) show that, in the biaxial case $P = 0.1$, ω coincides with Ω. Whereas, Fig. 5.11(c) and (c-2) show that, in the uniaxial case, oscillation of the components of ω and a deviation between $|\omega|$ and $|\Omega|$ are observed. Focusing on the dynamics of θ_1 and θ_2, they were time-independent for both cases in the steady states (Fig. 5.11(d) and (h)). Hence, we find that, in the uniaxial case, an additional rotational motion around the helical axis a of the CLC droplet occurs during the helical motion. The oscillation should be originated from a limit cycle in H phase, consistent with the Hopf bifurcation in the uniaxial case. The insight in the uniaxial limit $P = 0$ will be important, since the biaxiality of the CLC droplet should decrease to vanish as the wave number q of the helical director field gets larger.
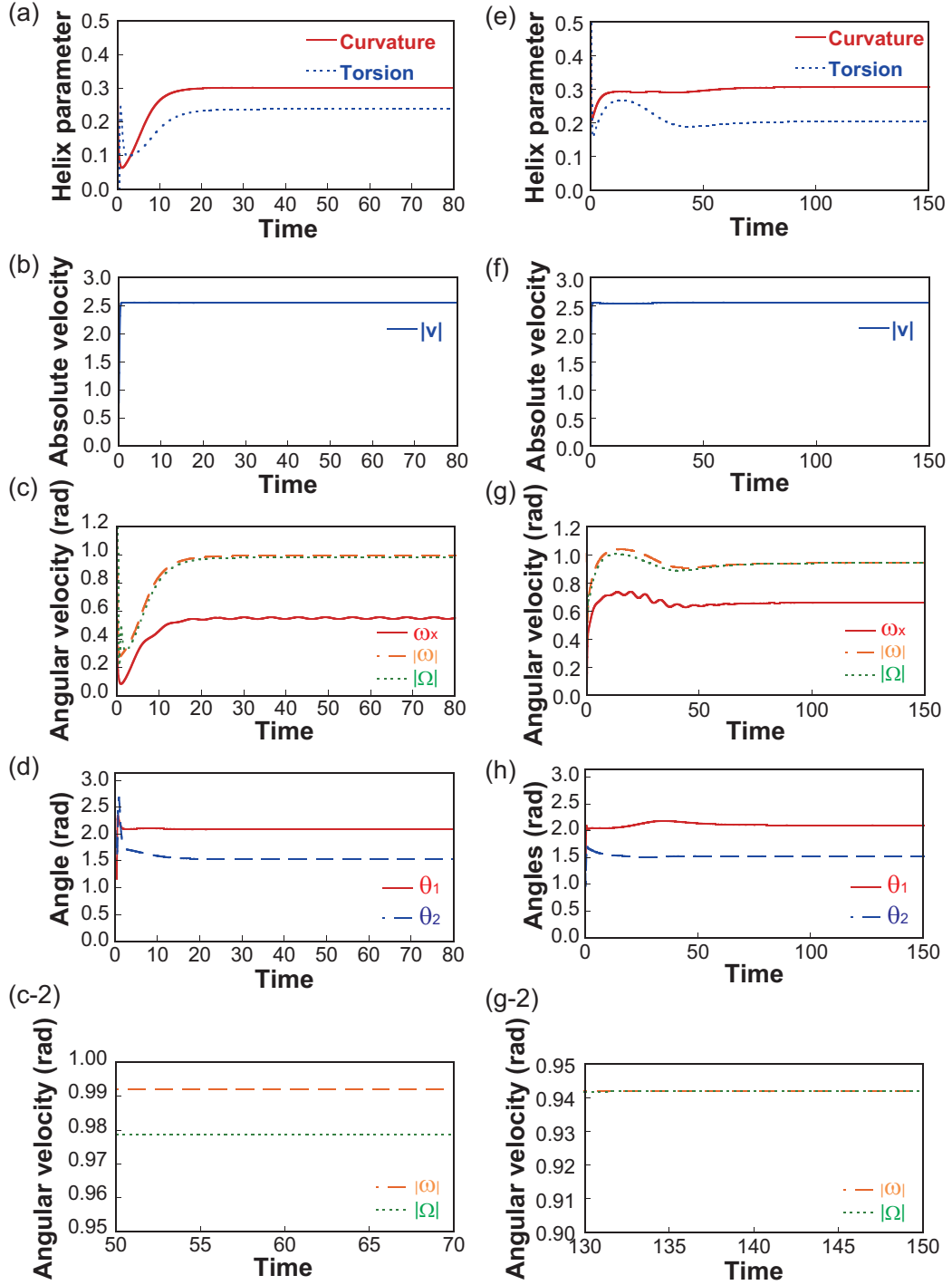
Figure 5.11: Time-evolution of (a) curvature κ and τ, (b) absolute value of velocity v, (c) x component ω_x of ω, absolute values of ω and Ω, (d) θ_1 and θ_2 in a helical motion ($P = 0, c_2 = 0.4, \gamma = 6, \mu = 1.4$). The same properties in a helical motion for a biaxial case ($P = 0.1, c_2 = 0.4, \gamma = 6, \mu = 1.4$) are shown in (e-h). Also, the enlarged time-series of $|\omega|$ and $|\Omega|$ are shown in (c-2) and (g-2) for uniaxial and biaxial cases, respectively.
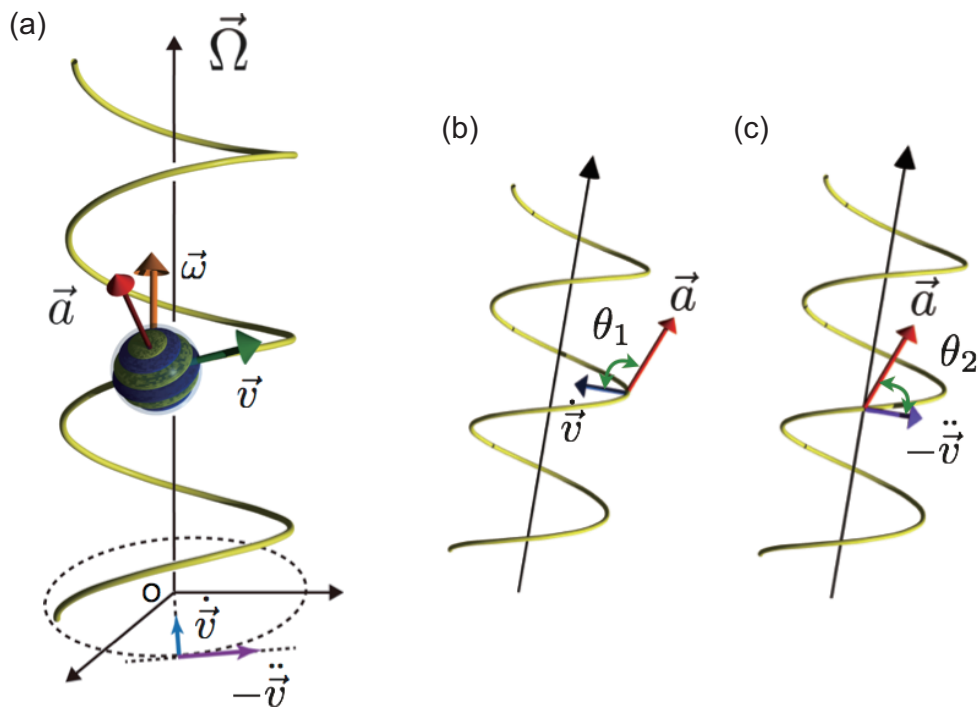
Figure 5.12: (a) Schematic of the spatial relations between a helical trajectory and the time derivatives of velocity. (b)(c) Definition of the angles θ_1 and θ_2 which indentify the spatial relation between the helical trajectory and the helical axis of the CLC droplet.

5.5.4   Term with coefficient c_2

We discuss the term with c_2. As the arrows in Fig. 4.17(a) indicate, we find a feature that the helical axis of the droplet is directed toward outside from the helical axis of the helical path. To quantify this feature, we use $\theta_1 = \arccos(\dot{\boldsymbol{v}} \cdot \boldsymbol{a}/|\dot{\boldsymbol{v}}|)$ (See Fig. 5.13(b)). When $\boldsymbol{a}$ is directed outside like the experimental result, $\theta_1 > \pi/2$. The effect of c_2 on θ_1 is numerically investigated in Fig. 5.13(a), which suggests that θ_1 is larger than $\pi/2$ when $c_2 > 0$. Accordingly, our model predicts that $c_2 > 0$ in the CLC droplet experiment. Meanwhile, the second-rank symmetric tensor $v_i v_j$ in the term with c_2 represents the symmetry of the flow field generated by the force dipole, with which the droplet is classified into a pusher or a puller in the squirmer model [116, 117]. We schematically depict such flow field in Fig. 5.14. For example, since *E. coli* pushes surrounding fluid forward and backward during swimming, it is classified as a pusher [118, 32]. In contrast, *Chlamydomonas reinhardtii* pulls surrounding fluid along the center line of the body, and hence it is called a puller [119, 32]. We consider that this term is derived from the torque on the helical director field due to a force dipole (Fig. 5.15). Let us consider situations where the direction of helical axis of a CLC droplet is deviated from the direction of translation. If $c_2 > 0$, the term with c_2 induces the torque for the helical axis to align parallel to the translational direction. Otherwise, a torque is exerted on the CLC droplet for the helical axis to align perpendicular to the translational direction. We schematically show these situations in Fig. 5.15. Although further investigation on the flow field is essential to understand c_2, our model suggests the importance of the force dipole in dynamics of the CLC droplet.
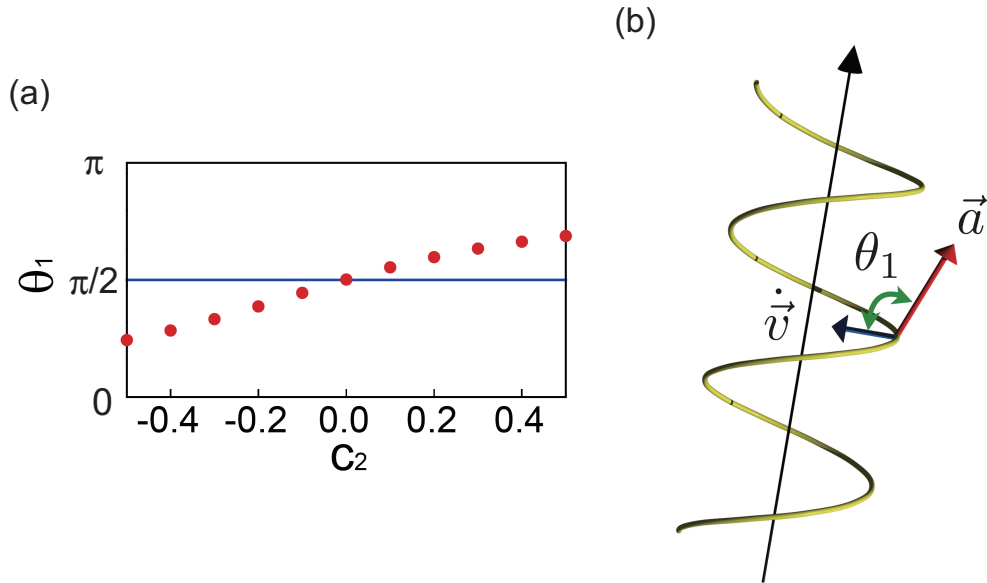
Figure 5.13: (a) Relation between θ_1 and c_2 in the uniaxial case ($\gamma = 6, \mu = 1.4$). The solid line represents $\theta_1 = \pi/2$. (b) Schematic image of the definition of θ_1, which is an angle between $\boldsymbol{a}$ and $\dot{\boldsymbol{v}}$. The helical path is drawn as a helix.
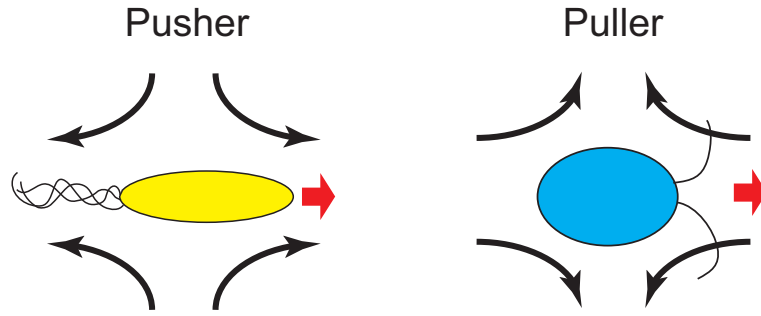
Figure 5.14: Exapmples of microswimmers which are classified as a pusher and a puller, respectively. While *E. coli* is classified as a pusher [118, 32], *Chlamydomonas reinhardtii* is classifeid as a puller [119, 32]. Such flow field which is originated from the force dipole is shown in each figure with curved arrows. Also, the red arrows indicate the direction of motion.
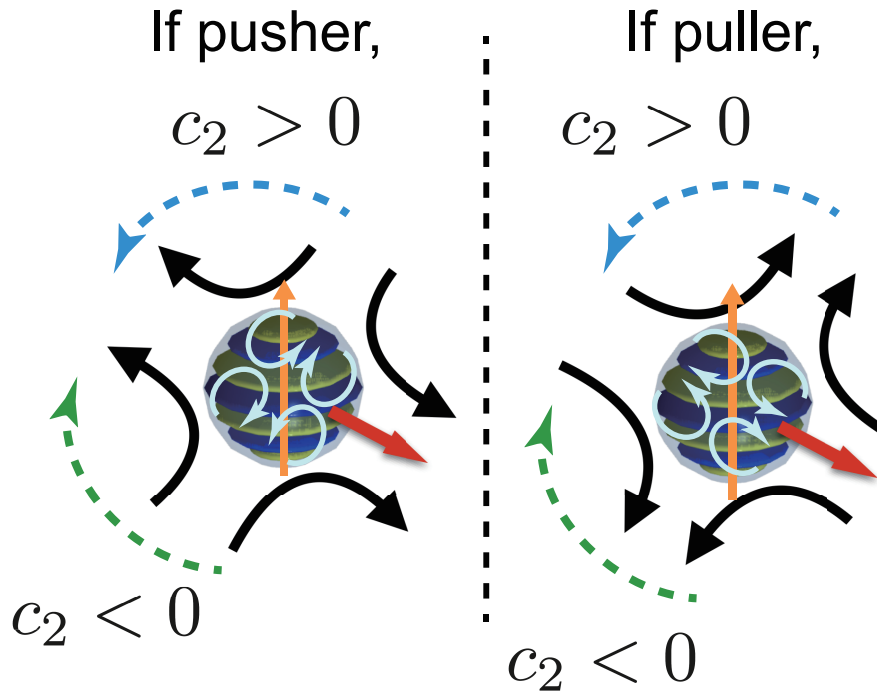
Figure 5.15: Schematic of our CLC droplets with flow fields characterized by the force dipoles. The flow fields are depicted both inside and outside the droplets with curved arrows. The dashed curves around the droplets are torques which the droplets feel from the flow fields. The blue dashed arrows represent the torques when $c_2 > 0$, while the green dashed arrows indicate those when $c_2 < 0$. Also, the helical axes of the droplets are drawn as orange arrows.

5.6   Discussion

We found that our model exhibits several chiral motions, that is SSS, SSP and H, depending on the parameters γ and μ for self-propulsion and chiral couplings (Fig. 5.9). Here, we qualitatively discuss the phase diagrams we obtained.

5.6.1   SSS and SSP phases

First, we provide an intuitive interpretation on the reason why the SSS and SSP phases appear in low and high μ regions in Fig. 5.9, respectively. In our model parameters, we assumed anisotropic viscosity represented by $a_1 < 0$ in the CLC droplets, where the viscosity is lower in the direction *perpendicular to the helical axis* of the droplet than that parallel to the helical axis as schematically depicted in Fig. 5.8. When the chiral coupling is weak, translational motion dominates the motion of the droplet, and the rotational motion is slaved by the translational motion. Accordingly, the droplet shows spinning straight motion along the direction perpendicular to the helical axis (SSS), when μ is small (Fig. 5.9).

In contrast, we also assumed that the rotational response to the Marangoni flow is stronger in the direction *parallel to the helical axis* than that perpendicular to the helical axis by taking into consideration the experimental results on the Lehmann effect we described in Chapter 3, where CLC droplets rotate faster under a temperature gradient when the temperature gradient is *parallel to the helical axis* of the droplet than when it is perpendicular to the helical axis. The relations $\mu = \nu, \mu^{\mathrm{iso}} = \nu^{\mathrm{iso}} = 0.7\mu(\alpha = 0.2)$ we set in our numerical simulations satisfy such assumption. Hence, we consider that the rotational motion dominates the motion of the droplet, when the chiral coupling is strong. Consequently, the droplet exhibits spinning straight motion in the direction parallel to the helical axis of the droplet (SSP), when μ is large (Fig. 5.9).

5.6.2   H phase and nonlinearity of our model

Meanwhile, helical motion (H) appears between SSS and SSP in our model (Fig. 5.9). We suspected the helical motion appears owing to the nonlinearity of our model. In our model, we have four nonlinear terms with respect to v and ω, that is, $v_j v_j v_i, a_2 \epsilon_{ijk} \omega_j v_k, \omega_j \omega_j \omega_i, c_2 \epsilon_{ijk} Q_{jl} v_l v_k$. Note that, the term with a_2 brings nonlinearity to our models when $a_2 \neq 1$, since if we look at our equations with the particle frame which is introduced in Appendix B, $(a_2 - 1)$ is a coefficient which brings a nonlinearity of the equations as shown in Eq. (5.62). To investigate whether such nonlinear terms are necessary for the helical motion, we performed numerical simulations by eliminating the terms $\omega_j \omega_j \omega_i, c_2 \epsilon_{ijk} Q_{jl} v_l v_k$ and setting $a_1 = 1$, while we keep the term $v_j v_j v_i$, which is essential for the self-propulsion of the droplet.

Fig. 5.16 shows the phase diagrams in such situations for both uniaxial ($P = 0$) and biaxial ($P = 0.1$) cases. We found that the model does not show helical motions but only NM, ST, SSS and SSP. The linear stability limits of NM, SSS, SSP are also shown as

curves in Fig. 5.16. Interestingly, the linear stability limits of SSS and SSP coincide at the boundary between SSS and SSP, and the boundary between SSS an SSP is parallel to the γ-axis ($\mu = \sqrt{-\zeta/(2\alpha + 3/2 - P/2)}$). Although it is difficult to completely identify which nonlinear terms are essential for the helical motion, we found that our model does not show helical motions in the absence of any nonlinear terms. It seems quite natural to introduce such nonlinear terms in our phenomenological model, since the original hydrodynamic equations are highly nonlinear.
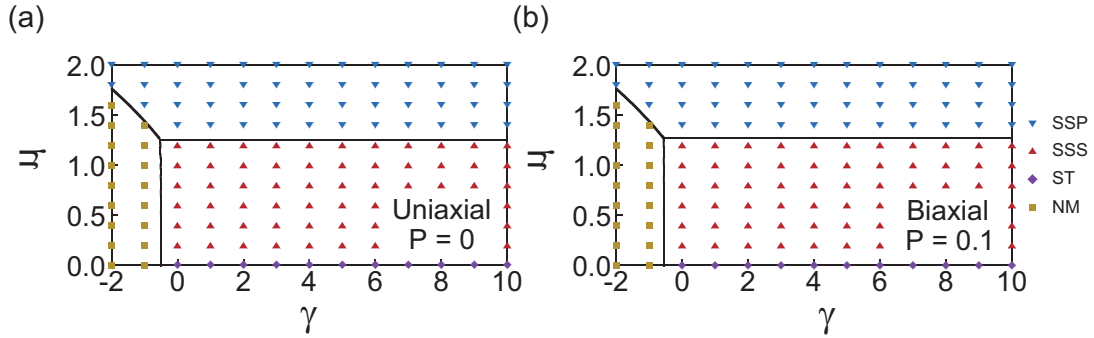
Figure 5.16: Phase diagrams of our model without nonlinear terms except the self-propulsion term, for (a) uniaxial ($P = 0$) and (b) biaxial case ($P = 0.1$). The other coefficients in linear-terms are same as those we applied in nonlinear case in Fig. 5.9. The phase boundaries between SSS and SSP are parallel to the horizontal-axes.

5.7   Conclusion and remarks

In this chapter, we proposed a phenomenological model of chirality-induced helical self-propulsion of a CLC droplet, based on the theoretical framework of the self-propelled objects proposed by Ohta et al. [52]. We found that our model exhibits helical motion due to the nonlinearity of our model equations and the chiral coupling terms between v and ω. Interestingly, in addition to the helical motion, we found that other chiral motions which we call SSS and SSP appear as solutions of the model equations. Transitions between each chiral motion are associated with the bifurcation of the dynamical system. Also, we found that the uniaxiality and biaxiality of the CLC droplet change the types of bifurcations between SSP and H; Hopf bifurcation for uniaxial case ($P = 0$) and zero-eigenvalue bifurcation in biaxial case ($P = 0.1$). These features have not been reported yet in previous models of helical motions. Furthermore, our model sheds light on the importance of the force dipoles on the detail dynamics of helical motions, which classify the microswimmer into a pusher or a puller.

   To justify our model as a model of a CLC droplet, several experimental and theoretical works remain. From the experimental points of view, it is necessary to experimentally test the phase diagrams and bifurcations. In principle, we can control the parameters μ and γ by changing the concentration of chiral dopants and surfactant

solutions. We also consider that the uniaxiality of the droplet will increase by increasing the chirality of the droplet, since the anisotropy perpendicular to the helical axis will decrease when the pitch of the CLC is short. The measurement of the flow field inside/outside the droplet is also required to justify our model, especially the importance of force dipoles.

From the theoretical view points, our model has to be derived from the hydrodynamic equations governing the dynamics of surfactant solutions and CLC. As we introduced in Sec. 5.2.4, such derivations have succeeded in the case of isotropic self-propelled droplet in surfactant solutions [102, 103]. However, it requires analytical solutions of the Stokes equations governing the isotropic fluid with the low-Reynolds number. Hence, the lack of analytical solutions of CLC will challenge such works on the derivation. Understanding of the molecular mechanisms of the self-propulsion of our droplet, which are not well understood for the moment, should be also necessary for such theoretical works.

Although quantitative arguments are difficult with our model, our model succeeded in prediction of non-trivial bifurcation structures and phase diagrams. We believe that our model will provide important insights on the self-propelled motion of chiral objects thanks to the generality of the formulation of our equations constructed by symmetry argument.

5.8   Appendix A: Frenet-Serret frame

Frenet-Serret formula is a concept which describes the geometric property of a continuous and differentiable curve in 3D Euclidean space or a particle moving on the curve [120]. The curve is described using a tangent vector t, normal vector $n = \dot{t}/|\dot{t}|$ and binormal vector $b = t \times n$ as follows:

$$\frac{dt}{ds} = \kappa n, \tag{5.27}$$

$$\frac{dn}{ds} = -\kappa t + \tau b, \tag{5.28}$$

$$\frac{db}{ds} = -\tau n, \tag{5.29}$$

where d/ds is the derivative with respect to arc length, κ, τ are the curvature and torsion of the curve, respectively. These vectors are illustrated in Fig. 5.5.

If we consider a particle moving with the velocity v on the curve, we have $ds = |v|dt$ where t is time. Substituting $ds = |v|dt$ into the Frenet-Serret formula, we obtain,

$$v = |\dot{r}|, \tag{5.30}$$

$$\dot{r} = vt, \tag{5.31}$$

$$\dot{t} = v\kappa n, \tag{5.32}$$

$$\dot{n} = -v\kappa t + v\tau b, \tag{5.33}$$

$$\dot{b} = -v\tau n, \tag{5.34}$$

where $r(t)$ is a Cartesian coordinate of particle at time t. Here, the dots operate the time derivative.

Note that we have following relations between Frenet-Serret frame and Cartesian coordinate;

$$t = \frac{\dot{r}}{|\dot{r}|}, \tag{5.35}$$

$$n = \frac{\dot{r} \times (\ddot{r} \times \dot{r})}{|\dot{r} \times (\ddot{r} \times \dot{r})|}, \tag{5.36}$$

$$b = \frac{\dot{r} \times \ddot{r}}{|\dot{r} \times \ddot{r}|}. \tag{5.37}$$

Also, curvature and torsion are given as,

$$\kappa = \frac{d\boldsymbol{t}}{ds} \cdot \boldsymbol{n} \tag{5.38}$$

$$= \frac{|\dot{\boldsymbol{r}} \times \ddot{\boldsymbol{r}}|}{|\dot{\boldsymbol{r}}|^3}, \tag{5.39}$$

$$\tau = -\frac{d\boldsymbol{b}}{ds} \cdot \boldsymbol{n} \tag{5.40}$$

$$= \frac{\dot{\boldsymbol{r}} \cdot (\ddot{\boldsymbol{r}} \times \dddot{\boldsymbol{r}})}{|\dot{\boldsymbol{r}} \times \ddot{\boldsymbol{r}}|^2}. \tag{5.41}$$

Consider a helical motion where the helical axis is along z axis, the diameter is r, the helical pitch is $P = 2\pi|h|$, and angular velocity is $\omega > 0$, and we have,

$$x(t) = r\cos(\omega t), \tag{5.42}$$

$$y(t) = r\sin(\omega t), \tag{5.43}$$

$$z(t) = h\omega t, \tag{5.44}$$

where the sign of h determines the handedness of the helical path. If $h > 0$, the helix is right-handed. Otherwise, left-handed.

Since arclength $s(t)$ is denoted as $s(t) = \sqrt{r^2 + h^2}\omega t$, we obtain a description with the Frenet-Serret frame,

$$\boldsymbol{t}(s) = \left(\frac{-r}{\sqrt{r^2 + h^2}} \sin(\omega t), \frac{r}{\sqrt{r^2 + h^2}} \cos(\omega t), \frac{h}{\sqrt{r^2 + h^2}} \right), \tag{5.45}$$

$$\boldsymbol{n}(s) = \left(-\cos(\omega t), -\sin(\omega t), 0 \right), \tag{5.46}$$

$$\boldsymbol{b}(s) = \left(\frac{h}{\sqrt{r^2 + h^2}} \sin(\omega t), \frac{-h}{\sqrt{r^2 + h^2}} \cos(\omega t), \frac{r}{\sqrt{r^2 + h^2}} \right). \tag{5.47}$$

Curvature κ and torsion τ are described as follows:

$$\kappa = \frac{r}{r^2 + h^2}, \tag{5.48}$$

$$\tau = \frac{h}{r^2 + h^2}. \tag{5.49}$$

Also, if the helical motion is perfect, $\Omega(t)$ defined as follows are invariant.

$$\Omega(t) = v(\tau \boldsymbol{t}(t) - \kappa \boldsymbol{b}(t)). \tag{5.50}$$

$\Omega(t)$ describes the angular velocity of the helical motion. Hence, a unit vector $\boldsymbol{h}$ indicating the direction of the helical axis is $\boldsymbol{h} = \Omega/|\Omega|$. Using $\Omega(t)$, we have following formulas,

$$\dot{\boldsymbol{t}} = \Omega \times \boldsymbol{t}, \tag{5.51}$$

$$\Omega \cdot \boldsymbol{t} = v\tau, \tag{5.52}$$

$$|\Omega \times \boldsymbol{t}| = v\kappa. \tag{5.53}$$

Finally, the helical radius r and pitch P is described as,

$$
\begin{aligned}
r &= \kappa/(\kappa^2 + \tau^2), & (5.54) \\
P &= 2\pi h = 2\pi\tau/(\kappa^2 + \tau^2). & (5.55)
\end{aligned}
$$

Here, $h = 0$ provides a circular motion with $\kappa = 1/r, \tau = 0$.

5.9 Appendix B: Coordinate transformation from the lab frame to the particle frame

To simplify the linear stability analysis, a coordinate transformation from the lab frame (v, ω, Q) to the particle frame $(\tilde{v}, \tilde{\omega}, \tilde{Q})$ was performed. Just for simplicity, we rewrite the Eqs. 5.23-5.25 in this chapter in more general form as follows:

$$
\begin{aligned}
\frac{dv_i}{dt} &= f_i(v, Q, \omega), & (5.56) \\
\frac{d\omega_i}{dt} &= g_i(v, Q, \omega), & (5.57) \\
\frac{dQ_{ij}}{dt} &= \epsilon_{kjl}Q_{ik}\omega_l - \epsilon_{ikl}\omega_l Q_{kj}. & (5.58)
\end{aligned}
$$

Since the particle frame is a rotating reference frame with the angular velocity ω, we have the following time-evolution equations in the particle frame:

$$
\begin{aligned}
\frac{d\tilde{v}_i}{dt} &= f_i(\tilde{v}, \tilde{Q}, \tilde{\omega}) - \epsilon_{ijk}\tilde{\omega}_j\tilde{v}_k, & (5.59) \\
\frac{d\tilde{\omega}_i}{dt} &= g_i(\tilde{v}, \tilde{Q}, \tilde{\omega}), & (5.60) \\
\frac{d\tilde{Q}_{ij}}{dt} &= 0. & (5.61)
\end{aligned}
$$

Note that, if we define a 3×3 orthogonal matrix P as the transformation matrix, where $\tilde{v} = Pv, \tilde{\omega} = P\omega, \tilde{Q} = PQP^T$, we have the relation $\dot{P}(t) = \Omega(t)P(t)$. Here, the 2nd rank anti-symmetric tensor Ω is defined as $\Omega_{ij} = \epsilon_{ijk}\omega_k$.

Consequently, we only need to perform the linear stability analysis of the following time-evolution equations with regard to $\tilde{v}$ and $\tilde{\omega}$ in the particle frame.

$$
\begin{aligned}
\frac{d\tilde{v}_i}{dt} &= \gamma\tilde{v}_i - \tilde{v}_j\tilde{v}_j\tilde{v}_i + a_1\tilde{Q}_{ij}\tilde{v}_j + (a_2 - 1)\epsilon_{ijk}\tilde{\omega}_j\tilde{v}_k \\
&\quad + \mu^{\text{iso}}\tilde{\omega}_i + \mu\tilde{Q}_{ij}\tilde{\omega}_j, & (5.62) \\
\frac{d\tilde{\omega}_i}{dt} &= \zeta\tilde{\omega}_i - \tilde{\omega}_j\tilde{\omega}_j\tilde{\omega}_i + c_1\tilde{Q}_{ij}\tilde{\omega}_j + c_2\epsilon_{ijk}\tilde{Q}_{jl}\tilde{v}_l\tilde{v}_k \\
&\quad + \nu^{\text{iso}}\tilde{v}_i + \nu\tilde{Q}_{ij}\tilde{v}_j. & (5.63)
\end{aligned}
$$

In the linear stability analysis, we set $\tilde{Q}_{ij}$ as follows:

$$\tilde{Q} = \begin{bmatrix} q_1 = 1 & 0 & 0 \\ 0 & q_2 = -\frac{1}{2}(1-P) & 0 \\ 0 & 0 & q_3 = -\frac{1}{2}(1+P) \end{bmatrix}. \quad (5.64)$$

Here, a, b and c in the main text are parallel to x-axis, y-axis and z-axis in the particle frame. q_1, q_2 and q_3 are the eigenvalues of Q_{ij}, corresponding to the eigenvectors a, b and c. Also, P is a biaxial parameter in the main text. In the uniaxial case, we set $P = 0$.

5.10 Appendix C: Linear stability analysis

We show the detail of the linear stability analysis of N (No motion), SSS (Spinning Straight motion along Secondary axis) and SSP (Spinning Straight motion along Primary axis) using the particle frame introduced above. In the following, we take $(\tilde{v}_1, \tilde{v}_2, \tilde{v}_3, \tilde{\omega}_1, \tilde{\omega}_2, \tilde{\omega}_3)$ as our dynamical variables.

5.10.1 Linear stability analysis of N

In N phase, $\tilde{v} = \tilde{\omega} = 0$, which is a trivial fixed point of Eqs. (5.62) and (5.63). We obtain the Jacobian J_N as follows:

$$J_N = \begin{bmatrix} \gamma + a_1 q_1 & 0 & 0 & \mu^{iso} + \mu q_1 & 0 & 0 \\ 0 & \gamma + a_1 q_2 & 0 & 0 & \mu^{iso} + \mu q_2 & 0 \\ 0 & 0 & \gamma + a_1 q_3 & 0 & 0 & \mu^{iso} + \mu q_3 \\ \nu^{iso} + \nu q_1 & 0 & 0 & \zeta + c_1 q_1 & 0 & 0 \\ 0 & \nu^{iso} + \nu q_2 & 0 & 0 & \zeta + c_1 q_2 & 0 \\ 0 & 0 & \nu^{iso} + \nu q_3 & 0 & 0 & \zeta + c_1 q_3 \end{bmatrix}. \quad (5.65)$$

With respect to the reciprocal relation among pseudo scalar parameters in the main text, we introduce a parameter α just for simplicity as follows:

$$\mu^{iso} = (\frac{1}{2} + \alpha)\mu, \quad (5.66)$$

$$\mu = \nu, \quad (5.67)$$

$$\mu^{iso} = \nu^{iso}. \quad (5.68)$$

Note that we set $\alpha = 0.2$ in the main text. Setting $a_1 = -1, c_1 = 0$ as in the main text, we analytically obtain the linear stability limit as follows:

$$\gamma = \begin{cases} 1 + \frac{1}{\zeta}(\frac{3}{2} + \alpha)^2 \mu^2, & \text{if } \gamma < \frac{-3/4 - P/2 - \alpha - \alpha^2}{3/2 - P/2 + 2\alpha}, \\ -(\frac{1}{2} + P/2) + \frac{1}{\zeta}(\alpha - P/2)^2 \mu^2, & \text{otherwise.} \end{cases}$$

Also, the coordinate of the intersection of the two branch is $(\gamma, \mu) = \left(\frac{-3/4 - P/2 - \alpha - \alpha^2}{3/2 - P/2 + 2\alpha}, \sqrt{\frac{-\zeta}{(2\alpha + 3/2 - P/2)}} \right)$.

5.10.2   Linear stability analysis of SSS

SSS is the spinning straight motion (SS) along secondary axis. In the biaxial case, we have two secondary axes b and c. However, when $a_1 < 0$ as considered in the main text, the spinning straight motion (SS) with $\tilde{v} \parallel \tilde{\omega} \parallel b$ is so unstable that SS with $\tilde{v} \parallel \tilde{\omega} \parallel c$ appears as SSS, since the axis which has the lower negative eigenvalue is the favorable direction of the motion in SSS. Consequently, $\tilde{v}$ is parallel to c and $\tilde{\omega}$ in SSS. Putting the solution $\tilde{v} = (0, 0, \tilde{v}_s)$ and $\tilde{\omega} = (0, 0, \tilde{\omega}_s)$, we obtain the following Jacobian J_{SSS} of the SSS solution,

$$
J_{\text{SSS}} = \begin{bmatrix}
\gamma + a_1 q_1 - \tilde{v}_s^2 & -(a_2 - 1)\tilde{\omega}_s & 0 & \mu^{\text{iso}} + \mu q_1 & (a_2 - 1)\tilde{v}_s & 0 \\
(a_2 - 1)\tilde{\omega}_s & \gamma + a_1 q_2 - \tilde{v}_s^2 & 0 & -(a_2 - 1)\tilde{v}_s & \mu^{\text{iso}} + \mu q_2 & 0 \\
0 & 0 & \gamma + a_1 q_3 - 3\tilde{v}_s^2 & 0 & 0 & \mu^{\text{iso}} + \mu q_3 \\
v^{\text{iso}} + v q_1 & c_2(q_2 - q_3)\tilde{v}_s & 0 & \zeta + c_1 q_1 - \tilde{\omega}_s^2 & 0 & 0 \\
c_2(q_3 - q_1)\tilde{v}_s & v^{\text{iso}} + v q_2 & 0 & 0 & \zeta + c_1 q_2 - \tilde{\omega}_s^2 & 0 \\
0 & 0 & v^{\text{iso}} + v q_3 & 0 & 0 & \zeta + c_1 q_3 - 3\tilde{\omega}_s^2
\end{bmatrix}. \quad (5.69)
$$

Here, $\tilde{v} = (0, 0, \tilde{v}_s), \tilde{\omega} = (0, 0, \tilde{\omega}_s)$ is a steady solution of Eqs. (5.62) and (5.63). Hence, $(\tilde{v}_s, \tilde{\omega}_s)$ is a non-trivial solution of the following equations.

$$
(\mu^{\text{iso}} + q_3 \mu)\tilde{\omega}_s = \tilde{v}_s^3 - (\gamma + a_1 q_3)\tilde{v}_s, \quad (5.70)
$$

$$
(v^{\text{iso}} + q_3 v)\tilde{v}_s = \tilde{\omega}_s^3 - (\zeta + c_1 q_3)\tilde{\omega}_s. \quad (5.71)
$$

In the range of the parameters in the main text, we have three solutions: 0 and two symmetric solutions with respect to the origin of the phase space. Since the degrees of the freedom in the z-axis span the stable manifold, we considered the following Jacobian J'_{SSS} by removing the degrees of the freedom in the z-axis from J_{SSS}.

$$
J'_{\text{SSS}} = \begin{bmatrix}
\gamma + a_1 q_1 - \tilde{v}_s^2 & -(a_2 - 1)\tilde{\omega}_s & \mu^{\text{iso}} + \mu q_1 & (a_2 - 1)\tilde{v}_s \\
(a_2 - 1)\tilde{\omega}_s & \gamma + a_1 q_2 - \tilde{v}_s^2 & -(a_2 - 1)\tilde{v}_s & \mu^{\text{iso}} + \mu q_2 \\
v^{\text{iso}} + v q_1 & c_2(q_2 - q_3)\tilde{v}_s & \zeta + c_1 q_1 - \tilde{\omega}_s^2 & 0 \\
c_2(q_3 - q_1)\tilde{v}_s & v^{\text{iso}} + v q_2 & 0 & \zeta + c_1 q_2 - \tilde{\omega}_s^2
\end{bmatrix}. \quad (5.72)
$$

Next, we define the characteristic polynomial $f_s(\lambda)$ of J'_{SSS}. In the biaxial case, substituting one of the non-trivial solutions of Eqs. (5.70) and (5.71) into $f_s(\lambda)$, we calculated the linear stability limit by numerically solving $f_s(0) = 0$ with respect to γ and μ. Here, the function ContourPlot on Mathematica was used. In the uniaxial case, J'_{SSS} always has a zero eigenvalue and we obtain,

$$
f_s(\lambda) = \lambda \begin{vmatrix}
-(\mu^{\text{iso}} + q_2 \mu)\frac{\tilde{\omega}_s}{\tilde{v}_s} + a_1(q_1 - q_2) - \lambda & -(a_2 - 1)\tilde{\omega}_s & \mu^{\text{iso}} + \mu q_1 \\
(a_2 - 1)\tilde{\omega}_s - c_2(q_2 - q_1)\frac{\tilde{v}_s^2}{\tilde{\omega}_s} & -(\mu^{\text{iso}} + q_2 \mu)(\frac{\tilde{\omega}_s}{\tilde{v}_s} + \frac{\tilde{v}_s}{\tilde{\omega}_s}) - \lambda & -(a_2 - 1)\tilde{v}_s \\
\mu^{\text{iso}} + \mu q_1 & 0 & -\frac{\tilde{v}_s}{\tilde{\omega}_s}(\mu^{\text{iso}} + q_2 \mu) + c_1(q_1 - q_2) - \lambda
\end{vmatrix}. \quad (5.73)
$$

Here, we used the uniaxiality $q_2 = q_3$, Eqs. (5.67) and (5.68) and the following relations obtained from Eqs. (5.70) and (5.71),

$$(\mu^{\text{iso}} + q_3\mu)\frac{\tilde{\omega}_s}{\tilde{v}_s} = \tilde{v}_s^2 - (\gamma + a_1q_3), \tag{5.74}$$

$$(\nu^{\text{iso}} + q_3\nu)\frac{\tilde{v}_s}{\tilde{\omega}_s} = \tilde{\omega}_s^2 - (\zeta + c_1q_3). \tag{5.75}$$

Equating the determinant in Eq. (5.73) to zero and setting $\lambda = 0$, we calculated the linear stability limit in the same way performed in the biaxial case. As a result, we found that zero-eigenvalue bifucations occur at the boundaries in both uniaxial $P = 0$ and biaxial case $P = 0.1$.

5.10.3   Linear stability analysis of SSP

In SSP, $\tilde{v}$ is parallel to a and $\tilde{\omega}$. Putting the solution $\tilde{v} = (\tilde{v}_p, 0, 0)$ and $\tilde{\omega} = (\tilde{\omega}_p, 0, 0)$, we obtain the following Jacobian J_{SSP} of the SSP solution,

$$J_{\text{SSP}} = \begin{bmatrix} \gamma + a_1q_1 - 3\tilde{v}_p^2 & 0 & 0 & \mu^{\text{iso}} + \mu q_1 & 0 & 0 \\ 0 & \gamma + a_1q_2 - \tilde{v}_p^2 & -(a_2-1)\tilde{\omega}_p & 0 & \mu^{\text{iso}} + \mu q_2 & (a_2-1)\tilde{v}_p \\ 0 & (a_2-1)\tilde{\omega}_p & \gamma + a_1q_3 - \tilde{v}_p^2 & 0 & -(a_2-1)\tilde{v}_p & \mu^{\text{iso}} + \mu q_3 \\ \nu^{\text{iso}} + \nu q_1 & 0 & 0 & \zeta + c_1q_1 - 3\tilde{\omega}_p^2 & 0 & 0 \\ 0 & \nu^{\text{iso}} + \nu q_2 & c_2(q_3-q_1)\tilde{v}_p & 0 & \zeta + c_1q_2 - \tilde{\omega}_p^2 & 0 \\ 0 & c_2(q_1-q_2)\tilde{v}_p & \nu^{\text{iso}} + \nu q_3 & 0 & 0 & \zeta + c_1q_3 - \tilde{\omega}_p^2 \end{bmatrix}.\tag{5.76}$$

Here, $\tilde{v} = (\tilde{v}_p, 0, 0)$, $\tilde{\omega} = (\tilde{\omega}_p, 0, 0)$ is a steady solution of Eqs. (5.62) and (5.63). Hence, $(\tilde{v}_p, \tilde{\omega}_p)$ is a non-trivial solution of the following equations.

$$(\mu^{\text{iso}} + q_1\mu)\tilde{\omega}_p = \tilde{v}_p^3 - (\gamma + a_1q_1)\tilde{v}_p, \tag{5.77}$$

$$(\nu^{\text{iso}} + q_1\nu)\tilde{v}_p = \tilde{\omega}_p^3 - (\zeta + c_1q_1)\tilde{\omega}_p. \tag{5.78}$$

In the range of the parameters in the main text, we have three solutions of Eqs. (5.77) and (5.78): 0 and two symmetric solutions with respect to the origin of the phase space. Since the degrees of the freedom in the x-axis span the stable manifold, we considered the following Jacobian J'_{SSP} by removing the degrees of the freedom in the x-axis from J_{SSS}.

$$J'_{\text{SSP}} = \begin{bmatrix} \gamma + a_1q_2 - \tilde{v}_p^2 & -(a_2-1)\tilde{\omega}_p & \mu^{\text{iso}} + \mu q_2 & (a_2-1)\tilde{v}_p \\ (a_2-1)\tilde{\omega}_p & \gamma + a_1q_3 - \tilde{v}_p^2 & -(a_2-1)\tilde{v}_p & \mu^{\text{iso}} + \mu q_3 \\ \nu^{\text{iso}} + \nu q_2 & c_2(q_3-q_1)\tilde{v}_p & \zeta + c_1q_2 - \tilde{\omega}_p^2 & 0 \\ c_2(q_1-q_2)\tilde{v}_p & \nu^{\text{iso}} + \nu q_3 & 0 & \zeta + c_1q_3 - \tilde{\omega}_p^2 \end{bmatrix}. \tag{5.79}$$

In our analysis, one of the non-trivial solutions of Eqs. (5.77) and (5.78) was substituted into J'_{SSP}. We calculated the largest eigenvalue of J'_{SSP} for each γ and μ, and plotted the linear stability limit as a contour on γ–μ space, where the real part of the largest eigenvalue λ_{max} equals to zero. Here, the function ListContourPlot on Mathematica was used. By checking the imaginary part of the largest eigenvalues, we determined whether zero-eigenvalue bifurcation or Hopf bifurcation occurs at the boundaries. Consequently, the Hopf bifurcation occurs in the uniaxial case, while the zero-eigenvalue bifurcation occurs in the biaxial case $P = 0.1$.

Chapter 6

Conclusion and perspective

In the dissertation, we experimentally studied non-equilibrium dynamics of cholesteric liquid crystal (CLC) and constructed the phenomenological models; rotational dynamics of CLC droplets under a temperature gradient (the Lehmann effect [19]) and helical self-propulsion of CLC droplets. First, we summarize the central results on each topic.

In Chapter 3, we investigated the rotational motion of CLC droplets under a temperature gradient (the Lehmann effect). We controlled the angle between the helical axis of CLC droplets and the direction of the temperature gradient by changing anchoring conditions of LC cells. Using a such method, we observed the rotation of the three types of CLC droplets under a temperature gradient (Fig. 3.6). One of the three types of CLC droplets, which we call the stripeless droplet, was realized for the first time. We also found that the rotational velocity of these droplets depends differently on their size (Fig. 3.9). By determining the 3D structures of the droplets using the fluorescence confocal polarizing microscopy (FCPM [63], Fig. 3.13), we constructed a phenomenological model to describe these rotational behaviors following the basic ideas of the hydrodynamic model of CLC (the Ericksen-Leslie theory). We concluded that introduction of a surface torque is necessary to explain the rotational velocity. Although it requires further works to reveal the origin of the surface torque, the consistency between our experimental results and the model shows that such surface torque probably exists.

Next, we reported our discovery on the Marangoni-effect-driven spontaneous helical motion of CLC droplets dispersed in surfactant solution in Chapter 4. When the sizes of the droplets are large, the droplets did not show helical motion since the director field of the droplets are strongly disturbed by the Marangoni flow. Then, we discovered that, as the droplets shrink due to the dissolution process of CLC into surfactant solution, the droplets suddenly start to exhibit helical motion with the homogenous helical director field (Fig. 4.14). Furthermore, we experimentally confirmed that the handedness of the helical motion is reversed by changing the handedness of the chiral dopant (Fig. 4.15). In contrast, the nematic LC (NLC) showed only ballistic motion (Fig. 4.16). Hence, we concluded that the helical motion is derived from the chirality of CLC. As the studies on the Lehmann effect taught us that CLC can rotate due to the chiral coupling between

external fields such as temperature gradient and rotational motion of the director field, we speculated that chiral couplings between the Marangoni flow and the rotational motion of the CLC droplet allows the droplets swim in helical paths (Fig. 4.18). We also proposed the mechanism of the size-dependent texture of the droplets considering the effect of viscosity, elasticity and increasing concentration of chiral dopants during the locomotion.

In Chapter 5, we proposed a novel phenomenological model of spontaneous helical motion of a CLC droplet by symmetry argument in chiral systems. We found that our model exhibits helical motion due to the nonlinearity of our model equations and the chiral coupling terms between v and ω. In addition to helical motions, we found that other chiral motions which we call SSS and SSP appear as solutions of the model equations, where the translational and rotational directions are parallel (Fig. 5.9). The bifurcation behaviors of our model were investigated by changing the parameters which control the strength of self-propulsion and the chiral couplings, which should be experimentally controllable by changing the concentration of surfactant and chiral dopants. Furthermore, our model showed importance of force dipoles on the detail dynamics of the helical motions (Fig. 5.13).

Throughout this dissertation, we experimentally explored roles of chirality in non-equilibrium dynamics of CLC focusing on the cross effects allowed only in chiral systems. Even though such cross effects in CLC were theoretically predicted in the Ericksen-Leslie theory (ELT) to explain the first non-equilibrium phenomenon of CLC, that is the Lehmann effect, we still do not have enough experimental validation of the theory. In our experiments on the Lehmann effect, we concluded that some surface torque on the CLC droplet induced by a temperature gradient is probably exist in addition to the temperature-gradient-induced torque introduced in the ELT. Although the origin of the surface torque has not been revealed yet, we consider that one of the possible mechanisms is the Marangoni effect induced by the temperature gradient on the surface of the CLC droplet, taking into consideration that the CLC droplets exhibit rotational motions owing to the Marangoni effect as we discovered in our experiments on the helical motion of CLC droplets.

The latter experiments on the spontaneous helical motion of the CLC droplets were motivated not only by interests in the hydrodynamics of CLC but also by that in roles of chirality in microswimmers. Chiral microswimmers which show chiral motions such as rotation [24, 25], circular motion [26, 27] and helical motions [28, 29] are ubiquitous in biological systems due to the biological molecular chirality. Nevertheless, the role of chirality in microswimmers in 3D had not been investigated using artificial microswimmers, which have advantages of the controllability of experimental parameters such as handedness of microswimmers and strength of self-propulsion. Although there is still a leap between the CLC droplets and chiral living microswimmers [28], our first realization of 3D chiral artificial microswimmer without any external field will open a new era of investigation on roles of chirality in microswimmers.

In our theoretical model of helical motion of CLC droplets, we revealed that the chiral couplings between spontaneous translation and rotation, and the non-lineality

of our model are essential for the emergence of helical motion. Helical motion is apparently a simple phenomenon which you may think trivial if the self-propelled object is chiral. However, our model showed that the helical motion appears non-trivially as a result of bifurcation behaviors of our model. Although our model itself can be applied when the structure is represented by the second rank tensor Q_{ij}, the formulation can be straightforwardly extended to the self-propelled objects which have structures represented by higher-order tensors [110, 111]. We believe that our experiments and theoretical models on chiral microswimmers play essential roles not only in fundamental physics but also as a design principle of artificial microswimmers, which are now increasing attentions in the micro-engineering [31, 121].

Meanwhile, we still have open questions we have to answer in future works. From the experimental point of view, the fluid flow in the CLC droplets on both experiments is unclear for the moment due to the lack of well established method to measure the velocity field in LC. The critical difficulty in the flow visualization of LC is that topological defects inevitably appear [122, 123] and may change the velocity field, when we add tracer particles for the flow visualization as we do in the case of the Newtonian fluid such as water. Recently, Yoshioka et al. proposed a non-invasive method of flow visualization of LC using photobleaching method [62] (Fig. 2.8). However, it is still required to enhance the spatial resolution of the method to reveal the flow field inside the CLC droplets in micro scale. We are now considering that visualization of flow field may be possible using quantum dots as tracers, whose sizes are the same oder of the size of LC molecules and may not disturb the director field. Such flow visualization is essential not only in our works but also for the development of liquid crystal science, since fluidity is one of essential feature characterizing LC.

From the theoretical point of view, our phenomenological models both on the Lehmann effect and helical motion were constructed rigorously taking our and previous experimental results into consideration. However, our model has not been justified from the hydrodynamic equations yet. For instance, in the case of isotropic self-propelled droplet in surfactant solutions, derivations of phenomenological models describing the motion of the droplet have succeeded [103, 102] (See also Sec. 5.2.4). However, it requires analytical solutions of the Stokes equations governing the isotropic fluid with low-Reynolds number. Hence, the lack of analytical solutions of CLC will challenge the derivation of our models from the hydrodynamic model of CLC. Also, numerical simulation of the hydrodynamic model of CLC is another essential way to investigate the phenomena. In fact, when we, experimentalists, compare the experimental results with the hydrodynamic theory such as the ELT, it is essential to quantitatively compare the experimental results with the dynamics of director field and velocity field calculated numerically. However, for instance, since numerical calculations of the Lehmann effect using hydrodynamic theories are still lacking, no one has compared the experimental results and hydrodynamic theories. Although we confront numerical difficulties due to the nonlinearity of the hydrodynamic theory of CLC when we work on the numerical simulations of hydrodynamics of CLC including the velocity field, several numerical schemes have been established in numerical calculation of LC dynamics

[124, 125, 126]. We hope that our works will stimulate such theoretical works and understanding of CLC dynamics will go beyond the current stage.

Lastly, this dissertation explored the fundamental aspects of non-equilibrium dynamics of chiral liquid crystal focusing on the chiral couplings between rotational motion of CLC, and either an external field (temperature gradient) or a field (the Marangoni flow) which spontaneously appears in the system. In fact, we still have open questions we have to solve. Nevertheless, we believe that our works including non-trivial experimental findings will advance the current understanding on the hydrodynamics of chiral fluids and also the role of chirality in microswimmers.

Bibliography

[1] F. Jafarpour, T. Biancalani, and N. Goldenfeld. Noise-Induced Mechanism for Biological Homochirality of Early Life Self-Replicators. *Physical Review Letters*, Vol. 115, p. 15801, 2015.

[2] Y. Saito and H. Hyuga. *Colloquium* : Homochirality: Symmetry breaking in systems driven far from equilibrium. *Reviews of Modern Physics*, Vol. 85, pp. 603–621, 2013.

[3] K. Soai, S. Osanai, K. Kadowsaki, S. Yonekubo, T. Shibata, and I. Sato. d- and l-quartz-promoted highly enantioselective synthesis of a chiral organic compound. *Journal of American Chemical Society*, Vol. 121, p. 11235, 1999.

[4] M. Mochizuki, X. Z. Yu, S. Seki, N. Kanazawa, W. Koshibae, J. Zang, M. Mostovoy, Y. Tokura, and N. Nagaosa. Thermally driven ratchet motion of a skyrmion microcrystal and topological magnon Hall effect. *Nature Materials*, Vol. 13, pp. 241–246, 2014.

[5] L. Kong and J. Zang. Dynamics of an Insulating Skyrmion under a Temperature Gradient. *Physical Review Letters*, Vol. 111, p. 067203, 2013.

[6] R. Yasuda, H. Noji, K. J. Kinoshita, and M. Yoshida. F_1-ATPase is a highly efficient molecular motor that rotates with discrete $120°$ steps. *Cell*, Vol. 93, p. 1117, 1998.

[7] T. C. Lubensky. Hydrodynamics of cholesteric liquid crystals. *Physical Review A*, Vol. 6, p. 452, 1972.

[8] S. Fürthauer, M. Strempel, S. W. Grill, and F. Jülicher. Active chiral fluids. *The European Physical Journal E*, Vol. 35, p. 89, 2012.

[9] S. Fürthauer, M. Strempel, S. W. Grill, and F. Jülicher. Active Chiral Processes in Thin Films. *Physical Review Letters*, Vol. 110, p. 048103, 2013.

[10] P. G. de Gennes and J. Prost. *The Physics of liquid crystals, 2nd edition*. Clarendon Press, Oxford, 1984.

[11] S. R. de Groot and P. Mazur. *Non-equilibrium thermodynamics*. Dover publications, inc., New York, 1984.

[12] L. D. Landau and E. M. Lifshitz. *Fluid Mechanics, 2nd ed.* Elsevier, Amsterdam, 1987.

[13] R. Piazza and A. Parola. Thermophoresis in colloidal suspensions. *Journal of Physics: Condensed Matter*, Vol. 20, p. 153102, 2008.

[14] S. Chandrasekhar. *Liquid Crystals, 2nd ed.* Cambridge Univ. Press, 1992.

[15] A. G. Cherstvy. DNA Cholesteric Phases: The Role of DNA Molecular Chirality and DNA-DNA Electrostatic Interactions. *The Journal of Physical Chemistry B*, Vol. 112, pp. 12585–12595, 2008.

[16] Z. Dogic and S. Fraden. Cholesteric Phase in Virus Suspensions. *Langmuir*, Vol. 16, pp. 7820–7824, 2000.

[17] M. Humar and I. Mušević. 3D microlasers from self-assembled cholesteric liquid-crystal microdroplets. *Optics express*, Vol. 18, pp. 26995–27003, 2010.

[18] G. Tkachenko and E. Brasselet. Optofluidic sorting of material chirality by chiral light. *Nature Communications*, Vol. 5, p. 3577, 2014.

[19] O. Lehmann. Struktur, system and magnetisches verhalten flüssiger kristalle und deren mischbarkeit mit feten. *Annalen der Physik*, Vol. 2, p. 649, 1900.

[20] F. M. Leslie. Some thermal effects in cholesteric liquid crystals. *Proceedings of the Royal Society A*, Vol. 307, p. 359, 1968.

[21] P. Oswald and A. Dequidt. Measurement of the Continuous Lehmann Rotation of Cholesteric Droplets Subjected to a Temperature Gradient. *Physical Review Letters*, Vol. 100, p. 217802, 2008.

[22] Y. Tabe and H. Yokoyama. Coherent collective precession of molecular rotors with chiral propellers. *Nature Materials*, Vol. 2, pp. 806–809, 2003.

[23] F. M. Leslie. Electromechanical effect in cholesteric liquid crystals with fixed boundary conditions. *Proceedings of the Royal Society A*, Vol. 89, p. 249, 1982.

[24] K. Drescher, K. C. Leptos, I. Tuval, T. Ishikawa, T. J. Pedley, and R. E. Goldstein. Dancing *Volvox* : Hydrodynamic Bound States of Swimming Algae. *Physical Review Letters*, Vol. 102, p. 168101, 2009.

[25] A. P. Petroff, X.-L. Wu, and A. Libchaber. Fast-Moving Bacteria Self-Organize into Active Two-Dimensional Crystals of Rotating Cells. *Physical Review Letters*, Vol. 114, p. 158102, 2015.

[26] E. Lauga, W. R. DiLuzio, G. M. Whitesides, and H. A. Stone. Swimming in Circles: Motion of Bacteria near Solid Boundaries. *Biophysical Journal*, Vol. 90, pp. 400–412, 2006.

[27] J. Elgeti, U. B. Kaupp, and G. Gompper. Hydrodynamics of Sperm Cells near Surfaces. *Biophysical Journal*, Vol. 99, pp. 1018–1026, 2010.

[28] J. F. Jikeli, L. Alvarez, B. M. Friedrich, L. G. Wilson, R. Pascal, R. Colin, M. Pichlo, A. Rennhack, C. Brenker, and U. B. Kaupp. Sperm navigation along helical paths in 3D chemoattractant landscapes. *Nature Communications*, Vol. 6, p. 7985, 2015.

[29] J. Gray. The movement of sea-urchin sperma tozoa. *Journal of Experimental Biology*, Vol. 32, p. 775, 1955.

[30]   2016 12 10 ( ) 12:24 UTC
       . `http://ja.wikipedia.org`.

[31] R. Dreyfus, J. Baudry, M. L. Roper, M. Fermigier, H. A. Stone, and J. Bibette. Microscopic artificial swimmers. *Nature*, Vol. 437, pp. 862–865, 2005.

[32] E. Lauga and T. R. Powers. The hydrodynamics of swimming microorganisms. *Reports on Progress in Physics*, Vol. 72, p. 096601, 2009.

[33] J. Elgeti, R. G. Winkler, and G. Gompper. Physics of microswimmers—single particle motion and collective behavior: A review. *Reports on Progress in Physics*, Vol. 78, p. 056601, 2015.

[34] S. Ramaswamy. The Mechanics and Statistics of Active Matter. *Annual Review of Condensed Matter Physics*, Vol. 1, pp. 323–345, 2010.

[35] M. C. Marchetti, J. F. Joanny, S. Ramaswamy, T. B. Liverpool, J. Prost, M. Rao, and R. A. Simha. Hydrodynamics of soft active matter. *Reviews of Modern Physics*, Vol. 85, pp. 1143–1189, 2013.

[36] W. F. Paxton, K. C. Kistler, C. C. Olmeda, A. Sen, S. K. St. Angelo, Y. Cao, T. E. Mallouk, P. E. Lammert, and V. H. Crespi. Catalytic Nanomotors: Autonomous Movement of Striped Nanorods. *Journal of the American Chemical Society*, Vol. 126, pp. 13424–13431, 2004.

[37] J. R. Howse, R. A. L. Jones, A. J. Ryan, T. Gough, R. Vafabakhsh, and R. Golestanian. Self-Motile Colloidal Particles: From Directed Propulsion to Random Walk. *Physical Review Letters*, Vol. 99, p. 048102, 2007.

[38] N. Mano and A. Heller. Bioelectrochemical Propulsion. *Journal of the American Chemical Society*, Vol. 127, pp. 11574–11575, 2005.

[39] T. Banno, A. Asami, N. Ueno, H. Kitahata, Y. Koyano, K. Asakura, and T. Toyota. Deformable Self-Propelled Micro-Object Comprising Underwater Oil Droplets. *Scientific Reports*, Vol. 6, p. 31292, 2016.

[40] W. F. Paxton, P. T. Baker, T. R. Kline, Y. Wang, T. E. Mallouk, and A. Sen. Catalytically Induced Electrokinetics for Motors and Micropumps. *Journal of the American Chemical Society*, Vol. 128, pp. 14881–14888, 2006.

[41] J. Gibbs and Y. Zhao. Catalytic nanomotors: Fabrication, mechanism, and applications. *Frontiers of Materials Science*, Vol. 5, pp. 25–39, 2011.

[42] J. L. Moran, P. M. Wheat, and J. D. Posner. Locomotion of electrocatalytic nanomotors due to reaction induced charge autoelectrophoresis. *Physical Review E*, Vol. 81, p. 065302, 2010.

[43] L. Zhang, J. J. Abbott, L. Dong, B. E. Kratochvil, D. Bell, and B. J. Nelson. Artificial bacterial flagella: Fabrication and magnetic control. *Applied Physics Letters*, Vol. 94, p. 064107, 2009.

[44] A. Ghosh and P. Fischer. Controlled Propulsion of Artificial Magnetic Nanostructured Propellers. *Nano Letters*, Vol. 9, pp. 2243–2245, 2009.

[45] Y. Ding, F. Qiu, X. Casadevall i Solvas, F. Chiu, B. Nelson, and A. deMello. Microfluidic-Based Droplet and Cell Manipulations Using Artificial Bacterial Flagella. *Micromachines*, Vol. 7, p. 25, 2016.

[46] F. Kümmel, B. ten Hagen, R. Wittkowski, I. Buttinoni, R. Eichhorn, G. Volpe, H. Löwen, and C. Bechinger. Circular Motion of Asymmetric Self-Propelling Particles. *Physical Review Letters*, Vol. 110, p. 198302, 2013.

[47] H. Löwen. Chirality in microswimmer motion: From circle swimmers to active turbulence. *The European Physical Journal Special Topics*, Vol. 225, pp. 2319–2331, 2016.

[48] S. Herminghaus, C. C. Maass, C. Krüger, S. Thutupalli, L. Goehring, and C. Bahr. Interfacial mechanisms in active emulsions. *Soft Matter*, Vol. 10, pp. 7008–7022, 2014.

[49] C. C. Maass, C. Krüger, S. Herminghaus, and C. Bahr. Swimming Droplets. *Annual Review of Condensed Matter Physics*, Vol. 7, pp. 171–193, 2016.

[50] P. Romanczuk and L. Schimansky-Geier. Brownian Motion with Active Fluctuations. *Physical Review Letters*, Vol. 106, p. 230601, 2011.

[51] R. Großmann, L. Schimansky-Geier, and P. Romanczuk. Active Brownian particles with velocity-alignment and active fluctuations. *New Journal of Physics*, Vol. 14, p. 073033, 2012.

[52] T. Ohta and T. Ohkuma. Deformable Self-Propelled Particles. *Physical Review Letters*, Vol. 102, p. 154101, 2009.

[53] H. R. Brand and H. Pleiner. New theoretical results for the Lehmann effect in cholesteric liquid crystals. *Physical Review A*, Vol. 37, p. 2736, 1988.

[54] G. S. Ranganath. Thermomechanical effects in cholesteric liquid crystals. *Molecular Crystals and Liquid Crystals Letters*, Vol. 92, p. 105, 1983.

[55] H. K. Jayaram, U. D. Kini, G. S. Ranganath, and S. Chandrasekhar. Thermomechanical Effect in Cholesteric Liquid-crystals. *Molecular Crystals and Liquid Crystals*, Vol. 99, pp. 155–160, 1983.

[56] A. N. Beris and B. J. Edwards. *Thermodynamics of Flowing Systems*. Oxford University Press, Oxford, 1994.

[57] T. Qian and P. Sheng. Generalized hydrodynamic equations for nematic liquid crystals. *Physical Review E*, Vol. 58, p. 7475, 1998.

[58] M. Ravnik and S. Žumer. Landau–de Gennes modelling of nematic liquid crystal colloids. *Liquid Crystals*, Vol. 36, pp. 1201–1214, 2009.

[59] P. Oswald, A. Dequidt, and A. Żywociński. Sliding planar anchoring and viscous surface torque in a cholesteric liquid crystal. *Physical Review E*, Vol. 77, p. 061703, 2008.

[60] P. Oswald. Microscopic vs. macroscopic origin of the Lehmann effect in cholesteric liquid crystals. *The European Physical Journal E*, Vol. 35, p. 10, 2012.

[61] P. Oswald and S. Pirkl. Lehmann rotation of the cholesteric helix in droplets oriented by an electric field. *Physical Review E*, Vol. 89, p. 022509, 2014.

[62] J. Yoshioka, F. Ito, Y. Suzuki, H. Takahashi, H. Takizawa, and Y. Tabe. Director/barycentric rotation in cholesteric droplets under temperature gradient. *Soft Matter*, Vol. 10, p. 5869, 2014.

[63] I. I. Smalyukh, S. Shiyanovskii, and O. Lavrentovich. Three-dimensional imaging of orientational order by fluorescence confocal polarizing microscopy. *Chemical Physics Letters*, Vol. 336, p. 88, 2001.

[64] I. Buttinoni, J. Bialké, F. Kümmel, H. Löwen, C. Bechinger, and T. Speck. Dynamical Clustering and Phase Separation in Suspensions of Self-Propelled Colloidal Particles. *Physical Review Letters*, Vol. 110, p. 238301, 2013.

[65] H. R. Brand and H. Pleiner. New theoretical results for the Lehmann effect in cholesteric liquid crystals. *Physical Review A*, Vol. 37, p. 2736, 1988.

[66] S. Sarman. Molecular theory of thermomechanical coupling in cholesteric liquid crystals. *The Journal of Chemical Physics*, Vol. 110, p. 12218, 1999.

[67] D. Svenšek, H. Pleiner, and H. R. Brand. Inverse Lehmann effects can be used as a microscopic pump. *Physical Review E*, Vol. 78, p. 021703, 2008.

[68] T. Lee, R. P. Trivedi, and I. I. Smalyukh. Multimodal nonlinear optical polarizing microscopy of long-range molecular order in liquid crystals. *Optics letters*, Vol. 35, pp. 3447–3449, 2010.

[69] M. Marinelli, F. Mercuri, U. Zammit, and F. Scudieri. Thermal conductivity and thermal diffusivity of the cyanobiphenyl (nCB) homologous series. *Physical Review E*, Vol. 58, p. 5860, 1998.

[70] T. Yamamoto, M. Kuroda, and M. Sano. Three-dimensional analysis of thermo-mechanically rotating cholesteric liquid crystal droplets under a temperature gradient. *EPL (Europhysics Letters)*, Vol. 109, p. 46001, 2015.

[71] S. Yang, Y. Liu, H. Tan, C. Wu, Z. Wu, G. Shen, and R. Yu. Gold nanoparticle based signal enhancement liquid crystal biosensors for DNA hybridization assays. *Chemical Communications*, Vol. 48, p. 2861, 2012.

[72] H. Lamb. *Hydrodynamics*. Dover, New York, 1945.

[73] T. Young. An essay on the cohesion of fluids. *Philosophical Transactions of the Royal Society of London*, Vol. 95, p. 65, 1805.

[74] R. S. Zola, L. R. Evangelista, Y.-C. Yang, and D.-K. Yang. Surface Induced Phase Separation and Pattern Formation at the Isotropic Interface in Chiral Nematic Liquid Crystals. *Physical Review Letters*, Vol. 110, p. 057801, 2013.

[75] N. R. Bernardino, M. C. F. Pereira, N. M. Silvestre, and M. M. Telo da Gama. Structure of the cholesteric–isotropic interface. *Soft Matter*, Vol. 10, pp. 9399–9402, 2014.

[76] R. S. Akopyan and B. Y. Zel'dovich. Thermomechanical effects in deformed nematics. *Zhurnal Experimental'noi i Teoreticheskoi Fiziki*, Vol. 60, p. 953, 1984.

[77] O. D. Lavrentovich and Y. A. Nastishin. Thermomechanical effect in deformed nematic liquid crystal. *Ukrains'kii Fizichnii Zhurnal*, Vol. 32, p. 710, 1987.

[78] A. Dequidt, G. Poy, and P. Oswald. Generalized drift velocity of a cholesteric texture in a temperature gradient. *Soft Matter*, Vol. 12, pp. 7529–7538, 2016.

[79] G. Poy and P. Oswald. Do Lehmann cholesteric droplets subjected to a temperature gradient rotate as rigid bodies? *Soft Matter*, Vol. 12, pp. 2604–2611, 2016.

[80] B. M. Friedrich and F. Jülicher. Steering Chiral Swimmers along Noisy Helical Paths. *Physical Review Letters*, Vol. 103, p. 068102, 2009.

[81] H. C. Crenshaw. Orientation by helical motion—I. Kinematics of the helical motion of organisms with up to six degrees of freedom. *Bulletin of Mathematical Biology*, Vol. 55, pp. 197–212, 1993.

[82] H. C. Crenshaw and L. Edelstein-Keshet. Orientation by helical motion—II. Changing the direction of the axis of motion. *Bulletin of mathematical biology*, Vol. 55, pp. 213–230, 1993.

[83] H. C. Crenshaw. Orientation by helical motion—III. Microorganisms can orient to stimuli by changing the direction of their rotational velocity. *Bulletin of Mathematical Biology*, Vol. 55, pp. 231–255, 1993.

[84] B. Liu, M. Gulino, M. Morse, J. X. Tang, T. R. Powers, and K. S. Breuer. Helical motion of the cell body enhances Caulobacter crescentus motility. *Proceedings of the National Academy of Sciences*, Vol. 111, pp. 11252–11256, 2014.

[85] Z. Izri, M. N. van der Linden, S. Michelin, and O. Dauchot. Self-Propulsion of Pure Water Droplets by Spontaneous Marangoni-Stress-Driven Motion. *Physical Review Letters*, Vol. 113, p. 248302, 2014.

[86] S. Michelin, E. Lauga, and D. Bartolo. Spontaneous autophoretic motion of isotropic particles. *Physics of Fluids (1994-present)*, Vol. 25, p. 061701, 2013.

[87] V. Pimienta, M. Brost, N. Kovalchuk, S. Bresch, and O. Steinbock. Complex Shapes and Dynamics of Dissolving Drops of Dichloromethane. *Angewandte Chemie International Edition*, Vol. 50, pp. 10728–10731, 2011.

[88] K. Nagai, Y. Sumino, H. Kitahata, and K. Yoshikawa. Mode selection in the spontaneous motion of an alcohol droplet. *Physical Review E*, Vol. 71, p. 065301(R), 2005.

[89] M. Schmitt and H. Stark. Marangoni flow at droplet interfaces: Three-dimensional solution and applications. *Physics of Fluids (1994-present)*, Vol. 28, p. 012106, 2016.

[90] C. Krüger, G. Klös, C. Bahr, and C. C. Maass. Curling Liquid Crystal Microswimmers: A Cascade of Spontaneous Symmetry Breaking. *Physical Review Letters*, Vol. 117, p. 048003, 2016.

[91] L. E. Scriven and C. V. Sternling. The marangoni effects. *Nature*, Vol. 187, p. 186, 1960.

[92] P. G. de Gennes, F. Brocahrd-Wyart, and D. Quéré. *Capillarity and Wetting Phenomena*. Springer, 2004.

[93] J. Thomson. On certain curious motions observable at the surfaces of wine and other alcoholic liquors. *Philosophical Magazine*, Vol. 10, p. 330, 1855.

[94] J. B. Fournier and A. M. Cazabat. Tears of wine. *EPL (Europhysics Letters)*, Vol. 20, p. 517, 1992.

[95] R. Vuilleumier, V. Ego, L. Neltner, and A. M. Cazabat. Tears of wine: The stationary state. *Langmuir*, Vol. 11, pp. 4117–4121, 1995.

[96] M. Gugliotti and T. Silverstein. Tears of wine. *Journal of Chemical Education*, Vol. 81, p. 67, 2004.

[97] D. C. Venerus and D. Nieto Simavilla. Tears of wine: New insights on an old phenomenon. *Scientific Reports*, Vol. 5, p. 16162, 2015.

[98] R. K. Shah, H. C. Shum, A. C. Rowat, D. Lee, J. J. Agresti, A. S. Utada, L.-Y. Chu, J.-W. Kim, A. Fernandez-Nieves, C. J. Martinez, and D. A. Weitz. Designer emulsions using microfluidics. *Materials Today*, Vol. 11, pp. 18–27, 2008.

[99] A. G. Chmielewski. Viscosity coefficients of some nematic liquid crystals. *Molecular Crystals and Liquid Crystals*, Vol. 132, p. 339, 1986.

[100] J. Happel and H. Brenner. *Low Reynolds Number Hydrodynamics*. Englewood Cliffs, NJ: Prentice Hall, 1965.

[101] H. Ebata and M. Sano. Swimming droplets driven by a surface wave. *Scientific Reports*, Vol. 5, p. 8546, 2015.

[102] S. Yabunaka, T. Ohta, and N. Yoshinaga. Self-propelled motion of a fluid droplet under chemical reaction. *The Journal of chemical physics*, Vol. 136, p. 074904, 2012.

[103] N. Yoshinaga, K. H. Nagai, Y. Sumino, and H. Kitahata. Drift instability in the motion of a fluid droplet with a chemically reactive surface driven by Marangoni flow. *Physical Review E*, Vol. 86, p. 016108, 2012.

[104] K. Krischer and A. Mikhailov. Bifurcation to traveling spots in reaction-diffusion systems. *Physical review letters*, Vol. 73, p. 3165, 1994.

[105] K. Keren, Z. Pincus, G. M. Allen, E. L. Barnhart, G. Marriott, A. Mogilner, and J. A. Theriot. Mechanism of shape determination in motile cells. *Nature*, Vol. 453, pp. 475–480, 2008.

[106] T. Hiraiwa, K. Shitara, and T. Ohta. Dynamics of a deformable self-propelled particle in three dimensions. *Soft Matter*, Vol. 7, pp. 3083–3086, 2011.

[107] S. H. Strogatz. *Nonlinear Dynamics and Chaos: With Application to Physics, Chemistry, and Engineering*. Westview Press, 2001.

[108] M. Tarama and T. Ohta. Dynamics of a deformable self-propelled particle with internal rotational force. *Progress of Theoretical and Experimental Physics*, Vol. 2013, p. 013A01, 2013.

[109] M. Tarama and T. Ohta. Spinning motion of a deformable self-propelled particle in two dimensions. *Journal of Physics: Condensed Matter*, Vol. 24, p. 464129, 2012.

[110] T. Hiraiwa, M. Y. Matsuo, T. Ohkuma, T. Ohta, and M. Sano. Dynamics of a deformable self-propelled domain. *EPL (Europhysics Letters)*, Vol. 91, p. 20001, 2010.

[111] T. Ohta, M. Tarama, and M. Sano. Simple model of cell crawling. *Physica D: Nonlinear Phenomena*, Vol. 318-319, pp. 3–11, 2016.

[112] E. Gurarie, D. Grünbaum, and M. T. Nishizaki. Estimating 3D Movements from 2D Observations Using a Continuous Model of Helical Swimming. *Bulletin of Mathematical Biology*, Vol. 73, pp. 1358–1377, 2011.

[113] R. N. Bearon. Helical swimming can provide robust upwards transport for gravitactic single-cell algae; a mechanistic model. *Journal of mathematical biology*, Vol. 66, pp. 1341–1359, 2013.

[114] F.-L. Wen, K.-t. Leung, and H.-Y. Chen. Spontaneous symmetry breaking for geometrical trajectories of actin-based motility in three dimensions. *Physical Review E*, Vol. 94, p. 012401, 2016.

[115] W. L. Zeile, F. Zhang, R. B. Dickinson, and D. L. Purich. *Listeria* 's right-handed helical rocket-tail trajectories: Mechanistic implications for force generation in actin-based motility. *Cell Motility and the Cytoskeleton*, Vol. 60, pp. 121–128, 2005.

[116] J. R. Blake. A spherical envelope approach to ciliary propulsion. *Journal of Fluid Mechanics*, Vol. 46, pp. 199–208, 1971.

[117] O. S. Pak and E. Lauga. Generalized squirming motion of a sphere. *Journal of Engineering Mathematics*, Vol. 88, pp. 1–28, 2014.

[118] K. Drescher, J. Dunkel, L. H. Cisneros, S. Ganguly, and R. E. Goldstein. Fluid dynamics and noise in bacterial cell–cell and cell–surface scattering. *Proceedings of the National Academy of Sciences*, Vol. 108, pp. 10940–10945, 2011.

[119] K. Drescher, R. E. Goldstein, N. Michel, M. Polin, and I. Tuval. Direct Measurement of the Flow Field around Swimming Microorganisms. *Physical Review Letters*, Vol. 105, p. 168101, 2010.

[120] B. Audoly and Y. Pomeau. *Elasticity and geometry, From Hair Curls to the Non-linear Response of Shells*. Oxford University Press Inc., New York, 2010.

[121] H. Wang and M. Pumera. Fabrication of Micro/Nanoscale Motors. *Chemical Reviews*, Vol. 115, pp. 8704–8735, 2015.

[122] I. Muševič. Nematic colloids, topology and photonics. *Philosophical Transactions of the Royal Society A: Mathematical, Physical and Engineering Sciences*, Vol. 371, p. 20120266, 2013.

[123] A. Martinez, M. Ravnik, B. Lucero, R. Visvanathan, S. Žumer, and I. I. Smalyukh. Mutually tangled colloidal knots and induced defect loops in nematic fields. *Nature Materials*, Vol. 13, pp. 258–263, 2014.

[124] J.-I. Fukuda. Effect of hydrodynamic flow on kinetics of nematic-isotropic transition in liquid crystals. *The European Physical Journal B-Condensed Matter and Complex Systems*, Vol. 1, pp. 173–177, 1998.

[125] C. M. Care, I. Halliday, and K. Good. Lattice Boltzmann nemato-dynamics. *Journal of Physics: Condensed Matter*, Vol. 12, p. L665, 2000.

[126] C. Denniston, E. Orlandini, and J. M. Yeomans. Lattice Boltzmann simulations of liquid crystal hydrodynamics. *Physical Review E*, Vol. 63, p. 056702, 2001.